

**THEORY AND EXPERIMENT OF PLANAR INVERTED F-
ANTENNAS FOR WIRELESS COMMUNICATIONS
APPLICATIONS**

by

Vadim Antonchik

B.Sc., St.-Petersburg State University of Aerospace Instrumentation, 2000

THESIS SUBMITTED IN PARTIAL FULFILLMENT OF
THE REQUIREMENTS FOR THE DEGREE OF

MASTER OF APPLIED SCIENCE

In the
School
of
Engineering Science

© Vadim Antonchik 2007

SIMON FRASER UNIVERSITY

Summer 2007

All rights reserved. This work may not be
reproduced in whole or in part, by photocopy
or other means, without permission of the author.

APPROVAL

Name: **Vadim Antonchik**
Degree: **Master of Applied Science**
Title of Thesis: **Theory and experiment of planar inverted F-antennas for wireless communications applications**

Examining Committee:

Chair: **Dr. Paul K. M. Ho**
Professor of School of Engineering Science

Dr. Rodney G. Vaughan
Senior Supervisor
Professor of School of Engineering Science

Dr. Ash M. Parameswaran
Supervisor
Professor of School of Engineering Science

Dr. Alireza (Nima) Mahanfar
Internal Examiner
Post-Doctorate Fellow of School of Engineering Science

Date Defended/Approved:

Aug 03 2007



SIMON FRASER UNIVERSITY
LIBRARY

Declaration of Partial Copyright Licence

The author, whose copyright is declared on the title page of this work, has granted to Simon Fraser University the right to lend this thesis, project or extended essay to users of the Simon Fraser University Library, and to make partial or single copies only for such users or in response to a request from the library of any other university, or other educational institution, on its own behalf or for one of its users.

The author has further granted permission to Simon Fraser University to keep or make a digital copy for use in its circulating collection (currently available to the public at the "Institutional Repository" link of the SFU Library website <www.lib.sfu.ca> at: <<http://ir.lib.sfu.ca/handle/1892/112>>) and, without changing the content, to translate the thesis/project or extended essays, if technically possible, to any medium or format for the purpose of preservation of the digital work.

The author has further agreed that permission for multiple copying of this work for scholarly purposes may be granted by either the author or the Dean of Graduate Studies.

It is understood that copying or publication of this work for financial gain shall not be allowed without the author's written permission.

Permission for public performance, or limited permission for private scholarly use, of any multimedia materials forming part of this work, may have been granted by the author. This information may be found on the separately catalogued multimedia material and in the signed Partial Copyright Licence.

While licensing SFU to permit the above uses, the author retains copyright in the thesis, project or extended essays, including the right to change the work for subsequent purposes, including editing and publishing the work in whole or in part, and licensing other parties, as the author may desire.

The original Partial Copyright Licence attesting to these terms, and signed by this author, may be found in the original bound copy of this work, retained in the Simon Fraser University Archive.

Simon Fraser University Library
Burnaby, BC, Canada

ABSTRACT

The planar inverted F-antenna (PIFA) is a compact element for wireless applications. There is little theory available on this subject. This dissertation investigates simple theoretical models for two most popular types of PIFA – rectangular and semicircular PIFA's.

The PIFA's three-slot cavity model (CM) and transmission line model (TLM) are presented here, along with numerical and physical experimental techniques and results for the PIFA far field and impedance behavior.

The CM is used to predict PIFA's far field pattern, polarization, impedance, Q-factor, and bandwidth from an equivalent resonant cavity with perfect magnetic and electric boundaries.

The TLM represents PIFA as an equivalent transmission lines arrangement with three branches representing its radiating slots and one short-circuited branch.

Extensive measurements and numerical simulations confirmed that PIFA's radiation and impedance characteristics can be predicted with simple theoretical calculations described here. The measurements also showed PIFA's pattern and impedance dependence on the sideslot radiation.

To my Mother

ACKNOWLEDGEMENTS

It is difficult to overstate my gratitude to my senior supervisor, Prof. Rodney Vaughan for providing me with a chance to be a part of his research team. I deeply appreciate the enthusiasm, inspiration, support, and patience he has shown throughout my program.

I would like to thank my supervisor Prof. Ash M. Parameswaran for his valuable feedback and suggestions which helped to improve the contents and presentation of this work. I also want to thank my internal examiner and a colleague Dr. Nima Mahanfar for his constructive feedback on this thesis and his valuable help and advice on numerical electromagnetic solvers and methods.

I would also like to thank Mr. Peter McConnell, Dr. Behrouz Pourseyed, and Mr. Sushil Basnet from Sierra Wireless Inc, Richmond BC for the time and effort they have generously put in arranging a number of antenna measurements sessions performed for this work at the company's Satimo anechoic chamber.

I would also like to thank my colleagues from the Wireless Communications Lab whom I had a pleasure to work with, especially Mr. Bradley Zarikoff, Dr. Inas Khalifa, and Mrs. Sara Bavarian.

Last but not the least, I want to express my deep gratitude to my family for their constant encouragement, patience, and support.

TABLE OF CONTENTS

Approval	ii
Abstract.....	iii
Acknowledgements	v
Table of Contents	vi
List of Figures.....	ix
1 Introduction	1
1.1 Planar Inverted F-Antennas.....	2
1.2 Motivation and approach.....	4
1.3 Contributions.....	6
1.4 Organization of the thesis.....	7
2 Cavity Model For a Rectangular PIFA.....	9
2.1 Introduction	9
2.2 PIFA field distribution (TM-modes).....	10
2.3 Equivalent magnetic currents.....	15
2.4 PIFA radiating far fields derivation	19
2.4.1 End slot contribution to the far field of PIFA	19
2.4.2 Side slot contribution to the far field of PIFA	21
2.4.3 Combined side slot contribution to the far field of PIFA using array factor concept.....	23
2.4.4 Total PIFA radiated fields using array theory.....	25
2.5 Enhanced model for PIFA magnetic currents and far fields	31
3 Cavity Model For a Semicircular PIFA	37
3.1 Introduction	37
3.2 Semicircular PIFA field distribution (TM-modes)	37
3.3 Equivalent magnetic currents.....	40
3.4 PIFA radiating far fields derivation	43
4 PIFA Q-factor, bandwidth, input impedance and polarization.....	48
4.1 Introduction	48
4.2 PIFA Q-factor.....	48
4.2.1 PIFA losses, antenna efficiency	49
4.2.2 PIFA radiation Q-factor	51
4.2.3 PIFA dielectric Q-factor	51
4.2.4 PIFA conductor Q-factor	52
4.3 PIFA Q-factor limit and bandwidth	53
4.4 PIFA input impedance.....	58
4.5 PIFA polarization	62

5	Transmission Line Model.....	71
5.1	Introduction	71
5.2	Basic transmission line model.....	72
5.3	Three slot transmission line model	75
5.4	Expressions for transmission line parameters	77
5.4.1	Endslot conductance	78
5.4.2	Endslot susceptance	83
5.4.3	Sideslot conductance.....	86
5.4.4	Sideslot susceptance.....	89
5.4.5	Transmission line propagation constants and characteristic impedances.....	90
5.5	Results and comparisons	92
6	Measurements and simulations.....	97
6.1	Introduction	97
6.2	PIFA impedance measurements considerations.....	97
6.2.1	The reflection coefficient, VSWR	97
6.2.2	Scattering parameters.....	98
6.2.3	Bandwidth	100
6.3	PIFA prototype design considerations	101
6.3.1	Prototype I.....	101
6.3.2	Prototype II	102
6.3.3	Prototype III	103
6.4	PIFA test-set layout.....	104
6.5	PIFA far field measurements considerations	106
6.6	PIFA numerical simulation with commercial software packages.....	107
6.7	Results and comparisons	107
6.7.1	Rectangular PIFA impedance and resonant frequency	107
6.7.2	Semicircular PIFA impedance and resonant frequency.....	111
6.7.3	Rectangular PIFA far fields	113
6.7.4	Semicircular PIFA far fields	115
7	Conclusions.....	117
7.1	Summary and contributions	117
7.2	Conclusions	118
7.3	Future work	119
8	Bibliography	121
9	Appendices	125
9.1	Maxwell equations	126
9.2	Wave (Helmholtz) equation	127
9.3	Boundary conditions	129
9.3.1	Arbitrary.....	129
9.3.2	Electric wall	129
9.3.3	Magnetic wall.....	130
9.4	Coordinate transformations.....	131
9.4.1	Rectangular to spherical coordinate transformation [1].....	131

9.4.2	Cylindrical to spherical coordinate transformation [1].....	131
9.5	Far fields components for a magnetic current source	132
9.6	PIFA impedance measurements	133
9.6.1	Rectangular PIFA.....	133
9.6.2	Semicircular PIFA	134

LIST OF FIGURES

Figure 1.1	Isometric view of an example of the rectangular PIFA on finite groundplane.....	3
Figure 1.2	Isometric view of an example of the semicircular PIFA on finite groundplane.....	4
Figure 2.1	Cavity model for PIFA element shown with a finite ground plane.....	10
Figure 2.2	Electric field configurations (modes) for the rectangular PIFA.....	14
Figure 2.3	Dominant mode electric fields of the rectangular PIFA. Fringing fields of the dominant mode.....	15
Figure 2.4	Rectangular PIFA radiating fields and their equivalent magnetic current densities.....	17
Figure 2.5	Equivalent magnetic current source of a rectangular PIFA.	18
Figure 2.6	Linear array arrangement of side slot equivalent magnetic currents for rectangular PIFA.....	23
Figure 2.7	Two isotropic point sources with identical amplitudes spaced one-half wavelength apart: near field (left) and far field (right) observation.	24
Figure 2.8	XZ plane (H plane) far field patterns for an example of the rectangular PIFA ($W = \lambda / 2$, $L = \lambda / 4$).....	27
Figure 2.9	YZ plane (E plane) far field patterns for an example of the rectangular PIFA ($W = \lambda / 2$, $L = \lambda / 4$).....	28
Figure 2.10	XZ plane (H plane) far field pattern for an example of the rectangular PIFA ($W = \lambda / 2$, $L = \lambda / 4$).....	29
Figure 2.11	YZ plane (E plane) far field pattern for an example of the rectangular PIFA ($W = \lambda / 2$, $L = \lambda / 4$).....	29
Figure 2.12	XY plane (Ground plane) far field pattern for an example of the rectangular PIFA ($W = \lambda / 2$, $L = \lambda / 4$).....	30
Figure 2.13	Principal planes total far field patterns for an example of the rectangular PIFA ($W = \lambda / 2$, $L = \lambda / 4$).....	31
Figure 2.14	Rectangular PIFA far field patterns in the XY plane for different values of the end slot illumination pedestal ‘height’.....	33
Figure 2.15	Rectangular PIFA far field patterns in the XY plane for different values of the end slot illumination negative pedestal ‘height’.....	36

Figure 3.1	Cavity model for semicircular PIFA element with an infinite ground plane.....	38
Figure 3.2	Electric field configurations (modes) for the semicircular PIFA.....	39
Figure 3.3	Dominant mode electric field of the semicircular PIFA. Fringing fields of the dominant mode.....	40
Figure 3.4	Semicircular PIFA radiating field and its respective equivalent magnetic current density.....	41
Figure 3.5	Equivalent magnetic current source of semicircular PIFA.....	42
Figure 3.6	XZ plane (H plane) far field pattern for an example of the semicircular PIFA ($ka = 1.84$).....	45
Figure 3.7	YZ plane (E plane) far field pattern for an example of the semicircular PIFA ($ka = 1.84$).....	46
Figure 3.8	XY plane (Ground plane) far field pattern for an example of the semicircular PIFA ($ka = 1.84$).....	47
Figure 4.1	Minimum unloaded Q of electrically small antennas according to a dipole mode and the two modes in equal excitation as a function of the enclosing radius.....	55
Figure 4.2	The PIFA's VSWR=2 bandwidth versus the substrate permittivity according to different models results. Cavity height $h=7.5\text{mm}$	57
Figure 4.3	Rectangular PIFA input impedance fed at an arbitrary point along its center length: Cavity model, experimental results, CST FDTD solver, and WIPL-D Method of Moments solver.....	60
Figure 4.4	Rectangular PIFA input impedance fed at an arbitrary point along its sideslot length: Cavity model, experimental results, CST FDTD solver, and WIPL-D Method of Moments solver.....	61
Figure 4.5	XZ (top), YZ plane (bottom) CP patterns for an example of the rectangular PIFA ($W = \lambda / 2$, $L = \lambda / 4$). Experiment and numerical results are of the PIFA with: substrate thickness – 1mm, metal plate thickness $t = 1.7$ mm. $W = 146$ mm, $L = 78$ mm. The groundplane size: 400x300 mm (WxL).	65
Figure 4.6	Rectangular PIFA on infinite groundplane CP axial ratio for a full spatial sphere of radiation in 3D. CST FDTD results.....	66
Figure 4.7	Rectangular PIFA on finite groundplane CP axial ratio for a full spatial sphere of radiation in 3D. CST FDTD results.....	67
Figure 4.8	Rectangular PIFA (top) and semicircular PIFA (bottom) on infinite groundplanes axial ratios for a full spatial sphere of radiation in 2D. CST FDTD results.....	68
Figure 4.9	Rectangular PIFA (top) and semicircular PIFA (bottom) on finite groundplanes axial ratios for a full spatial sphere of radiation in 2D. CST FDTD results.....	69

Figure 5.1	PIFA's equivalent three-slot arrangement. In practice, the slot width is constant, i.e., the indented corners are not implemented, they are drawn indented to clarify the slots dimensioning.....	72
Figure 5.2	Perspective view of PIFA fed at an arbitrary point along y axis and its one-slot transmission line model.	73
Figure 5.3	Perspective view of PIFA fed at an arbitrary point along x and y axes and its three-slot transmission line model equivalent network.	76
Figure 5.4	PIFA endslot conductance versus the normalized width according to: a) equivalent voltage source approach; b) aperture field integration method for different truncation factors; c) Cavity Model far field integration technique. *a) and c) are almost indistinguishable.....	82
Figure 5.5	PIFA endslot susceptance versus the normalized width according to open-end capacitance formula, Wiener-Hopf approach, and curve fitting formula for two substrate permittivity values (substrate height $h=1$ mm).	85
Figure 5.6	PIFA sideslot conductance and susceptance versus the normalized slot width (height is varied) according to Booker's relation approach ($L=\lambda/4$, $\epsilon_r = 1$).....	89
Figure 5.7	PIFA sideslot susceptance versus the normalized slot width according to Booker's relation approach (substrate height $h=1$ mm, $\epsilon_r = 1$).	90
Figure 5.8	PIFA TE_{10} complement waveguide.....	92
Figure 5.9	PIFA input impedance as a function of feed position along the centre length of the antenna. Experimental data is from [1] for three different PIFA heights.....	94
Figure 5.10	The PIFA input impedance as a function of feed position along the edge-slot of the antenna. The parameters of the PIFA: substrate thickness – 1mm, metal plate thickness $t = 1.8$ mm. $W = 146$ mm, $L = 78$ mm. The ground plane size: 400x300 mm (WxL).....	95
Figure 6.1	The 2 port network.	98
Figure 6.2	Rectangular PIFA prototype III. Via holes and SMA connectors are seen. Pen provided for scale. Patch: $W = 148$ mm, $L = 74$ mm, substrate height (air): 1mm ($\lambda/308$), plate thickness (brass): 1.7 mm ($\lambda/181$), groundplane: $W = 400$ mm , $L = 300$ mm	103
Figure 6.3	Semicircular PIFA prototype III. Via holes and nylon washers are seen. Ruler provided for scale. Patch radius: $a = 90$ mm, substrate height (air): 1mm ($\lambda/328$), plate thickness (brass): 1.7 mm ($\lambda/199$).	104
Figure 6.4	PIFA test setup.	105
Figure 6.5	Satimo Anechoic chamber setup.	106

Figure 6.6	Measured and simulated resonant frequency of the probe-fed rectangular PIFA along center (top) and one of its sideslots (bottom) versus the feed position.....	109
Figure 6.7	Measured and simulated resonant frequency of the probe-fed rectangular PIFA along its endslot versus the feed position.....	110
Figure 6.8	Measured and simulated resonant frequency of the probe-fed semicircular PIFA along its center, 45 degrees off the center (top) and PIFA along its circumferential endslot (bottom) versus the feed position.....	112
Figure 6.9	The rectangular PIFA far field in the: H-plane ($\phi = 0$) – top and E-plane ($\phi = 90$) – bottom. Parameters of the PIFA: W= 148mm, L=74mm, Ground plane size: WxL = 400x300 mm. Resonant frequency $f_r = 975$ MHz.....	113
Figure 6.10	The rectangular PIFA far field in the XY-plane ($\theta = 90$). Parameters of the PIFA: W= 148mm, L=74mm, Ground plane size: WxL = 400x300 mm. Resonant frequency $f_r = 975$ MHz.....	114
Figure 6.11	The semicircular PIFA far field in H-plane ($\phi = 0$) – top and E-plane ($\phi = 90$) – bottom. Parameters of the PIFA: a= 90mm, resonant frequency $f_r = 915$ MHz.....	115
Figure 6.12	The semicircular PIFA far field in the XY-plane ($\theta = 90$). Parameters of the PIFA: a= 90mm, resonant frequency $f_r = 915$ MHz.....	116
Figure 9.1	Measured and simulated input impedance of the probe-fed rectangular PIFA along sideslot (1-4), endslot (4-6) and center (6-9) versus frequency.....	134
Figure 9.2	Measured input impedance of the probe-fed semicircular PIFA along circumference (1-4), center (4-7) and 45° radius (7,8,2) versus frequency.....	135

1 INTRODUCTION

In the past decades, cellular communications have become a ubiquitous part of modern life. The desire of people to be able to communicate effectively while being mobile has become an incentive for mobile communications integration in terrestrial and satellite wireless systems. The mobile communications industry has already developed enormously bringing fast and reliable infrastructure to people's disposal. Yet, wireless communications systems are still in the centre of extensive academic and technological research and development, with constant demand of more compact, faster and more reliable devices and services.

Regardless of the type of wireless applications in question, an antenna represents the most naturally evident part of any wireless communication system. A significant amount of effort has already been invested into research and development of modern mobile communications antennas. However, rapid expansion of mobile applications, such as 2.5G and 3G cellular systems, Bluetooth, WLAN, WiMax and other broadband applications, has lead to a further need for improvement of modern antenna systems and their major characteristics.

Antennas make different forms of wireless communication possible. Research in the area of antennas, in general, is fuelled by the need for more efficient, compact and sophisticated antenna systems. Such systems are required to satisfy an ever increasing demand for higher bandwidths wireless applications from rapidly growing customer base and data rates.

In recent years, with the general trend of wireless communication devices becoming more compact, the space allocated for an antenna in such devices has become the most valuable commodity, driving the research in the area to investigating antennas with lowest possible spatial profiles. Thus microstrip antennas have dominated in wireless communications devices design, having good spatial properties, while providing adequate characteristics considering antenna bandwidth, gain and efficiency. They are also attractive for having low fabrication cost and well suited for mass production and printed circuit board integration.

Since the introduction of the concept of microstrip radiators by [2] and later by [3], extensive research has been put in this area, leading to diversified applications and establishing the whole new topic of microstrip antennas within the broad field of microwave antennas.

Various types of microstrip antennas have been developed – microstrip patches of different form and configuration, printed loops, dipoles and monopoles of various shapes, cavity baked slots, planar inverted F-antennas etc. The characteristics and possible applications of these antenna types vary significantly, however, in this work, the main focus will be given to investigation of planar inverted F-antennas.

1.1 Planar Inverted F-Antennas

The *planar inverted F-antenna* or PIFA (may also be referred to as a hybrid microstrip antenna [4] – rectangular PIFA (Figure 1.1), or a half-disk antenna – semicircular PIFA (Figure 1.2)) is one of the most compact microstrip patch antennas. It can provide the same resonant frequency at less than half size of conventional patch

antenna. It is in its essence a half of the usual patch antenna with one of its radiating edges shorted to ground-plane along zero potential line. Therefore, the PIFA has the advantage of being more compact than the conventional patch, while providing very good bandwidth capabilities with comparable antenna gain and efficiency. It is also capable of multi-band frequency operation, which makes it an ideal candidate for wireless communications devices and systems.

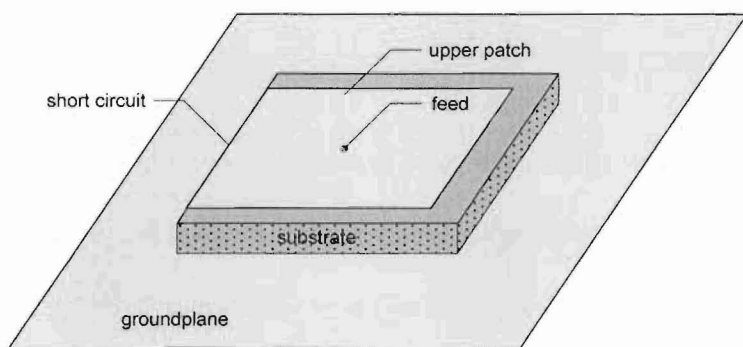


Figure 1.1 Isometric view of an example of the rectangular PIFA on finite groundplane.

Applications where the PIFA radiators have already excelled or expected to dominate in the near future are: satellite/terrestrial communications [5], various cellular communications equipment such as handset terminals/base stations [6], GPS devices [7-9], biomedical transceivers and implantable applications [9-11], WLAN transceivers [12, 13] and Bluetooth devices [14-16], and MIMO systems [17, 18].

This list is by no means exhaustive. The number of applications of the PIFA and PIFA-derived antennas continues to grow rapidly.

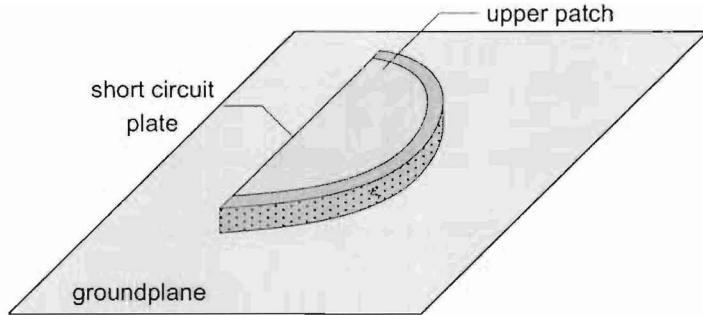


Figure 1.2 Isometric view of an example of the semicircular PIFA on finite groundplane.

1.2 Motivation and approach

The PIFA has become one of the most popular antennas in recent years, bringing much attention to the research in this area. Most contemporary treatments of the PIFA and PIFA-derived antennas include numerical solutions using expensive electromagnetic software packages and conventional experimental iterations design techniques (see for example the Proceedings of APS-2007). Both these methods are time consuming and expensive. Usually, when developing an antenna for a specific application and frequency, physical and numerical iterations of the dimensions and feed position are inevitable as they allow for corrections to the model which account for field fringing, finite ground plane effects, variable substrate permittivity, etc. For basic design, though, one needs a tool to estimate accurately the basic characteristics of the antenna performance, in particular, the behavior of the pattern, impedance, bandwidth and polarization.

For instance, the far field pattern is often not important for compact antennas, where the interest is often to simply achieve a compact, matched device. However, for array antennas, the pattern is often important, such as for satellite communications terminals, which have pattern constraints. In such applications, understanding the element

pattern details becomes important for the array design, and in particular for compact array designs, which use compact elements.

Theoretical models for the impedance and radiation characteristics are available for conventional microstrip antennas [4, 19-21]. They provide simple and insightful information regarding major characteristics of the antennas. However, for the PIFA, there are still improvements to be made. There is little theory available on the PIFA in the literature. One of the main objectives of this work is to review and improve the state of the art of PIFA theory using simple analytical models.

The most popular approaches in microstrip antennas' analysis are proved to be the *cavity model* (CM), *transmission line model* (TLM) and the *full wave analysis* (integral equations and/or *Method of Moments*, *Finite Difference Time Domain* methods).

While the transmission line model is the easiest of all of the above mentioned approaches, and it gives fair physical insight into microstrip radiation mechanisms, it lacks accuracy and flexibility in dealing with coupling effects of patches. The classic two-slot transmission line model, which was initially proposed for a rectangular patch antenna [22], is not accurate when applied to the PIFA. It was later improved by [1] for the rectangular PIFA by replacing the classic two-slot arrangement with the variable uniformly radiating slot and short circuit arrangement, paired with the two fixed radiating sideslots of the PIFA, which helped to provide accurate information about the PIFA impedance only across its center.

In comparison to the transmission line model, the cavity model is more accurate, yet at the same time, more computationally complex. Calculations based on the cavity method are the most useful for analysis of microstrip antennas. The cavity model offers

both the simplicity of computations and a great physical insight in radiation mechanisms of microstrip structures. Again, the classic two-slot cavity model was initially proposed for a rectangular [23] and circular [24] patch antennas, however, later it was successfully applied to various patches with different geometries. Nevertheless, as the author is aware, the cavity model results for the PIFA far fields, impedance etc have not been reported in the literature yet. An attempt has been made in [1] to describe electric vector potentials for the PIFA three equivalent magnetic currents.

In general, the full wave models are accurate and flexible, if properly applied. They can provide adequate results for variety of different microstrip radiators, arrays of elements of different shape, and coupling effects. However, they give less physical insight if compared to the cavity model as well as they are the most analytically and numerically complex of all described models [25-27]. These methods are utilized widely in commercially available electromagnetic (EM) software and will also be briefly discussed in this work.

1.3 Contributions

Design of any antenna device with specific characteristics requires multiple “cut-and-trial” iterations. This research builds upon and improves the state of the art in designing microstrip PIFA of different configurations, and aims at providing efficient paths of first cut design to minimize the number of experimental iterations. The contributions of this research to the design and analysis of the PIFA are briefly introduced here and elaborated in the following chapters. They include:

- Simple and novel three-slot cavity model for accurate prediction of rectangular PIFAs' far field patterns, polarization, Q-factor, frequency bandwidth, and input impedance;
- Simple and novel cavity model for accurate prediction of semicircular PIFAs' far field patterns and polarization;
- Simple and novel three-slot transmission line model for accurate prediction of the rectangular PIFA's input impedance across its upper patch area;
- Detailed description of the measurement techniques, and various antenna prototypes used during the physical measurements stage;
- Performance evaluation of the abovementioned theoretical methods and characteristics using extensive physical and numerical experiment results.

1.4 Organization of the thesis

This dissertation consists of 7 Chapters, and is organized as follows. Chapters 2 to 6 present the contributions of this work to current state of the art in PIFA research using simple theoretical models and extensive physical and numerical experiments. Chapter 2 introduces and develops the new three-slot cavity model for the rectangular PIFA using fundamental cavity physics to derive the PIFA's far fields' expressions. Enhanced models using cosine on the pedestal type distributions for the PIFA endslot magnetic current are also proposed and developed in the Chapter 2. In Chapter 3 the cavity model is applied to the semicircular PIFA antenna case and its far field expressions are computed numerically using semicircular electric vector potential functions of the cavity. The

PIFA's major characteristics such as antenna Q-factor, input impedance, frequency bandwidth, and polarization are derived in Chapter 4 using the abovementioned cavity models' results. Chapter 5 is focused on the investigation of the rectangular PIFA impedance using the transmission line model, and the PIFA transmission line parameters evaluation using different approaches. Extensive physical measurements and numerical simulations results are presented in Chapter 6 to validate the theoretical predictions about the PIFA's characteristics. The test set-up and the measurement technique description are also given in Chapter 6 along with numerical simulations' description. A summary of contributions and conclusions of this research is given in Chapter 7.

2 CAVITY MODEL FOR A RECTANGULAR PIFA

2.1 Introduction

To accommodate physical insight and simplify the analysis of electromagnetic field distribution inside PIFA radiator, the configuration of the feeding structure is neglected here. The feed electromagnetic discontinuity will have a minor effect on the field configuration inside PIFA resonator, yet the boundary conditions at the edges of the cavity should remain intact.

The cavity model for the PIFA consists of a description of the region between the microstrip and the ground plane, bounded by perfect electric and magnetic walls along the edges and by perfect electric walls from above and below, loaded with a dielectric material of permittivity ϵ_r as shown in Figure 2.1.

The upper and the lower (the ground plane) plates of the cavity as well as the vertical shorting plate are assumed to be *perfect electric conductors* (PEC). All other vertical perimeter walls are treated as *perfect magnetic conductors* (PMC).

The ground plane surface is assumed to be infinite in extent. In reality, the ground plane is always finite; hence, a more accurate model should take into account the effects of finite ground plane. Such models exist and produce good results; the good example is *geometrical theory of diffraction* (GTD), [28]. However, the cavity model provides good results for big ground plane sizes (which is often the case for antenna arrays elements), and gives an adequate physical explanation of microstrip radiation mechanism.

Once the electric and magnetic fields inside the cavity are known, the radiated fields of the PIFA are found readily by replacing magnetic walls with equivalent radiating sources, using the vector potential theory and Maxwell equations e.g. [29].

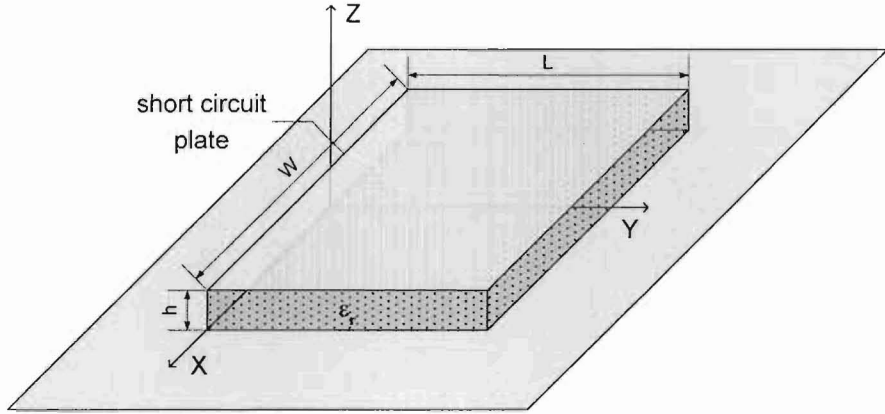


Figure 2.1 Cavity model for PIFA element shown with a finite ground plane.

Having found the far fields of the PIFA, many important characteristics of the antenna can be easily determined from there, such as radiated power, directivity, Q-factor, frequency bandwidth, input impedance etc.

2.2 PIFA field distribution (TM-modes)

Since the height of the microstrip is usually very small ($h \ll \lambda$, where λ is the wavelength inside the dielectric), the fields along the height of the PIFA are considered constant. Moreover, the fringing fields around the edges of the PIFA are also small because of the thin substrate. Therefore, the electric fields are considered to be normal to the surface of the PIFA patch. Consequently, only TM_{mn} (*transverse magnetic modes*) field configurations shall be considered in the model.

The cavity is treated as a lossless, source-free, linear, isotropic homogeneous media, in which the electric field satisfies the following condition (Appendices A-B):

$$\nabla^2 \bar{E} + k^2 \bar{E} = 0 \quad (2.1)$$

where \bar{E} - is the vector electric field, $k = 2\pi / \lambda$ is the wave number. Equation (2.1) is well known as the *homogeneous Helmholtz equation* [30].

The cavity resonator is defined such that its resonance length is in \hat{y} direction, i.e. cavity wave propagation is mostly \hat{y} directed. The boundary conditions for the electric walls (see Appendix 9.3) produce the electric field in the \hat{z} direction. As a result, the dominant modes excited in the PIFA cavity are TM_{mn} - modes.

Thus, with the fringing fields effect neglected, and the electric field depending only on \hat{y} , the equation (2.1) reduces to:

$$\frac{\partial^2 \bar{E}_z}{\partial y^2} + k^2 \bar{E}_z = 0, \quad (2.2)$$

and has a general solution (Appendix 9.2):

$$\bar{E}_z = E_1 e^{-jk_y y'} + E_2 e^{jk_y y'}, \quad (2.3)$$

here the primed coordinate denotes a source point.

The electric currents should be zero on the open end of the cavity ($y' = L$). From the electric current and magnetic field relation [30]:

$$\int_C \bar{H} \cdot d\bar{s} = \int_S \bar{J} \cdot d\bar{a}, \quad (2.4)$$

the magnetic fields at $y' = L$ should also be zero:

$$\bar{H}_{y'=L} = 0. \quad (2.5)$$

From the Maxwell equations (Appendix 9.1) we have:

$$\nabla \times \bar{E} = -j\omega\mu\bar{H}. \quad (2.6)$$

The curl in (2.6) can be evaluated yielding:

$$\nabla \times \bar{E} = \nabla \times \bar{E}_z = -\frac{\partial E_z}{\partial y} \hat{x}. \quad (2.7)$$

Upon inserting the boundary condition (2.5) into (2.7) we obtain:

$$\left(\frac{\partial E_z}{\partial y} \right)_{y'=L} = 0, \quad (2.8)$$

and evidently, the electric field is indeed finite at $y' = L$.

According to the electric wall boundary condition, the tangential electric field must disappear at the short circuit, thus, the boundary condition at $y' = 0$:

$$(E_z)_{y'=0} = 0. \quad (2.9)$$

Upon inserting the boundary condition (2.9) into (2.3) we obtain:

$$\bar{E}(y' = 0) = E_1 \hat{z} + E_2 \hat{z} = 0 \Rightarrow E_1 = -E_2. \quad (2.10)$$

Now, using Euler's identity, the general solution equation can be rewritten as follows:

$$\bar{E} = E_1 e^{-jk_y y'} \hat{z} - E_1 e^{jk_y y'} \hat{z} = -2jE_0 \sin k_y y' \hat{z}. \quad (2.11)$$

Taking the differential of (2.11) with respect to y and inserting the boundary condition from (2.8) yields:

$$\frac{\partial E_x}{\partial y} = (-j2kE_0 \cos k_y y')_{y=L} = -j2kE_0 \cos k_y L = 0. \quad (2.12)$$

The general solution of this equation is an infinite number of resonant modes:

$$k_y L = \pm \frac{\pi}{2} (2l + 1), \quad (2.13)$$

where k_y - is the wave number along y direction corresponding to each mode.

The lowest order resonant frequency mode is referred to as the *dominant (fundamental) mode* of the cavity. In the case of the PIFA resonator, the lowest radiating dominant mode is TM_{01} mode. Furthermore, solving for resonance length of the antenna, and choosing $l = 0$ for the smallest radiator size, we obtain:

$$L = \frac{\pi}{2k_y} = \frac{\lambda}{4} \quad (2.14)$$

Having defined all the properties and characteristics of the PIFA cavity, equation (2.11) can be used now as an approximation of the electric fields inside the cavity. Different modes of rectangular PIFA are depicted in Figure 2.2.

Similarly, the expression for the magnetic field inside the cavity can be found from the following Maxwell equation (Appendix 9.1):

$$\begin{aligned} \nabla \times \bar{E} &= -j\omega\mu\bar{H} \\ \Rightarrow \bar{H} &= -\frac{1}{j\omega\mu} \nabla \times \bar{E}. \end{aligned} \quad (2.15)$$

Performing the curl operator of \bar{E} in (2.11):

$$\nabla \times \bar{E} = -\hat{x} \left(\frac{\partial E_z}{\partial y} \right) = j2E_0 k \cos k_y y' \hat{x}, \quad (2.16)$$

and upon inserting (2.16) into (2.15) we finally obtain for the magnetic field:

$$\bar{H} = -\frac{k}{\omega\mu} 2E_0 \cos ky' \hat{x} = -\frac{1}{Z} 2E_0 \cos ky' \hat{x}, \quad (2.17)$$

where $Z = \sqrt{\mu/\epsilon}$ - intrinsic impedance, and $k = \omega\sqrt{\mu\epsilon}$.

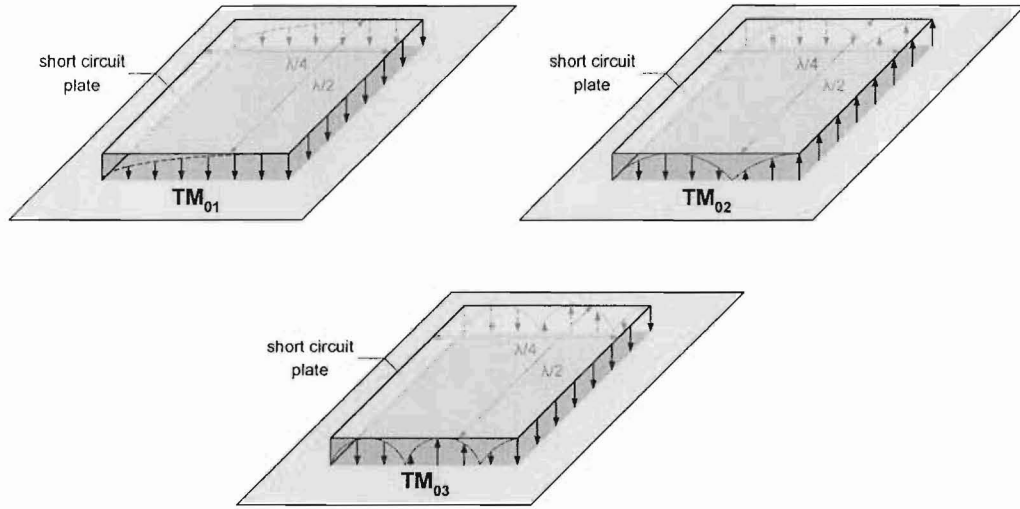


Figure 2.2 Electric field configurations (modes) for the rectangular PIFA.

It is apparent from the equation (2.17) that the tangential magnetic field equals to zero at the open ends of the cavity. However, in order to radiate electromagnetic energy, the power flux (*Poynting vector*) of the electromagnetic wave excited in the radiator $\bar{P} = \bar{E} \times \bar{H}^*$ has to have a nonzero value. The model has to be refined to account for this. In particular, the magnetic walls will be replaced with the equivalent magnetic sources, on the open ends of the PIFA, and their radiating characteristics will be found using the vector potential theory using Maxwell equations.

2.3 Equivalent magnetic currents

From the above analysis, it can be concluded that the PIFA resonator can be modeled as an equivalent microstrip cavity with perfect electric and magnetic conducting walls, loaded with the dielectric material. In reality, the substrate fields of the cavity do not always stop abruptly at the open edges of the resonator (see Chapters 5 and 6). Let us assume though, that the substrate of the antenna and corresponding fringing fields are truncated at the edges of the PIFA. Then, the three open sidewalls can be represented by three narrow apertures (slots) through which all the radiation of the antenna occurs.

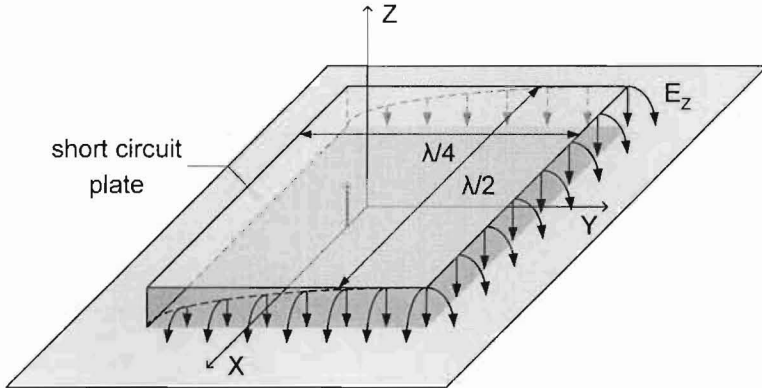


Figure 2.3 Dominant mode electric fields of the rectangular PIFA. Fringing fields of the dominant mode.

Having done that, the Huygens' equivalence principle can be applied now to the cavity radiating slots, replacing them with the following equivalent electric and magnetic current densities [29]:

$$\begin{aligned}\bar{J}_S &= \hat{n} \times \bar{H}_a \\ \bar{M}_S &= -\hat{n} \times \bar{E}_a,\end{aligned}\tag{2.18}$$

where \bar{H}_a and \bar{E}_a respectively represent the electric and magnetic fields of the slots.

It has also been shown in [29], that for a microstrip patch with very small height-to-width ratio, the tangential magnetic fields at the open edges of the cavity are very small, almost zero. Thus, the corresponding equivalent electric current densities \bar{J}_S are going to be very small as well, and will be set here to zero.

Therefore, the only nonzero current density is the magnetic current density \bar{M}_S which is, according to the preceding reasoning, located around the perimeter of the open slots of the PIFA resonator. Using *image theory* e.g. [1], this current density radiating in the close proximity of an infinite ground plane can be found by doubling the equivalent magnetic current density in (2.18):

$$\bar{M}_S = -2\hat{n} \times \bar{E}_a \quad (2.19)$$

Now, this radiating equivalent magnetic current density expression, along with the fields inside the cavity can be visualized as shown in Figure 2.4.

Furthermore, using the equivalence principle, each slot's magnetic current density radiates the same field as a magnetic dipole with magnetic current equal to (2.19). Upon replacing electric fields of the corresponding slots with equivalent magnetic currents given by (2.19) and using (2.11) (note the coordinate origin in the middle of the patch):

$$\bar{M}_1 = -(2\hat{y}) \times E_{a1}(-\hat{z}) = -2E_{a1}\hat{x}, \quad (2.20)$$

$$\bar{M}_2 = -(-2\hat{x}) \times E_{a2}(-\hat{z}) = -2E_{a2}\hat{y}, \quad (2.21)$$

$$\bar{M}_3 = -(2\hat{x}) \times E_{a3}(-\hat{z}) = 2E_{a3}\hat{y}, \quad (2.22)$$

we finally arrive at the PIFA equivalent magnetic currents expressions for the fundamental mode:

$$\bar{M}_1 = -2E_0 \hat{x}, \quad -W/2 \leq x \leq W/2, y = L/2, z = 0, \quad (2.23)$$

$$\bar{M}_2 = -2E_0 \sin(ky + \pi L/\lambda) \hat{y}, \quad x = -W/2, -L/2 \leq y \leq L/2, z = 0, \quad (2.24)$$

$$\bar{M}_3 = 2E_0 \sin(ky + \pi L/\lambda) \hat{y}, \quad x = W/2, -L/2 \leq y \leq L/2, z = 0. \quad (2.25)$$

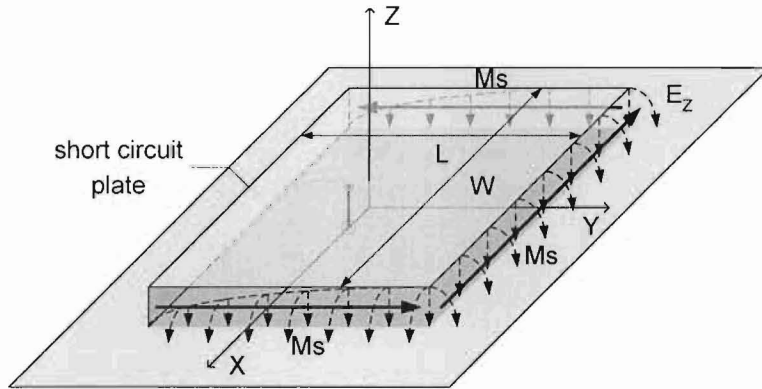


Figure 2.4 Rectangular PIFA radiating fields and their equivalent magnetic current densities.

The plan view of an equivalent magnetic source corresponding to the cavity model of the PIFA can be seen as in Figure 2.5.

As can be seen from the Figure 2.4 and Figure 2.5, the equivalent magnetic currents \bar{M}_2 and \bar{M}_3 are of the same magnitude and of the opposite phase. It is a common practice in the literature [20, 21, 30] to refer to these as *non-radiating slots* magnetic currents. Indeed, it is a valid assumption for a rectangular patch antenna, in which case the field structure of the corresponding cavity is different from the PIFA. The two sideslots of the patch antenna cancel each other in the far field in both principal planes of radiation. Even though this is not true for non-principal planes of radiation, it

does not have a major impact on the radiating characteristics of the rectangular patch except for introducing a systematic error in calculations.

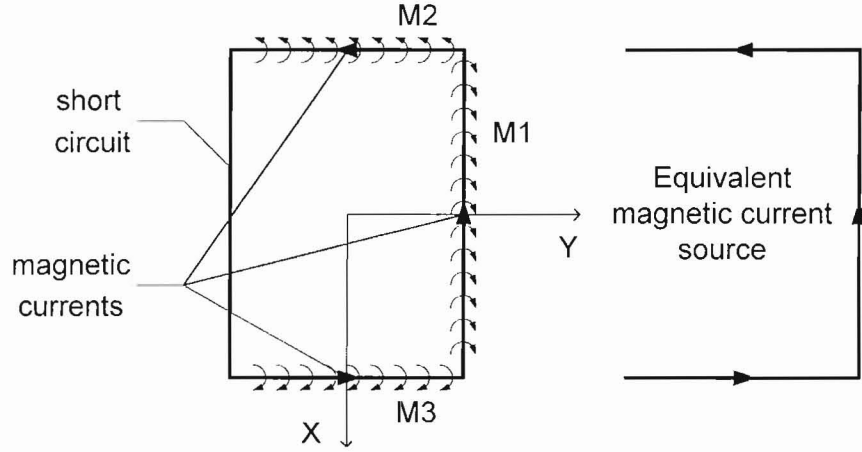


Figure 2.5 Equivalent magnetic current source of a rectangular PIFA.

However, in case of PIFA, not only the above assumption introduces a systematic error in calculations, but it also leads to wrong far field pattern behavior for the PIFA radiator, because of different cavity field structure in comparison to the conventional patch antenna. As it will be clear from the further analysis, the contribution of the sidelots of PIFA to the whole radiation pattern is significant comparing to the endslot contribution. Therefore, one of the goals of this analysis will be derivation of accurate expressions for PIFA far fields as well as comparison of an impact it has on main PIFA characteristics.

2.4 PIFA radiating far fields derivation

In this section, the far fields of each of three slots will be derived assuming the model just described. Firstly, the far field contribution of the PIFA endslot will be derived using the electric vector potential theory. Secondly, the far field contribution of each of the PIFA sideslots will be determined using the same approach. Thirdly, the combined contribution of the two sideslots will be obtained using the antenna array concept. Finally the overall PIFA far field will be determined as a combination of the contributions just derived.

2.4.1 End slot contribution to the far field of PIFA

The general expression for the electric vector potential of a magnetic current density can be written as follows [31]:

$$\bar{F} = \frac{\epsilon}{4\pi} \iiint_V \bar{M}_V \frac{e^{-jkR}}{R} dv', \quad (2.26)$$

where \bar{M}_V - is volume magnetic current density, $R = |r - r'|$ with r - as an observation point, and r' - as a source point.

In the assumption of a very small cavity height compared to a wavelength, for the endslot filament magnetic current, the volume integral reduces to a line integral. Using the far field approximation (Appendix 9.5) yields:

$$\bar{F}_1 = \frac{\epsilon_0}{4\pi} 2V \frac{e^{-jk_0 r}}{r} \hat{x} \int_{-W/2}^{W/2} e^{jk_0 x \sin \theta \cos \varphi} dx = \frac{\epsilon_0}{2\pi} V \frac{e^{-jk_0 r}}{r} W \left(\frac{\sin U_W}{U_W} \right) \hat{x}, \quad (2.27)$$

where $U_W = \frac{k_0 W}{2} \sin \theta \cos \varphi$. The integral was solved by using the well known expression of *Fresnel integral* [32].

In terms of spherical coordinates (Appendix 9.4), the components of \bar{F}_l will look like:

$$F_{lr} = \bar{F}_l \cdot \hat{r} = F_{lx} \sin \theta \cos \varphi, \quad (2.28)$$

$$F_{l\theta} = \bar{F}_l \cdot \hat{\theta} = F_{lx} \cos \theta \cos \varphi, \quad (2.29)$$

$$F_{l\varphi} = \bar{F}_l \cdot \hat{\varphi} = -F_{lx} \sin \varphi. \quad (2.30)$$

These vector potentials can be used to find the far fields from the Maxwell equations (Appendix 9.1):

$$\bar{E} = -\frac{1}{\epsilon_0} \nabla \times \bar{F}. \quad (2.31)$$

Finally, using the definition of the curl operator in the spherical coordinates (Appendix 9.4), the far electric field expressions for the PIFA endslot become:

$$E_{l\theta} = KW \frac{\sin U_W \sin \varphi}{\pi \sin \theta \cos \varphi}, \quad (2.32)$$

$$E_{l\varphi} = KW \frac{\sin U_W \cos \theta}{\pi \sin \theta}, \quad (2.33)$$

where $K = \frac{\epsilon_0 V}{2\pi} \frac{e^{-jk_0 r}}{r}$.

Usually, the height of microstrip structures is very small comparing to the wavelength in the substrate. Therefore, the similar height term $\sin(U_h)/U_h$ in the far

field expression is approaching unity with h approaching zero e.g. [21], and hence may be neglected without loss of accuracy. Also, as can be seen from these far field expressions, the electric field pattern of the end slot of PIFA by itself is that of single magnetic dipole, leading to the dipole-like E -pattern [19].

2.4.2 Side slot contribution to the far field of PIFA

As it was mentioned earlier, the contribution of side slots of PIFA to the far field is quite significant and cannot be neglected without loss of accuracy.

The far field expression for single PIFA sideslot can be derived in a similar manner using the electric potential theory. Again, in the assumption of a very small cavity height, the sideslot filament magnetic current volume integral reduces to a line integral. Thus, in the far field:

$$F_2 = \frac{\epsilon_0}{4\pi} 2V \frac{e^{-jk_0r}}{r} \int_{-L/2}^{L/2} \sin\left(k_0y + \frac{\pi L}{\lambda}\right) e^{jk_0y \sin\theta \sin\varphi} dz \hat{y} = \frac{\epsilon_0}{2\pi} V \frac{e^{-jk_0r}}{r} \\ \times \left\{ \frac{e^{jk_0y \sin\theta \sin\varphi}}{(k_0)^2 + (jk_0 \sin\theta \sin\varphi)^2} \left[(jk_0 \sin\theta \sin\varphi) \sin\left(k_0y + \frac{\pi L}{\lambda}\right) \right. \right. \\ \left. \left. + k_0 \cos\left(k_0y + \frac{\pi L}{\lambda}\right) \right] \right\}_{-L/2}^{L/2} \hat{y}, \quad (2.34)$$

which for $L = \lambda/4$ (rectangular PIFA) can be easily simplified to:

$$F_2 = \frac{\epsilon_0}{2\pi} V \frac{e^{-jk_0r}}{r} \left(\frac{1}{(k_0)^2 + (jk_0 \sin\theta \sin\varphi)^2} \right) \times \left[jk_0 \sin\theta \sin\varphi e^{\frac{k_0 L}{2} \sin\theta \sin\varphi} \right. \\ \left. + k_0 e^{-\frac{j k_0 L}{2} \sin\theta \sin\varphi} \right] \hat{y}. \quad (2.35)$$

The integral was solved by using the well known expression for the integral of combination of trigonometric and exponential function in [32].

Similarly, in terms of spherical coordinates (Appendix 9.4), the components of \bar{F}_2 will look like:

$$F_{2r} = \bar{F}_2 \cdot \hat{r} = F_{2y} \sin \theta \sin \varphi, \quad (2.36)$$

$$F_{2\theta} = \bar{F}_2 \cdot \hat{\theta} = F_{2y} \cos \theta \sin \varphi, \quad (2.37)$$

$$F_{2\varphi} = \bar{F}_2 \cdot \hat{\varphi} = F_{2y} \cos \varphi. \quad (2.38)$$

Finally, these vector potentials can be used in a similar manner to find the far fields of each of the sideslots of PIFA from the Maxwell equation in (2.31) by applying the curl operator in the spherical coordinates:

$$E_2 = E_3 = E_{2\cap 3\theta} = -K \frac{(jk_0 \sin \theta \sin \varphi e^{jU_L} + k_0 e^{-jU_L}) \cos \varphi}{(k_0)^2 + (jk_0 \sin \theta \sin \varphi)^2}, \quad (2.39)$$

$$E_2 = E_3 = E_{2\cap 3\varphi} = -K \frac{(jk_0 \sin \theta \sin \varphi e^{jU_L} + k_0 e^{-jU_L}) \cos \theta \sin \varphi}{(k_0)^2 + (jk_0 \sin \theta \sin \varphi)^2}, \quad (2.40)$$

where the same notation was used and $U_L = \frac{k_0 L}{2} \sin \theta \sin \varphi$.

As it was before, in this analysis the term accounting for a finite patch height was neglected having almost no effect on the PIFA far fields.

Having found the far field contribution for each of the sideslots of PIFA cavity, it is now possible to find the combined two-slot contribution to the PIFA far field. It can be done using the array factor concept.

2.4.3 Combined side slot contribution to the far field of PIFA using array factor concept

In order to find combined side slots contribution to PIFA far field, a linear array of two magnetic currents \bar{M}_2 and \bar{M}_3 may be considered (Figure 2.6). According to an array theory, this basic antenna array configuration can be represented in the far field by two parts: the pattern of one of the elements of the array by itself, - an *element pattern*, and the pattern of the array of two isotropic point sources, representing the actual elements , - an *array factor* e.g. [28].

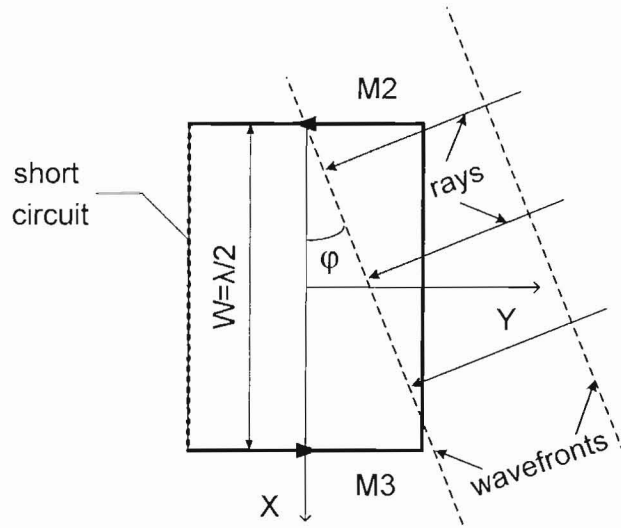


Figure 2.6 Linear array arrangement of side slot equivalent magnetic currents for rectangular PIFA.

The array factor of corresponding linear array is found upon replacing each magnetic current source by an isotropic radiator, retaining its spatial location and excitation. Let us assume two point sources aligned along the x axis according to PIFA sideslots arrangement (Figure 2.6, Figure 2.7). They are separated by a distance $W = \lambda/2$ in case of rectangular PIFA radiator.

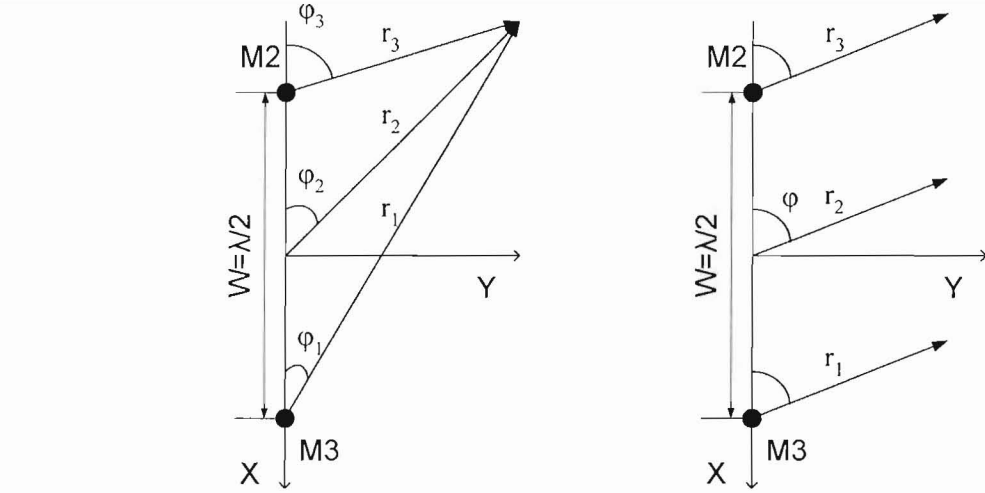


Figure 2.7 Two isotropic point sources with identical amplitudes spaced one-half wavelength apart: near field (left) and far field (right) observation.

In the far field, it is clear from the Figure 2.7, that:

$$\varphi_1 \equiv \varphi_2 \equiv \varphi_3 \quad (2.41)$$

The array is receiving a plane front wave at an angle φ . The direction of travel of the wave is indicated by the rays perpendicular to the wave front. In this arrangement, the distance to each element has a corresponding phase delay $e^{j\gamma_i}$. Assuming equal amplitude excitation, taken to be unity, the total far field contribution from these point sources will become:

$$\bar{E} = I_1 e^{j\gamma_1} + I_3 e^{j\gamma_3}, \quad (2.42)$$

where $I_i = \frac{e^{-jk_0 r_i}}{r_i}$.

From the equivalent magnetic currents analysis and from Figure 2.6 it is evident that the one source is 180° out of phase with the other. Therefore, the expression for the total far field contribution of two isotropic point magnetic sources with opposite phases becomes:

$$\bar{E} = -I_1 e^{-jk_0 \frac{W}{2} \sin \theta \cos \varphi} + I_1 e^{jk_0 \frac{W}{2} \sin \theta \cos \varphi} \quad (2.43)$$

Finally, from the last equation, using the *Euler identity*, the expression for the array factor of two isotropic point magnetic sources with identical amplitudes and opposite phases may be found as:

$$\begin{aligned} AF &= -1 \cdot e^{-jk_0 \frac{W}{2} \sin \theta \cos \varphi} + 1 \cdot e^{jk_0 \frac{W}{2} \sin \theta \cos \varphi} = 2j \sin(k_0 \frac{W}{2} \sin \theta \cos \varphi) \\ &= 2j \sin(U_W) \end{aligned} \quad (2.44)$$

Now, the combined field from both PIFA sideslots can be obtained by the array pattern multiplication rule [28]:

$$E_{tot} = E[\text{one element}] \times AF \quad (2.45)$$

2.4.4 Total PIFA radiated fields using array theory

Having determined all the necessary contributions to PIFA far fields it is now possible to obtain total radiated fields of the antenna.

For the PIFA operating with the basic rectangular TM_{01} mode, the far fields are found as:

$$E_\theta = E_{1\theta} + E_{2\cup 3\theta} = KW \frac{\sin U_W \sin \varphi}{\pi \sin \theta \cos \varphi} + E_{2\cap 3\theta} \cdot 2j \sin(U_W), \quad (2.46)$$

$$E_\varphi = E_{1\varphi} + E_{2\cup 3\varphi} = KW \frac{\sin U_W \cos \theta}{\pi \sin \theta} + E_{2\cap 3\varphi} \cdot 2j \sin(U_W), \quad (2.47)$$

where $E_{2\cap 3\theta}$ and $E_{2\cap 3\varphi}$ are as per (2.39) and (2.40) respectively, with:

$$U_W = \frac{k_0 W}{2} \sin \theta \cos \varphi, \quad (2.48)$$

$$U_L = \frac{k_0 L}{2} \sin \theta \sin \varphi, \quad (2.49)$$

and $K = \frac{\epsilon_0 V}{2\pi} \frac{e^{-jk_0 r}}{r}$, with V - patch voltage.

The far field patterns according the above expressions are furnished in Figure 2.8 along with the experimental data for rectangular PIFA from [4]. As can be seen from the plots the agreement between this theoretical model and experiment results is very good except for low elevation angles, where the obvious finite ground plane diffraction effects distort the pattern slightly. The diffraction at the edges of the ground plane appears in particular in the oscillations of principal components in both planes of radiation for elevation angles below 80° .

In the XZ plane (H -plane) the PIFA's endslot demonstrates the usual doughnut shape radiation pattern behavior of magnetic dipole with E_φ -field component being zero on the ground plane. Also, E_θ -field contribution of the endslot equivalent magnetic current along x axis is identically zero. However, for H -plane, the radiated field of the two sideslots located along the y axis gives a high level of E_θ -field radiation with a null in the broadside direction (because of the cancellation effect of out-of-phase magnetic currents in the far field). As can be readily seen from the E_θ field in the H -plane, the

effect of sideslot radiation on PIFA far field pattern is very significant giving almost the same electric field magnitude contribution as the endslot of the antenna.

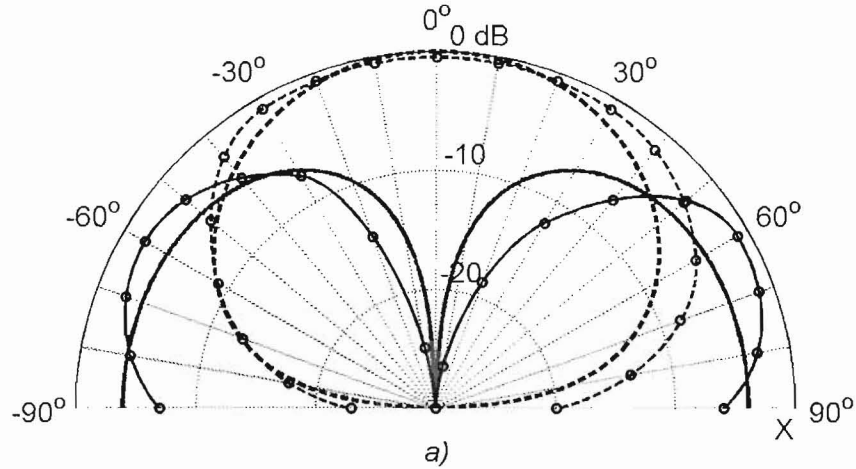


Figure 2.8 XZ plane (H plane) far field patterns for an example of the rectangular PIFA ($W = \lambda/2, L = \lambda/4$).

— E_θ , --- E_ϕ (this theory)
 —o— E_θ , --o-- E_ϕ (data from [4])

In the YZ plane (E -plane), however, the uniform endslot aperture dominates the pattern producing an omnidirectional E_θ -field radiation. The sideslots' contribution to the E_ϕ -field is zero because of the same far field cancellation effect produced by the two out-of-phase magnetic currents.

A minor tilt to the right of the experiment patterns in the H plane comparing to the theoretical ones must be attributed to either mechanical imperfections of the measured prototype and/or measurement environment (anechoic chamber), or some inaccurateness in the measurements process.

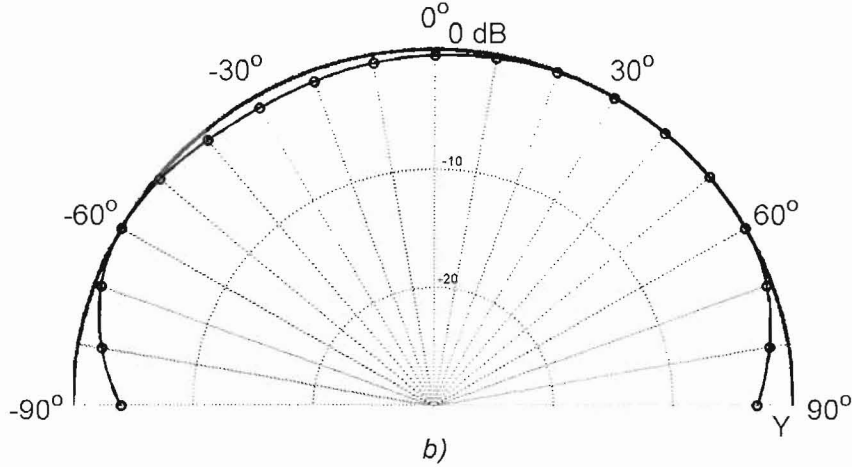


Figure 2.9 YZ plane (E plane) far field patterns for an example of the rectangular PIFA ($W = \lambda/2$, $L = \lambda/4$).

— E_θ , - - - E_ϕ (this theory)
 —○— E_θ , --○-- E_ϕ (data from [4])

It is also of interest to compare the results of this model to those of numerical techniques, such as Method of Moments or FDTD. In particular, the far field results of commercially available solver CST Microwave Studio (FDTD) are presented in Figure 2.10 - Figure 2.12 and along with the cavity model results. The rectangular PIFA was prototyped in CST of brass plates of thickness $t=1.7\text{mm}$ ($\lambda/181$) and an infinite groundplane. The inner height of the cavity was very small with $h=1\text{mm}$ ($\lambda/308$) in order to retain the PIFA's modal purity.

A reasonable agreement (less than ± 1.5 dB) of the cavity theory with numerical results provided by CST is evident. This difference is in directions along the groundplane corresponding to where the groundplane slot model is least robust.

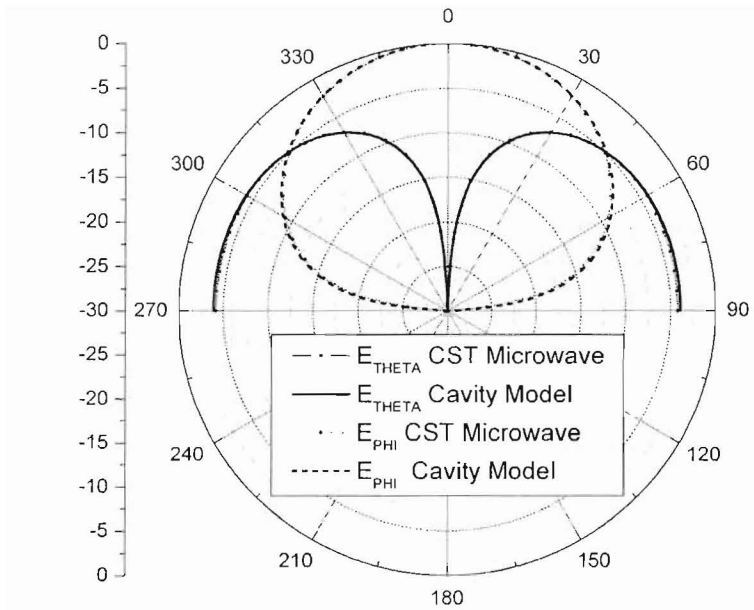


Figure 2.10 XZ plane (H plane) far field pattern for an example of the rectangular PIFA ($W = \lambda / 2, L = \lambda / 4$).

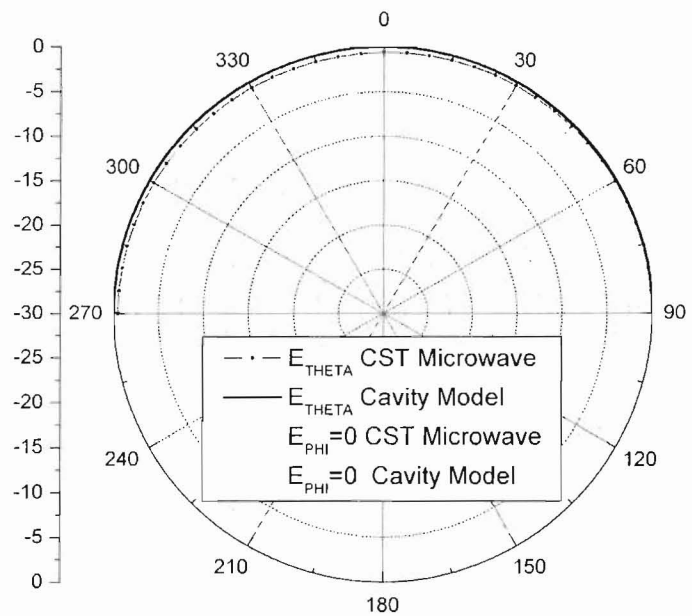


Figure 2.11 YZ plane (E plane) far field pattern for an example of the rectangular PIFA ($W = \lambda / 2, L = \lambda / 4$).

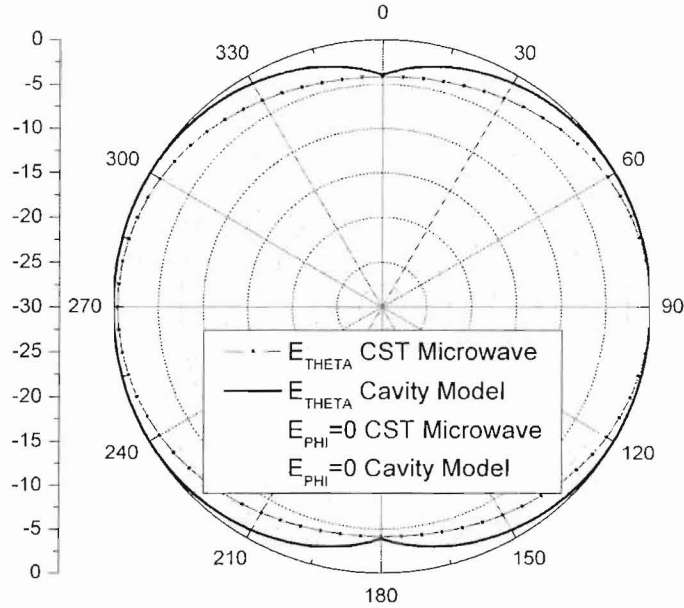


Figure 2.12 XY plane (Ground plane) far field pattern for an example of the rectangular PIFA ($W = \lambda/2$, $L = \lambda/4$).

To further illustrate an impact of side slots radiation, the total far field pattern according to this model and the classic single end-slot model described in [19] is presented in the Figure 2.13. Even though in the E -plane both patterns are identically omnidirectional, in the H -plane, the differences in the far fields between the two models reach up to about 20 dB for low elevation angles. So the ubiquitous assumption for the PIFA far field being the same as that of the end-slot only is not well justified as alluded to in [19]. As demonstrated here, this assumption only applies for the YZ cut.

As a result, the theoretical model for PIFA cavity just presented can be regarded as a more accurate tool for predicting PIFA far field pattern behavior and can be successfully used in the analysis of this type of radiation structure.

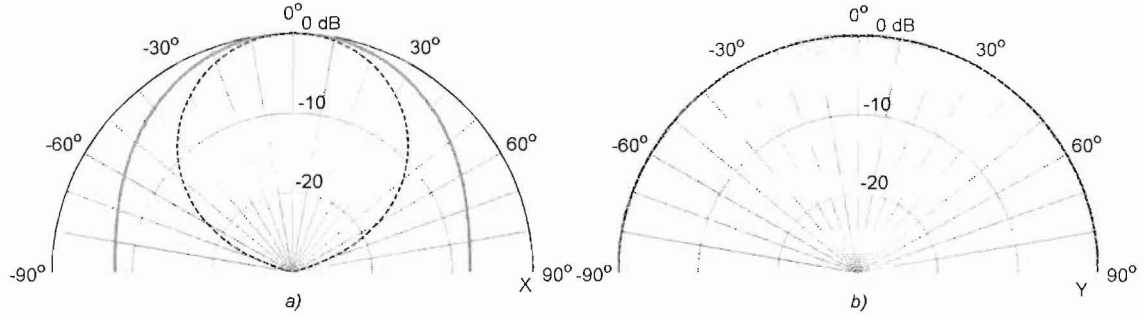


Figure 2.13 Principal planes total far field patterns for an example of the rectangular PIFA ($W = \lambda / 2$, $L = \lambda / 4$).

— E_{tot} (this theory), - - - E_{tot} (ibid.) - one slot model
a) XZ plane (H plane); b) YZ plane (E plane).

2.5 Enhanced model for PIFA magnetic currents and far fields

Using the model just described, in the following subsections, several important characteristics will be derived for the PIFA, such as Q-factor, frequency bandwidth and impedance. Yet before that, it is of interest to study the influence of the form of the end slot equivalent magnetic current on the PIFA far field pattern behavior.

Indeed, the exact distribution of EM energy across the end slot is not known. It is not unreasonable to assume that this distribution is not uniform. Moreover, experimental data from (Sections 4, 5, 6) suggest that the distribution may be described as a cosine-on-pedestal type function. This assumption will obviously impact the calculated far fields of the PIFA.

Instead of uniform illumination, the endslot and the sideslots magnetic currents are now expressed as:

$$\bar{M}_1 = -[C2E_0 + (1-C)2E_0 \cos(\pi x/L)]\hat{x}, \quad (2.50)$$

$$-W/2 \leq x \leq W/2, y = L/2, z = 0;$$

$$\bar{M}_2 = -C2E_0 \sin(ky + \pi L/\lambda) \hat{y}, \quad x = -W/2, -L/2 \leq y \leq L/2, z = 0; \quad (2.51)$$

$$\bar{M}_3 = C2E_0 \sin(ky + \pi L/\lambda) \hat{y}, \quad x = W/2, -L/2 \leq y \leq L/2, z = 0; \quad (2.52)$$

where C is a pedestal size parameter determined by the PIFA electrical dimensions.

For $C = 0$, there is no pedestal and there is a purely cosine form at the endslot. For $C = 1$, there is a uniformly illuminated endslot. Furthermore, this pedestal C appears in the sideslots' magnetic currents expressions as a scaling factor. For larger values of C the amplitude of the magnetic currents from the sideslots grows larger as well. Therefore, $C = 0$ corresponds to zero sideslots magnetic currents, i.e. no sideslot contribution to the far field, while $C = 1$ enhances the model to the case of PIFA with uniform endslot and sinusoidal sideslots, which was described in the preceding analysis.

This model is more general and more flexible in describing the PIFA far field pattern behavior, yet it does not add much to the physical insight of the radiation mechanism of PIFA. Also, the non-uniformity of the endslot assumption may not necessary hold in the real PIFA behavior and it needs to be applied with proper care.

In a similar fashion, the far fields due to these refined magnetic currents can be found from the contributing vector potentials:

$$E_\theta = E_{1\theta} + E_{2\cup 3\theta} = K \left\{ C \left(\frac{\sin U_W}{U_W} \right) + (1-C) \frac{2 \cos U_W}{\pi \left[1 - (2U_W/\pi)^2 \right]} \right\} \\ \times \sin \varphi / [C + (1-C)2/\pi] + CE_{2\cap 3\theta} \cdot 2j \sin(U_W) \quad (2.53)$$

$$E_\varphi = E_{1\varphi} + E_{2\cup 3\varphi} = K \left\{ C \left(\frac{\sin U_W}{U_W} \right) + (1-C) \frac{2 \cos U_W}{\pi \left[1 - (2U_W/\pi)^2 \right]} \right\} \\ \times \cos \theta \cos \varphi / [C + (1-C)2/\pi] + CE_{2\cap 3\varphi} \cdot 2j \sin(U_W) \quad (2.54)$$

where the corresponding expressions from (2.46) - (2.49) were used.

Figure 2.14 illustrates the influence of the scale factor C on the far field patterns of PIFA in the ground plane (XY -plane).

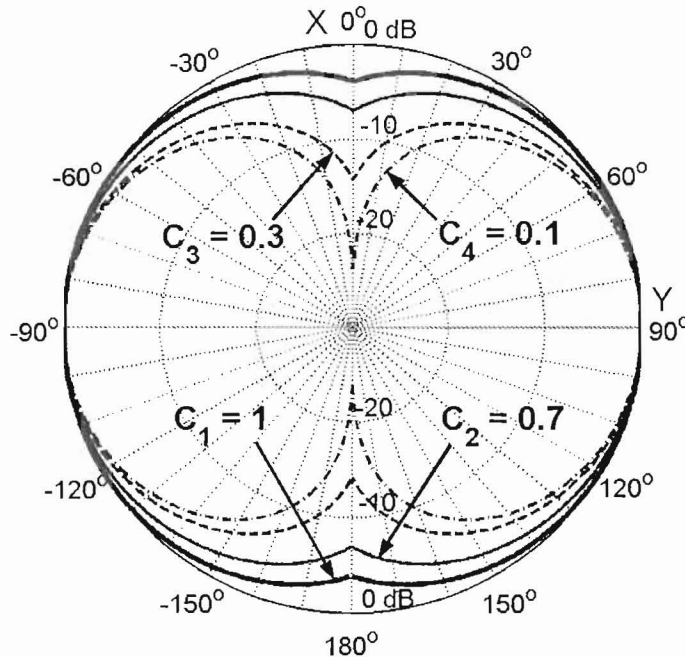


Figure 2.14 Rectangular PIFA far field patterns in the XY plane for different values of the end slot illumination pedestal ‘height’.

$C = 1$ corresponds to a “pedestal only”, i.e., a uniformly illuminated end slot.

$C = 0$ corresponds to a cosine illumination.

As can be seen from this plot, with a decreasing pedestal presence, and an associated decrease in the illumination of the sideslots, the PIFA’s end slot increasingly dominates the far field, bringing the PIFA pattern to the doughnut shape of the magnetic dipole with a sinusoidal current. For bigger values of C , or increasingly uniform endslot, the increasing presence of the side slots changes the pattern significantly.

Similar type of function, which can be used in description of the endslot instead of uniform illumination, is a negative cosine on a pedestal. Now, the end slot and the side slots magnetic currents are expressed as:

$$\bar{M}_1 = -[2E_0 - (1-C)2E_0 \cos(\pi x/L)]\hat{x}, \quad (2.55)$$

$-W/2 \leq x \leq W/2, y = L/2, z = 0;$

$$\bar{M}_2 = -2E_0 \sin(ky + \pi L/\lambda)\hat{y}, \quad x = -W/2, -L/2 \leq y \leq L/2, z = 0; \quad (2.56)$$

$$\bar{M}_3 = 2E_0 \sin(ky + \pi L/\lambda)\hat{y}, \quad x = W/2, -L/2 \leq y \leq L/2, z = 0; \quad (2.57)$$

where C is a pedestal size parameter determined by the PIFA electrical dimensions.

In this case, similarly, for $C = 0$, there is no pedestal associated with the endslot, and there is a purely negative cosine illumination with the voltage maximums at either edges of the slot. Also, for $C = 1$, there is a purely uniformly illuminated endslot. However, the C does not appear in the sideslots magnetic currents expressions as a scaling factor anymore. This means that changes of C do not influence the amplitudes of the magnetic currents from either of sideslots. Therefore, in this formulation, the sideslots' influence on the PIFA far fields is always present.

In a very similar fashion, the far fields due to these magnetic currents can now be found from the corresponding contributing vector potentials as follows:

$$E_\theta = E_{1\theta} + E_{2\cup 3\theta} = K \left\{ \left(\frac{\sin U_W}{U_W} \right) - (1-C) \frac{2 \cos U_W}{\pi [1 - (2U_W/\pi)^2]} \right\} \times \sin \varphi / [C + (1-C)2/\pi] + E_{2\cap 3\theta} \cdot 2j \sin(U_W) \quad (2.58)$$

$$E_\varphi = E_{1\varphi} + E_{2\cup 3\varphi} = K \left\{ \left(\frac{\sin U_W}{U_W} \right) - (1-C) \frac{2 \cos U_W}{\pi [1 - (2U_W/\pi)^2]} \right\} \\ \times \cos \theta \cos \varphi / [C + (1-C) 2/\pi] + CE_{2\cap 3\varphi} \cdot 2j \sin(U_W) \quad (2.59)$$

where the corresponding expressions from (2.46) - (2.49) were used as well.

Figure 2.15 illustrates the influence of the negative pedestal factor C on the far field patterns of PIFA in the ground plane (XY -plane).

It can be concluded from this plot that with a decreasing pedestal factor, the shape of far field pattern of the PIFA changes slightly. The changes of the far field shape in the XY plane are not significant comparing to those in the positive pedestal case, due to the constant presence of the sideslots. The case when the C is equal to 0 produces almost symmetrical pattern, which can be explained by the fact that the half-wavelength endslot can be thought of as an equivalent combination of the two quarter wavelength sinusoidal slots. These equivalent slots' contribution to the far field is almost the same to those, produced by the two PIFA's sideslots.

In practice, for single element PIFA on a compact terminal, the finite ground plane and the form of the mounting structure will have a larger impact than the differences resulting from the modeling improvements presented here. However, in an array where there is effectively a larger, or at least a more controlled ground plane presence, the improved element model allows better accuracy for both the mutual coupling and pattern calculations.

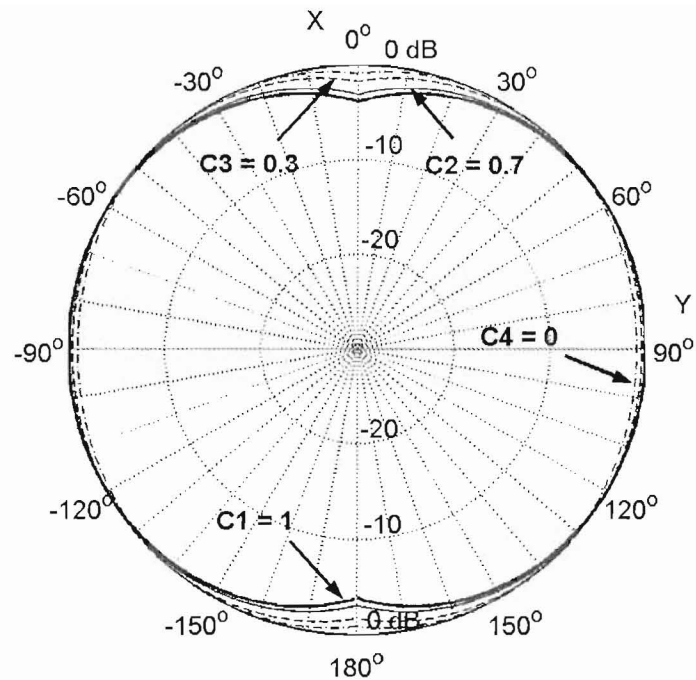


Figure 2.15 Rectangular PIFA far field patterns in the XY plane for different values of the end slot illumination negative pedestal ‘height’.

C = 1 corresponds to a “pedestal only”, i.e., a uniformly illuminated end slot.

C = 0 corresponds to a pure negative cosine illumination of the endslot.

3 CAVITY MODEL FOR A SEMICIRCULAR PIFA

3.1 Introduction

As it was for rectangular PIFA, to accommodate physical insight and simplify the analysis of electromagnetic field distribution inside semicircular PIFA radiator, the configuration of feeding structure is neglected here. Also, all the assumptions made about the boundary conditions at the edges of the rectangular PIFA cavity, perfect conductor materials, and ground plane infinite size, will remain intact for the semicircular PIFA.

The cavity model for semicircular PIFA consisting of the region between the microstrip and the ground plane, bounded by perfect electric and magnetic walls along the edges and by perfect electric walls from above and below, loaded with a dielectric material of permittivity ϵ_r , as shown in Figure 3.1.

3.2 Semicircular PIFA field distribution (TM-modes)

Again, using the small height assumption ($h \ll \lambda$), the semicircular PIFA's electric fields are considered to be normal to the surface of the PIFA patch. Therefore, only *TM*-modes field configurations will be considered in this model as well.

Similarly to the rectangular PIFA cavity, the boundary conditions for the electric walls of semicircular PIFA in homogeneous Helmholtz equation (2.1) produce the electric field in the \hat{z} direction (see Appendix 9.3). As a result, the dominant modes excited in the semicircular PIFA cavity are also TM_{mn} - modes.

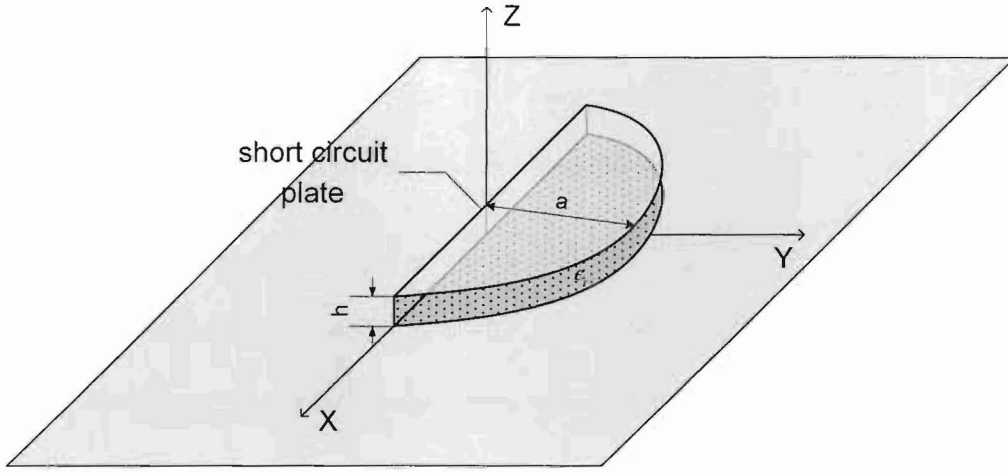


Figure 3.1 Cavity model for semicircular PIFA element with an infinite ground plane.

With the fringing fields effect neglected, similarly to the rectangular cavity case, the solution of the equation (2.1) for the semicircular cavity in cylindrical coordinates can now be found as:

$$\bar{E}_z = E_0 J_n(k\rho) \sin n\varphi, \quad (3.1)$$

for the electric field, and:

$$\bar{H}_\rho = \frac{jn}{\omega\mu\rho} E_0 J_n(k\rho) \cos n\varphi, \quad (3.2)$$

$$\bar{H}_\varphi = -\frac{jk}{\omega\mu} E_0 J'_n(k\rho) \sin n\varphi, \quad (3.3)$$

for the magnetic field. Here, $J_n(k\rho)$ denotes Bessel function of order n , $J'_n(k\rho)$ - its first derivative with respect to the argument $k\rho$, $0 \leq \rho \leq a$, where a is the antenna radius, and φ is changing between 0 and π .

The other cavity fields are equal to zero, i.e.

$$\bar{E}_\rho = \bar{E}_\varphi = \bar{H}_z = 0 \quad (3.4)$$

As it was for the rectangular PIFA, the general solution of this equation is an infinite number of resonant modes.

In case of the semicircular PIFA resonator, the lowest radiating dominant mode is TM_{11} mode.

Having defined all the properties and characteristics of the semicircular PIFA cavity, equation (3.1) can be used now as an approximation of the electric fields inside the cavity. Different modes of semicircular PIFA are depicted in Figure 3.2.

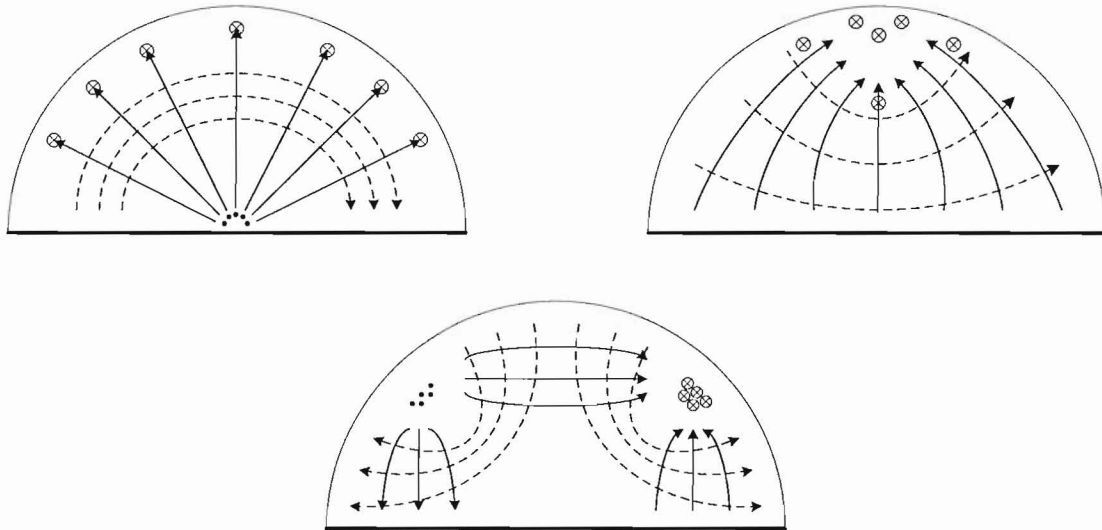


Figure 3.2 Electric field configurations (modes) for the semicircular PIFA.

- > currents on the top patch;
- - -> magnetic fields;
- × electric fields.

Similarly to the rectangular PIFA case, the tangential magnetic field equals zero at the open ends of the cavity. However, in order to radiate electromagnetic energy, the

power flux (Poynting vector) of the electromagnetic wave excited in the radiator $\bar{P} = \bar{E} \times \bar{H}$ has to have a nonzero value. This issue was mentioned earlier, and hence, this model has to be refined to account for this in the similar manner as it was done with the rectangular PIFA cavity. In particular, the magnetic walls will be replaced with the equivalent magnetic sources, representing fringing radiation on the open ends of the PIFA, and their radiating characteristics will be found using the vector potential theory using Maxwell equations.

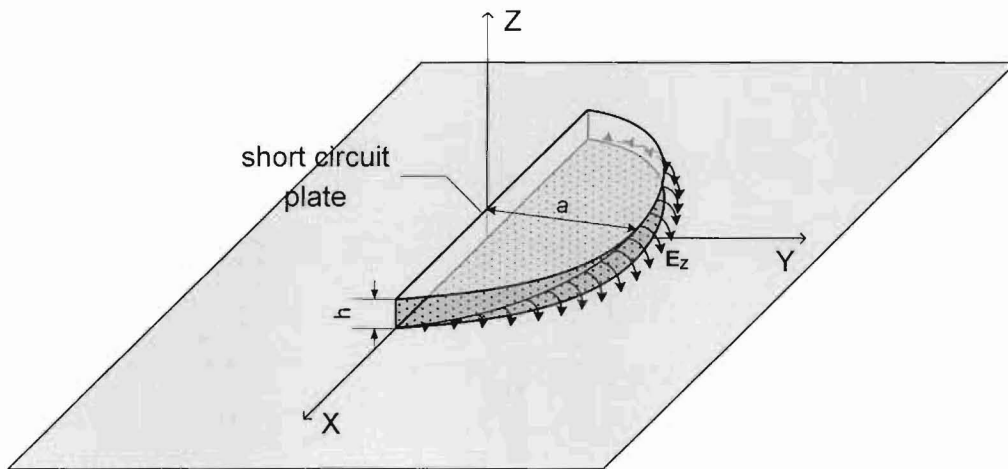


Figure 3.3 Dominant mode electric field of the semicircular PIFA. Fringing fields of the dominant mode.

3.3 Equivalent magnetic currents

From the above analysis, it can be concluded that the semicircular PIFA resonator can be modeled successfully as an equivalent microstrip cavity with perfect electric and magnetic conducting walls, loaded with the dielectric material. Following the reasoning outlined for the rectangular PIFA case, applying the equivalence Huygens' Principle to

the semicircular cavity radiating slot, and replacing it with the following equivalent electric and magnetic current densities [29]:

$$\bar{J}_S = \hat{n} \times \bar{H}_a = 0, \quad (3.5)$$

$$\bar{M}_S = -2\hat{n} \times \bar{E}_a \quad (3.6)$$

can be found, where \bar{H}_a and \bar{E}_a respectively represent the electric and magnetic fields of the slot.

The equivalent magnetic current density in (3.6) along with the fields inside the cavity can be visualized as shown in Figure 3.4:

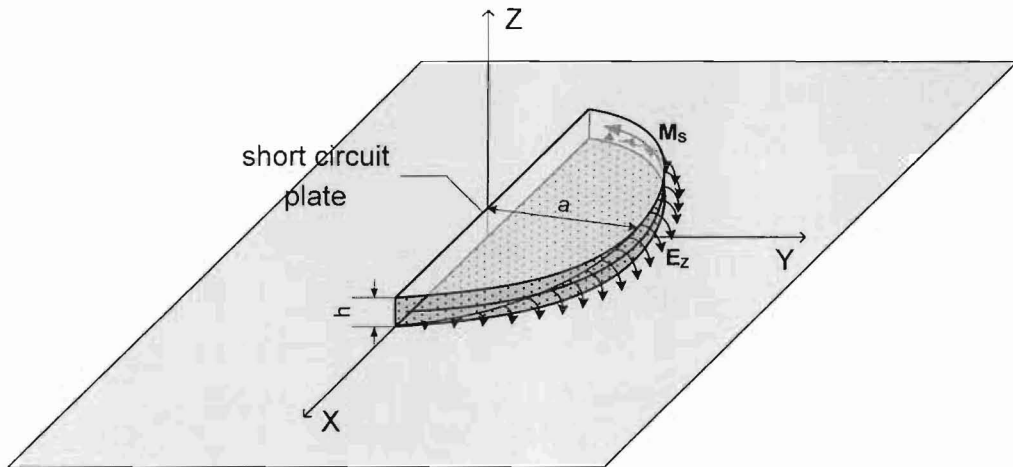


Figure 3.4 Semicircular PIFA radiating field and its respective equivalent magnetic current density.

Furthermore, using the equivalence principle, the open slot's magnetic current density radiates the same field as a half of a magnetic loop with its current equal to (3.6). Upon replacing electric fields of the corresponding slots with equivalent magnetic

currents given by (3.6) and using (3.1) (note the coordinate origin in the middle of the short circuit):

$$\bar{M} = 2\bar{E}_a \times \hat{\rho} = E_Z \hat{\phi} = \hat{\phi} \sum_{n=0}^{\infty} E_n J_n(k\rho) \sin n\varphi \quad (3.7)$$

the PIFA equivalent magnetic currents expressions for the fundamental mode become:

$$\bar{M} = \hat{\phi} E_1 J_1(k\rho) \sin \varphi, \quad 0 \leq \varphi \leq \pi, \quad \rho = a \quad (3.8)$$

Ultimately, the plan view of an equivalent magnetic source corresponding to the cavity model of the PIFA can be shown as in Figure 3.5:

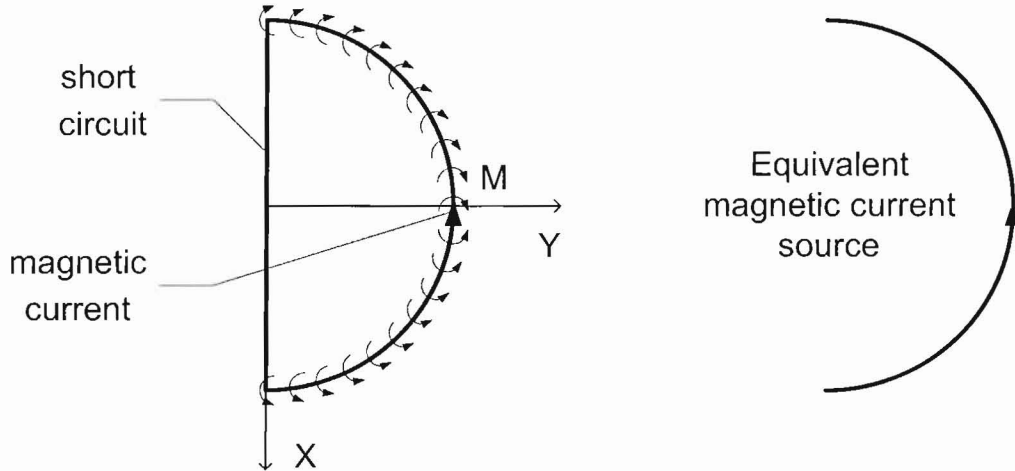


Figure 3.5 Equivalent magnetic current source of semicircular PIFA.

As can be seen from the Figure 3.4 and Figure 3.5, the equivalent semicircular magnetic current \bar{M} now solely represents the radiation mechanism of the corresponding PIFA structure. This magnetic current is sinusoidal and can be best analyzed in polar coordinates. In the next section, vector potential analysis will be applied to the magnetic

current in order to find out the far field pattern behavior of the semicircular PIFA antenna.

3.4 PIFA radiating far fields derivation

In this section, the far field of open slot of the semicircular PIFA will be determined assuming the model just described.

The general expression for the electric vector potential of a magnetic current density can be written as follows [31]:

$$\bar{F} = \frac{\epsilon}{4\pi} \iiint_V \bar{M}_V \frac{e^{-jkR}}{R} dv' \quad (3.9)$$

where \bar{M}_V - is volume magnetic current density, $R = |r - r'|$ with r - as an observation point, and r' - as a source point.

In the assumption of a very small cavity height comparing to a wavelength, for the filament magnetic current, the volume integral reduces to a line integral. The argument here is similar to that of derivation of vector potential for the circular loop current:

$$\bar{F}_r = \frac{\epsilon_0}{4\pi} 2V \sin \theta \int_0^\pi M(\varphi') \sin(\varphi - \varphi') \frac{e^{-jk_0 R'}}{R'} d\varphi' \quad (3.10)$$

$$\bar{F}_\theta = \frac{\epsilon_0}{4\pi} 2V \cos \theta \int_0^\pi M(\varphi') \sin(\varphi - \varphi') \frac{e^{-jk_0 R'}}{R'} d\varphi' \quad (3.11)$$

$$\bar{F}_\varphi = \frac{\epsilon_0}{4\pi} 2V \int_0^\pi M(\varphi') \cos(\varphi - \varphi') \frac{e^{-jk_0 R'}}{R'} d\varphi' \quad (3.12)$$

where \hat{M} is an equivalent magnetic current flowing around the walls of the cavity.

These electric vector potentials produce the following far fields in spherical coordinates (Appendix 9.5):

$$E_\theta = \frac{-jk_0\epsilon_0}{4\pi} \frac{e^{-jk_0r}}{r} ah E_n J_n(\chi_{nm}) \times \int_0^\pi \sin n\varphi' \cos(\varphi' - \varphi) e^{jk_0 \sin \theta \cos(\varphi' - \varphi)} d\varphi' \quad (3.13)$$

$$E_\varphi = \frac{-jk_0\epsilon_0}{4\pi} \frac{e^{-jk_0r}}{r} ah E_n J_n(\chi_{nm}) \cos \theta \times \int_0^\pi \sin n\varphi' \sin(\varphi' - \varphi) e^{jk_0 \sin \theta \cos(\varphi' - \varphi)} d\varphi' \quad (3.14)$$

where $J_1(\chi_{11})$ - is a resonant condition for the dominant TM_{11} mode, ϵ_0 - the substrate permittivity, h - the substrate thickness.

There is no analytical solution for these integrals available in the literature; however, these expressions can be evaluated numerically.

In order to find out the far field patterns of the semicircular PIFA, the latter expressions were evaluated numerically in Matlab. The patterns are given in Figure 3.6- Figure 3.8.

It must be noted as well that the finite ground plane effects are not included in this model, which can be accounted for later by adding the diffraction factors to the above expressions.

It is also of interest to compare the results of this model to those of different numerical techniques, such as Method of Moments or FDTD. In particular, the far field

results of commercially available solver CST Microwave are presented in the Figure 3.6-Figure 3.8 along with the cavity model results. The semicircular PIFA was prototyped in CST of brass plates of thickness $t=1.7\text{mm}$. The inner height of the cavity was $h=1\text{mm}$. The ground-plane was infinite in extent.

As can be seen from these patterns, the general shape far field produced by the semicircular PIFA is very similar to that of the corresponding rectangular PIFA.

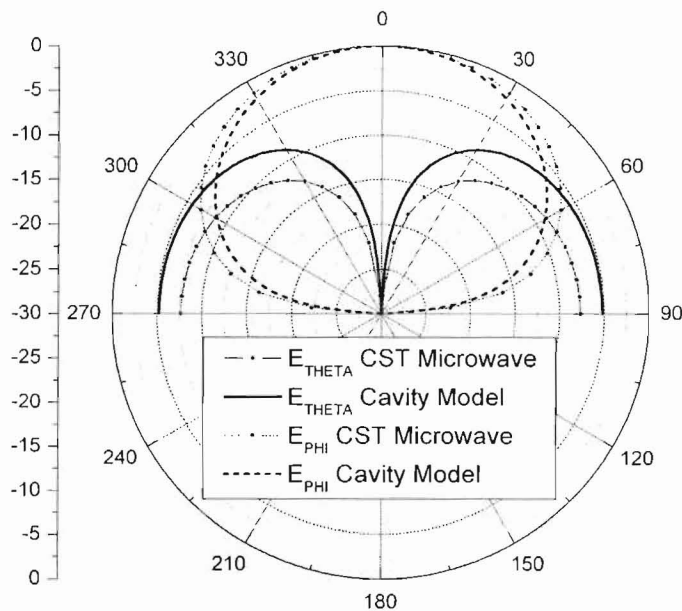


Figure 3.6 XZ plane (H plane) far field pattern for an example of the semicircular PIFA ($ka = 1.84$).

In the XZ plane (H -plane) the semicircular magnetic current of the PIFA's demonstrates usual doughnut shape radiation pattern behavior of magnetic dipole for the E_φ -field component. However, the E_θ -field contribution of the equivalent magnetic current gives a high level of the E_θ -field radiation with a null in the broadside direction. As can be readily seen from the above, the effect of three slot radiation of rectangular

PIFA far field pattern is very similar to the effect produced by the semicircular current in the H -plane.

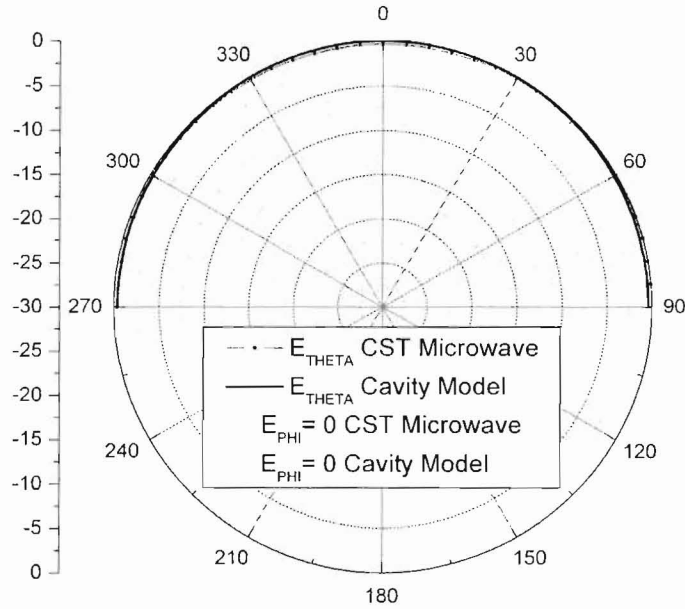


Figure 3.7 YZ plane (E plane) far field pattern for an example of the semicircular PIFA ($ka = 1.84$).

In the YZ plane (E -plane), the semicircular aperture produces almost an omnidirectional E_θ -field radiation.

A good agreement (less than ± 2.5 dB error) of the present theory with numerical results provided by CST FDTD solver is also evident.

As a result, the theoretical model for PIFA cavity just presented can be regarded as an accurate tool for predicting PIFA far field pattern behavior and can be successfully used in the analysis of this type of radiation structure.

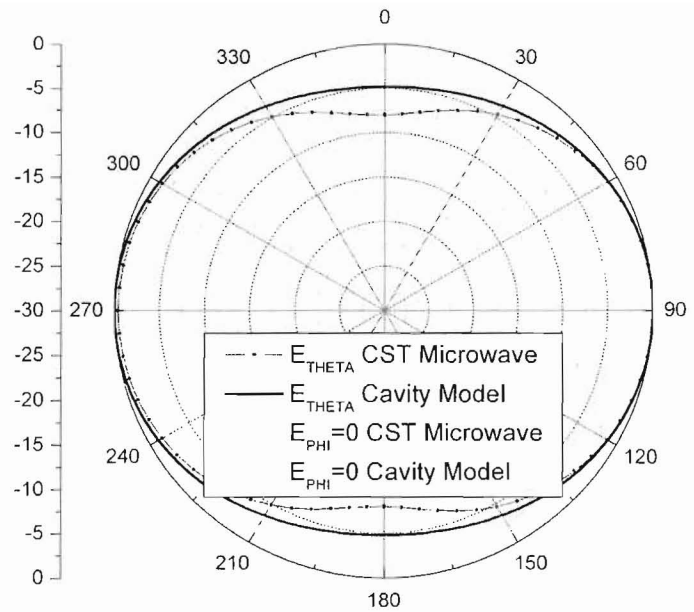


Figure 3.8 XY plane (Ground plane) far field pattern for an example of the semicircular PIFA ($ka = 1.84$).

4 PIFA Q-FACTOR, BANDWIDTH, INPUT IMPEDANCE AND POLARIZATION

4.1 Introduction

The overall goal of design of an antenna is to achieve certain performance characteristics at a certain operating frequency. Most important characteristics in a design of any antenna include radiation pattern, bandwidth, radiation efficiency, and impedance. Having found the radiation pattern of PIFA, it is possible now to determine the rest of the characteristics.

4.2 PIFA Q-factor

Antenna quality factor (Q-factor), is a fundamental parameter for determining the impedance bandwidth of the PIFA. For any resonating structure it is generally defined as [33]:

$$Q = 2\pi \frac{\text{energy stored in the system}}{\text{energy dissipated per cycle}} \quad (4.1)$$

or alternatively

$$Q = \frac{\omega(\text{time averaged energy stored in the system})}{\text{energy dissipated per time unit (sec.)}} \quad (4.2)$$

Considering a PIFA antenna as a radiating microstrip resonator, we can calculate its Q-factor. The averaged energy stored by the antenna resonating structure may be both electric energy and magnetic energy. These can be expressed as integrals over the antenna volume e.g. [1]:

$$W_e = \frac{1}{4} \int_V \epsilon |E|^2 dv \quad (4.3)$$

$$W_m = \frac{1}{4} \int_V \mu |H|^2 dv \quad (4.4)$$

where E and H are the electric and magnetic field peak values respectively.

4.2.1 PIFA losses, antenna efficiency

In general, the value of Q of PIFA resonator is decreased due to radiation losses (useful loss), dielectric losses and conductor losses (both are negative losses) e.g. [21]:

$$\frac{1}{Q} = \frac{1}{Q_r} + \frac{1}{Q_d} + \frac{1}{Q_c} \quad (4.5)$$

If the losses in the PIFA are defined respectively by P_r , P_d and P_c , the Q-factor expression (4.2) can be rewritten as:

$$Q = \frac{\omega(W_e + W_m)}{P_r + P_d + P_c} \quad (4.6)$$

By the operating principle, the PIFA is resonant type of antenna; therefore, its Q-factor is only of interest when there is resonance. In other words, at the resonance, all the PIFA losses, which are generally speaking complex, are considered to be pure active, having their reactive component equal to zero. In addition, at the resonance, the PIFA stored energies are the same, yielding:

$$Q = 2\pi f \frac{W_T}{P_r + P_d + P_c} \quad (4.7)$$

where $W_T = 2W_e = 2W_m$

While the radiation losses P_r are calculated from the far-zone electromagnetic fields, or more precisely from the integration of Poynting vector, the dielectric P_d and conductor P_c losses are calculated from the electromagnetic fields inside the PIFA cavity. The expressions are:

$$P_r = \frac{1}{2} \operatorname{Re} \left(\int_V (\mathbf{E} \times \mathbf{H}^*) \cdot \mathbf{n} dV \right) = \frac{1}{2Z_0} \int_0^{2\pi} \int_0^{\pi/2} (|E_\theta|^2 + |E_\phi|^2) r^2 \sin \theta d\theta d\phi \quad (4.8)$$

where Z_0 is a free space impedance, and E_θ , E_ϕ are the far-zone electric field components.

$$P_d = \pi f \epsilon \tan \delta \iiint_V |E_z|^2 dV \quad (4.9)$$

where f is a resonant frequency, ϵ - permittivity of the substrate, $\tan \delta$ - substrate dielectric loss tangent, E_z - electric field inside the cavity.

$$P_c = R_s \iint_S |\bar{H}|^2 ds \quad (4.10)$$

where R_s is the surface resistivity of the patch conductors, \bar{H} - the cavity magnetic field.

The radiation or antenna efficiency is the ratio of radiated power to input power e.g. [19]:

$$\eta (\%) = \frac{P_r}{P_r + P_d + P_c} \times 100\% \quad (4.11)$$

This formula can be equivalently represented in terms of corresponding network resistances [1], namely R_r , R_d and R_c . The choice of representation of the efficiency formula is dictated by the situation. The efficiency gives explicit information regarding

an antenna's positive utilization of EM energy. Usually, the radiation efficiency of microstrip antennas and PIFA in particular varies in broad limits between 50-99%.

4.2.2 PIFA radiation Q-factor

Radiation Q factor, as a fundamental measure of an antenna's positive utilization of EM energy is one of the most important design parameters. It is a ratio of the whole amount of EM energy stored in an antenna to energy radiated per cycle e.g. [4]:

$$Q_r = 2\pi f \frac{W_T}{P_{rad}} \quad (4.12)$$

The total energy of the PIFA at the resonance can be found conventionally from (4.3) by integrating [34] the electric field inside the cavity volume in (2.11):

$$W_T = 2W_e = 2 \frac{1}{4} \iiint_V \epsilon |E|^2 dv = \frac{\epsilon}{2} \iiint_V | -jE_0 \sin k_y y' |^2 dv = \frac{\epsilon L Wh E_0^2}{4} \quad (4.13)$$

where ϵ, L, W, h are the parameters of the PIFA cavity and the integral expression was solved using the definite integral from [ibid.].

The integral of the power flux (Poynting vector) in (4.8) may be easiest of all solved numerically.

4.2.3 PIFA dielectric Q-factor

PIFA dielectric Q factor is a measure of the antenna's negative utilization of EM energy due to polarization currents in the dielectric. It is a ratio of the whole amount of EM energy stored in the antenna to energy dissipated in the dielectric per cycle:

$$Q_d = 2\pi f \frac{W_T}{P_d} \quad (4.14)$$

Plugging (4.9) into (4.14) reveals a very simple relation similar to [35]:

$$Q_d = \frac{1}{\tan \delta} \quad (4.15)$$

The simplicity of this result is due to the fact that the integral in (4.13) for W_e cancels out with the identical integral in (4.9) for P_d . Therefore, this result can be applied to the Q_d for an arbitrary resonant mode of the PIFA.

4.2.4 PIFA conductor Q-factor

PIFA dielectric Q factor is a measure of the antenna's negative utilization of EM energy due to leaking surface conductor currents on the metal plates of the PIFA cavity. It is a ratio of the whole amount of EM energy stored in the antenna to energy dissipated in the conductors per cycle [4]:

$$Q_c = 2\pi f \frac{W_T}{P_c} \quad (4.16)$$

Using (4.10) and performing the integration across all the metallic walls of the cavity as in [34] with respect to magnetic field structure inside the cavity, finally yields [21]:

$$Q_c = \frac{h}{\delta_S} = h\sqrt{\pi f \mu_0 \sigma} \quad (4.17)$$

where $\mu_0 = 4\pi \times 10^{-7} H/m$ - permeability of free space, $\sigma, S/m (20^0 C)$ - conductivity of the cavity plates metal.

Having found all the contributing Q-factors for PIFA, it is possible to calculate the total Q-factor of the antenna. As can be seen from the above expressions, the Q-factor

is quite complex performance parameter and it depends on many variables and characteristics of the antenna. It is also interesting to know the PIFA Q-factor dependence on the substrate dielectric permittivity with the antenna cavity height as a parameter.

4.3 PIFA Q-factor limit and bandwidth

The importance of the Q-factor for a resonant antenna can be seen from the following relation [36]:

$$Q = \left(\frac{1}{k^3 a^3} + \frac{1}{ka} \right). \quad (4.18)$$

This fundamental relation provides the minimum Q that can be achieved for an electrically small antenna in relation to the smallest spherical volume with radius a that can enclose the antenna (plus its image). In other words, this formulation serves as a lower bound on the Q that can be possibly attained by any feasible antenna.

An electrically small antenna is defined such that its spherical volume is smaller than a radiansphere, or:

$$ka < 1. \quad (4.19)$$

It is characterized by a radiation resistance that is much less than its reactance and by a far-field pattern that is independent of the antenna size [28].

It was also demonstrated in [37] that as the size of an electrically small antenna decreases, its radiation resistance (and reactance) decreases relative to the ohmic losses in the structure. This makes it difficult to transfer power from the generator to the antenna and vice versa as frequency changes. An antenna with those characteristics is considered

to have a high Q. In other words, higher Q means that the input impedance is more sensitive to small changes in frequency.

An electrically small antenna behaves like a simple infinitesimal electric or magnetic dipole. Moreover, [36] showed that a dipole-type radiated field implied the smallest possible Q (4.18). The electric dipole has mostly electric energy which is stored, while for the magnetic dipole the stored energy is mainly in magnetic fields. However, the results do not change since the electromagnetic fields are dual.

It is also of interest to combine the *TM* and *TE* fields in one system and evaluate the Q since various antenna systems have their energy stored in both electric and magnetic fields. It was also shown in [38] that in this case:

$$Q_{TM+TE} = \left(\frac{1}{2k^3 a^3} + \frac{1}{ka} \right). \quad (4.20)$$

The two abovementioned formulations (4.18) and (4.20) serve as a fundamental benchmark in antenna systems that can be approached, but not exceeded. Both these equations are plotted in Figure 4.1 along with the calculated in this work Q for the PIFA and several other types of antennas (see also [1]). A practical antenna will have a Q greater than that of (4.18) or (4.20). The increasing Q with decreasing size of the antenna implies a fundamental limitation on the usable bandwidth of an electrically small antenna.

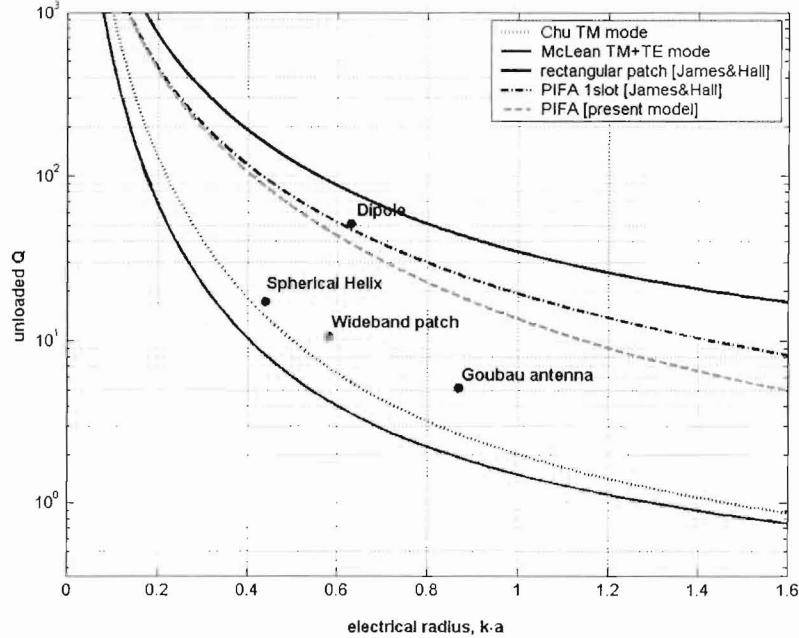


Figure 4.1 Minimum unloaded Q of electrically small antennas according to a dipole mode and the two modes in equal excitation as a function of the enclosing radius.

The Q -factor of the four antennas provided on the plot for a comparison, were calculated by different authors (see [1] for more). For a matched antenna, the unloaded Q can be found approximately from the measured loaded Q (antenna itself plus matching network) as follows:

$$Q_U = 2Q_L \quad (\text{matched}) . \quad (4.21)$$

Also, the theoretical curves are plotted in the assumption of 100% antenna efficiency, while the real measured antenna devices never achieve the perfect efficiency of operation. In this case, the theoretical limits curves can be multiplied by the efficiency factor, as it was done in [28], bringing the curves lower and to the left for a fair comparison.

Nevertheless, the theoretically predicted values of the PIFA Q-factor are very important since they provide information on PIFA resonant characteristics. It can be seen from the plots that generally, the PIFA possesses the lower Q-factor than the corresponding square patch antenna. The influence of the radiating side-slots is evident from the comparison of the one-slot and the three-slot cavity models. The results of a simple single slot cavity model are found to be close to those obtained for a lossless thin dipole, which is expected since the single end-slot magnetic current is the dual of the dipole.

The bandwidth of an antenna usually defined as a specific frequency range, in which the specific performance characteristics of the antenna conform to a certain standard. The PIFA as a member of microstrip antenna class is a strongly resonant device. Conventionally, it is the PIFA impedance, not the far field pattern, serves as a limit on its bandwidth. When the microstrip antenna is matched to its feeding structure, the mismatch loss off the antenna's resonance is usually described by the *Voltage Standing Wave Ratio – VSWR*. The maximum tolerated value of the VSWR then defines the bandwidth of the antenna (see Chapter 6):

$$BW = \frac{100(VSWR - 1)}{Q_T \sqrt{VSWR}} \% \quad (4.22)$$

This formula defines the usable bandwidth (in percents of the resonant frequency) as a relation to the total Q-factor of the antenna, for the $VSWR \geq 1$, but less than the certain value. For instance, for $VSWR=2$, which is a common standard, the above equation will look like:

$$BW = \frac{100}{Q_T \sqrt{2}} \quad \% . \quad (4.23)$$

This is a most widely accepted definition of bandwidth of an antenna; however, some authors could define the bandwidth of an antenna as a simple reciprocal of its total Q-factor $1/Q_T$.

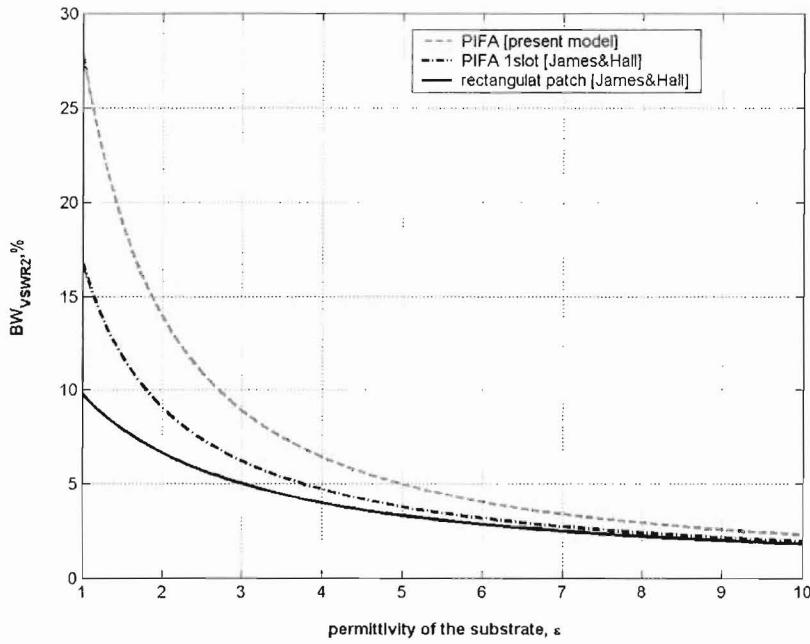


Figure 4.2 The PIFA's VSWR=2 bandwidth versus the substrate permittivity according to different models results. Cavity height $h=7.5\text{mm}$.

Using the Q the PIFA's VSWR=2 bandwidth is plotted against different PIFA's substrate permittivity values in Figure 4.2. A substrate with higher permittivity reduces the electrical size of the antenna, or in other words, reduces its resonant frequency. The figure shows the associated bandwidth reduction, which is a fundamental trade-off in compact antenna design. The PIFA is assumed to be matched in order to interpret the VSWR measure. But in practice an impedance match to a 50 ohm coax feed located on

the center line of the PIFA would be unlikely for the range of the substrate permittivities shown, so strictly, a lossless matching network is assumed for this figure. Finally, it must be noted that the inscribing sphere is not an ideal measure of volume for all patch antennas, and particularly not for thin panels for wall or ceiling mounting. Nevertheless, it still serves as a useful compactness measure.

Also, it has been found experimentally (see Section 6 for more), that the present cavity model provides the better agreement with experimental data than the simple single slot PIFA model, which is expected, since the simple model does not account for the PIFA's sidelobes radiation.

4.4 PIFA input impedance

In this section, the PIFA's input impedance as a function of feed position will be studied using cavity model along with numerical and experimental results.

According to the cavity model, input impedance Z_{in} can be estimated by using both the far fields radiation pattern and resonant cavity electromagnetic fields as it was outlined in [21] for a rectangular patch antenna. The input impedance of a microstrip antenna can be found as follows [39]:

$$Z_{in} = \frac{0.5V_0V_0^*}{P_T + j2\omega(W_e - W_m)}, \quad (4.24)$$

where

$$P_T = P_{rad} + P_c + P_d, \quad (4.25)$$

is the total power dissipated by the antenna; P_{rad} – the power radiated by the antenna; P_c – ohmic (conductor) losses in the antenna; and P_d – losses in the dielectric of the cavity.

The W_e and W_m were defined earlier in (4.3) and (4.4) respectively, as well as P_{rad} P_d and P_c were in(4.8)-(4.10) respectively. Also the patch edge voltage is [21]:

$$V_0 = hE_z. \quad (4.26)$$

The input impedance of the PIFA can be calculated numerically from the above expressions using Matlab and corresponding expressions for electromagnetic fields inside the PIFA cavity from (2.11) and (2.17).

It is clear from the above expressions that the PIFA's input impedance Z_{in} will be a function of the feed position along the center length of the antenna, because the E_z field is a sinusoidal function. This was noted by [35, 40] for rectangular patches and it is assumed to be true for the case of the PIFA [21]. However, as far as the author is aware, there is no theory or data present to predict the PIFA input impedance off the central axis of the PIFA.

Here, and later in the section devoted to the transmission line model, an effort will be made to fill that gap. In this section, the data predicted by the cavity model, will be compared with experimental as well as numerical results provided by Method of Moments and FDTD electromagnetic solvers.

A set of the rectangular PIFA's input impedance curves versus a normalized feed position is shown in Figure 4.3 (center feed locus) and Figure 4.4 (side-slot locus). The full range of graphs represents feed positions from the short circuit plate ($L = 0$) to the open edge-slot of the PIFA ($L = \lambda/4$).

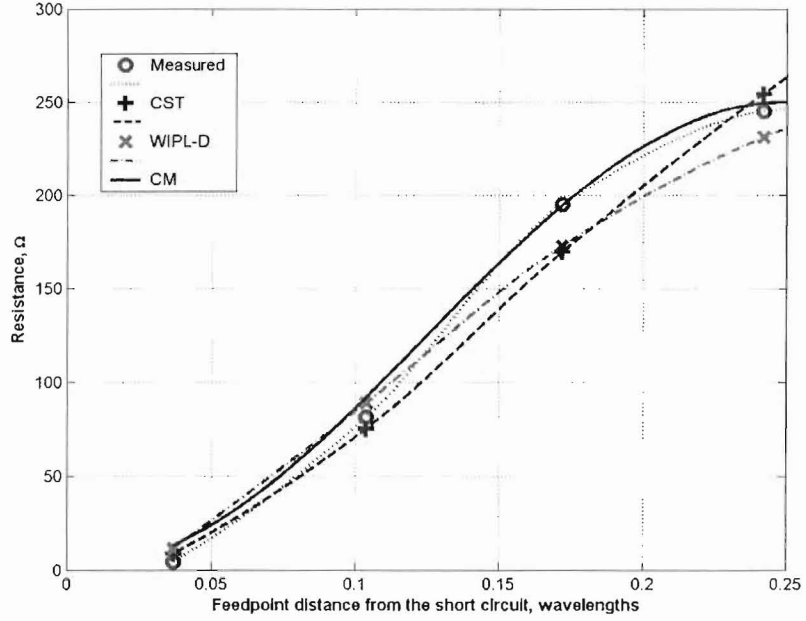


Figure 4.3 Rectangular PIFA input impedance fed at an arbitrary point along its center length: Cavity model, experimental results, CST FDTD solver, and WIPL-D Method of Moments solver.

Throughout this investigation, results for the PIFA input impedance were taken at the frequency *at which the maximum input resistance occurs*. Also, for the purposes of this study, a rectangular PIFA prototype was manufactured and its input impedance was extensively measured (see more on the prototype parameters and the measurement technique etc in Section 6). This prototype was subsequently modeled in CST Microwave commercial electromagnetic solver using the FDTD method, and WIPL-D EM modeling software using its Method of Moments engine. No optimization was made on either prototypes, regardless their resonant frequencies, bandwidth, gain etc. In both above mentioned EM solvers, basic feed ports were used.

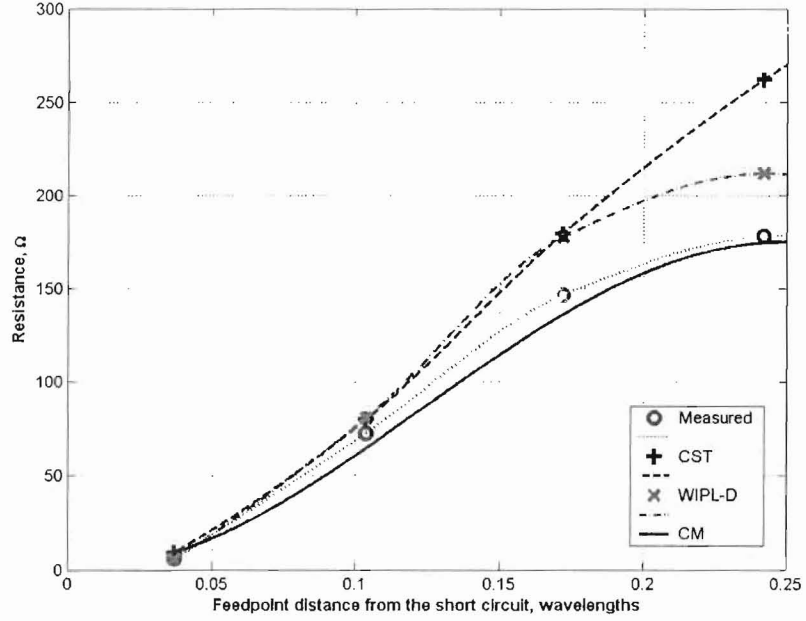


Figure 4.4 Rectangular PIFA input impedance fed at an arbitrary point along its sideslot length: Cavity model, experimental results, CST FDTD solver, and WIPL-D Method of Moments solver.

As can be seen from the plot (Figure 4.3), the cavity model provides good prediction about the rectangular PIFA input resistance behavior along its center. The shape of the measured input impedance curve is evidently close to that of cosine-squared type function provided by the theoretical cavity model. Both EM solvers provide fairly good results in terms of prediction of the rectangular PIFA input impedance along its center. The experimental and simulated data points were interpolated in Matlab using cubic spline interpolation.

Figure 4.4 shows that the agreement of the numerical data with the measured data degrades at the side-slots. Here, a modeled non-uniform illumination from a cosine-on-a-peDESTAL model can provide good agreement with the measurements. Incidentally, the

theoretical prediction of the PIFA's input impedance using the Cavity Model multiplied by a pedestal factor of $C=0.7$ provides very good agreement with the measured data.

4.5 PIFA polarization

The polarization of an arbitrary antenna is sensed from the plane wave transmitted by that antenna. The PIFA is inheritably a linearly polarized antenna. However, it is possible to find certain angular directions for which, the so called cross polar and co polar components of an electromagnetic wave, radiated by the PIFA have almost identical amplitudes, meaning that for these directions the circularly polarized (CP) radiation from the PIFA is achievable.

The sense of polarization of CP has been a source of ongoing confusion between the antenna and the propagation communities, so the definitions used here are briefly reviewed in order to avoid ambiguity. According to the IEEE standard [41], the sense of CP is determined by viewing the polarization plane, which contains the transverse electric field vector, with the wave direction moving away from the observer. At a fixed point in space, if the tip of the vector rotates clockwise as a function of time, the wave is right-hand (RH) polarized. For counter clockwise rotation, it is left-hand (LH) polarized. If the time dependence is taken as either $e^{i\omega t}$ or $e^{-i\omega t}$, then the RHCP and LHCP are reversed vice versa.

Using the complex vector representation [42], and assuming RHCP is the co-polarization, the complex unit vectors associated with the two orthogonal CP polarization states, i.e., co-polarization (RHCP) and cross-polarization (LHCP), are:

$$\hat{e}_{co} = \frac{1}{\sqrt{2}} \left((\sin \varphi + j \cos \varphi) \hat{\theta} + (\cos \varphi - j \sin \varphi) \hat{\phi} \right) = \frac{1}{\sqrt{2}} e^{-j\varphi} (\hat{\theta} - j \hat{\phi}), \quad (4.27)$$

$$\hat{e}_{cr} = \frac{1}{\sqrt{2}} \left((\sin \varphi - j \cos \varphi) \hat{\theta} + (\cos \varphi + j \sin \varphi) \hat{\phi} \right) = \frac{1}{\sqrt{2}} e^{j\varphi} (\hat{\theta} + j \hat{\phi}). \quad (4.28)$$

If LHCP is the co-polarization, then these vectors are interchanged.

The circular polarization ratio (CPR) is variously used in the literature as either the ratio of powers or amplitudes. The CPR, ρ_c , is defined as the amplitude of the RHCP over that of the LHCP, following from [43] to the IEEE standard [41].

The CPR, defined in dB scale, is related to the amplitude CPR, ρ_c , using the following formula:

$$R = \begin{cases} \rho_c & \text{if RHCP is the co-polarization} \\ 1/\rho_c & \text{if LHCP is the co-polarization} \end{cases} \quad (4.29)$$

Finally, ρ_c and R are related to the traditional metric of circular polarization purity, the *axial ratio*, A , using [41] and [42], respectively:

$$A = \frac{\rho_c + 1}{\rho_c - 1}, \quad \text{where } |A| = \frac{1+R}{1-R} \quad (4.30)$$

Therefore, better polarization purity translates into a low value of the CPR or an axial ratio magnitude which is close to 1.

The left hand (LHCP) and the right hand (RHCP) circular polarization patterns are calculated from the PIFA far field components according to the following formulas:

$$E_{LHCP} = \frac{1}{\sqrt{2}} \sqrt{\left(\operatorname{Re}(E_\theta) + \operatorname{Im}(E_\varphi) \right)^2 + \left(\operatorname{Im}(E_\theta) - \operatorname{Re}(E_\varphi) \right)^2} \quad (4.31)$$

$$E_{RHCP} = \frac{1}{\sqrt{2}} \sqrt{\left(\text{Im}(E_\theta) + \text{Re}(E_\varphi)\right)^2 + \left(\text{Re}(E_\theta) - \text{Im}(E_\varphi)\right)^2} \quad (4.32)$$

The axial ratio was found from the abovementioned components as follows:

$$AR = \sqrt{\frac{\left|E_\theta\right|^2 + \left|E_\varphi\right|^2 - \left|E_\theta + E_\varphi\right|^2}{\left|E_\theta\right|^2 + \left|E_\varphi\right|^2 + \left|E_\theta + E_\varphi\right|^2}} \quad (4.33)$$

As an example, the three-slot cavity model CP patterns, normalized to their respective maximum gains, are presented in the Figure 4.5 along with numerical and physical measurements results.

As can be seen from the figures, the cavity model patterns differ from the experimental results only for lower elevation angles where the finite groundplane starts to influence the pattern. Very good agreement between the experimental results and those simulated by CST is also evident (generally patterns from numerical analysis are accurate owing to the effect of error cancellation in the finite elements of current).

There are directions of very pure CP at $\pm 45^\circ$ off broadside, where the two opposite hands in the different, symmetric directions. This CP behavior is an interesting consequence of the side-slots and does not occur for the square patch.

In the YZ plane the LHCP and RHCP patterns of the PIFA are identical (see Figure 4.5). This is expected because in this plane of symmetry, the polarization has to be linear, so these patterns also represent the LP pattern (with a scaling factor of -3dB). The skewness illustrates the inherent asymmetry of the PIFA.

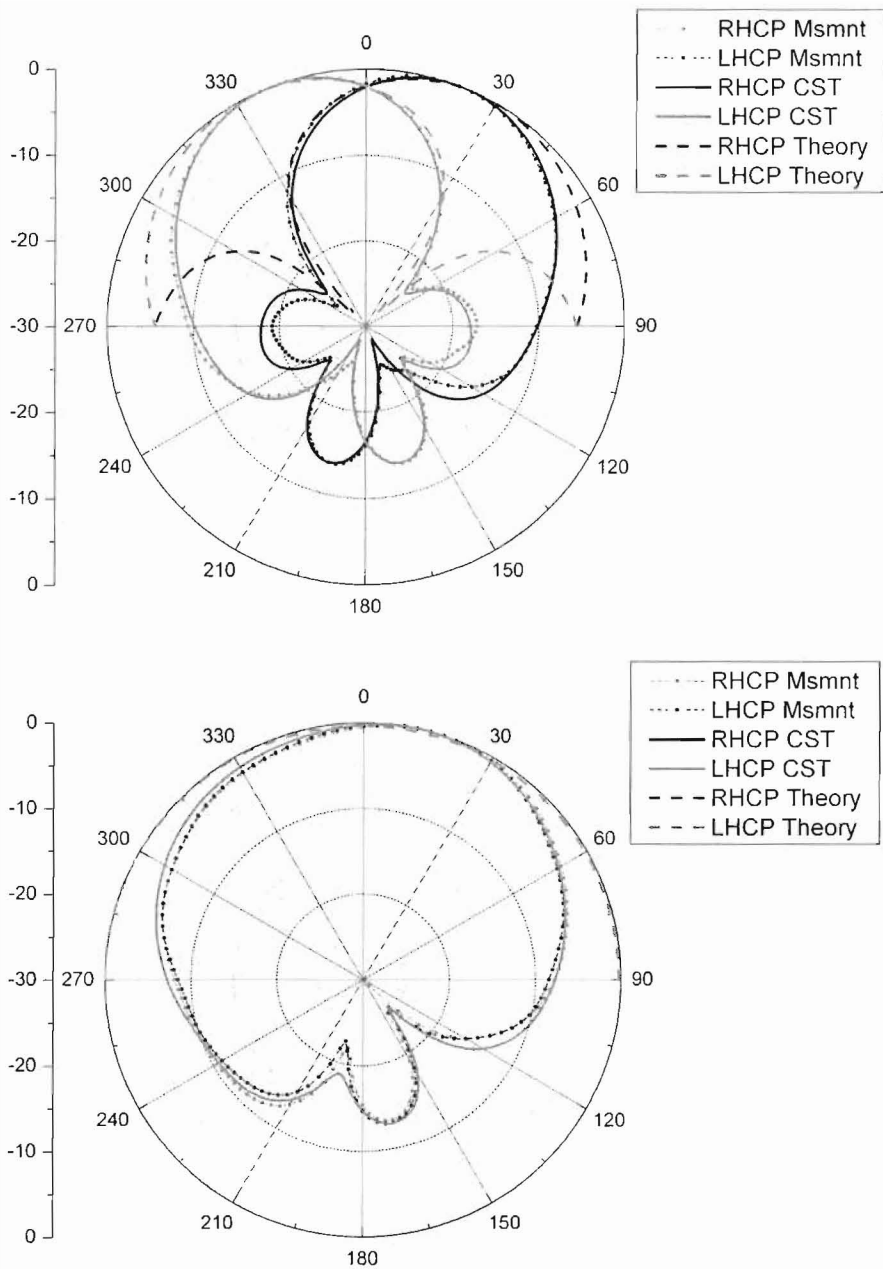


*Figure 4.5 XZ (top), YZ plane (bottom) CP patterns for an example of the rectangular PIFA ($W = \lambda / 2$, $L = \lambda / 4$).
Experiment and numerical results are of the PIFA with:
substrate thickness – 1mm, metal plate thickness $t = 1.7$
mm. $W = 146$ mm, $L = 78$ mm. The groundplane size:
 400×300 mm ($W \times L$).*

The 3D axial ratio (AR) patterns of the PIFA on both infinite and finite groundplanes are shown in Figure 4.6 and Figure 4.7 respectively. The plots give a feel for the CP behavior for the infinite and finite groundplane cases. The shape and size of the groundplane plays a role in the polarization detail, as is known for circularly polarized circular patches [44]. The CP behavior raises the possibility of using the PIFA for CP arrays with fixed directions.

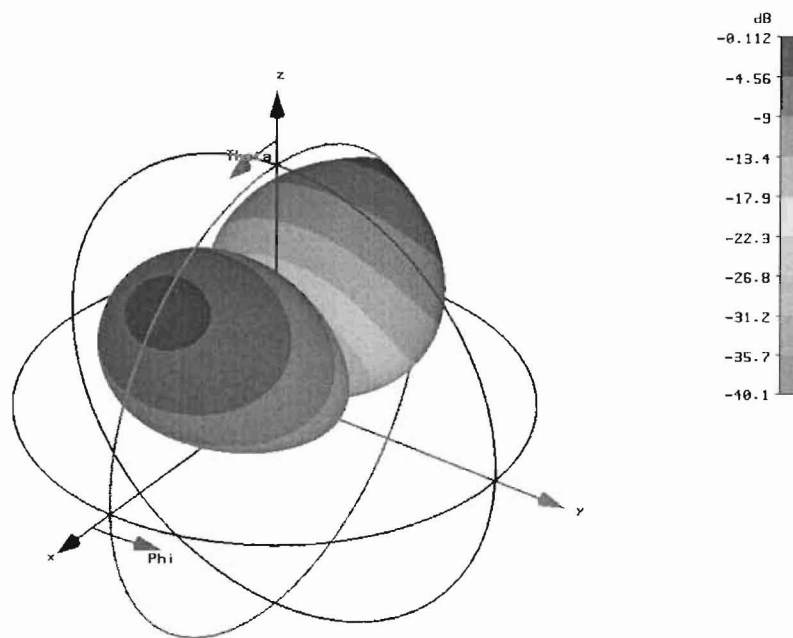


Figure 4.6 Rectangular PIFA on infinite groundplane CP axial ratio for a full spatial sphere of radiation in 3D. CST FDTD results.

Figure 4.8 also shows that, for the single mode RPPIFA and SCPIFA on infinite groundplanes, the purest CP is achieved at two angular sectors off broadside direction. It can also be noted from the plots that both antennas possess almost identical polarization

properties, which is expected, since their predicted far fields' behavior is also very similar.

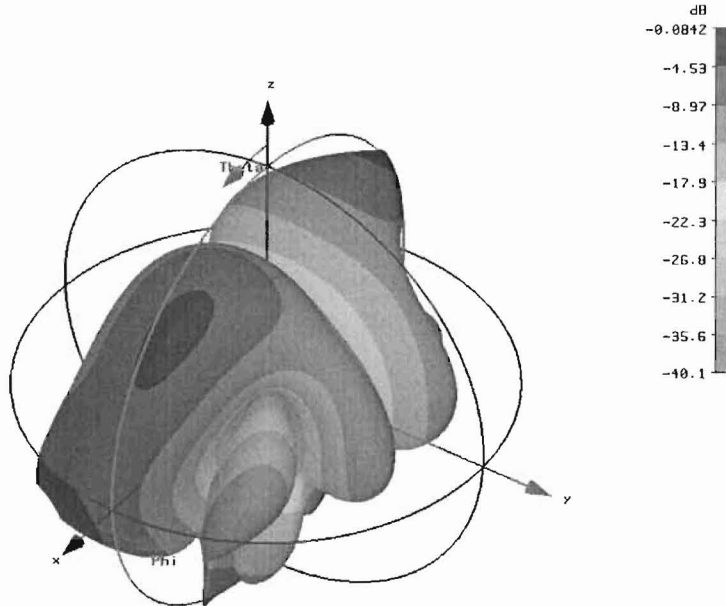


Figure 4.7 Rectangular PIFA on finite groundplane CP axial ratio for a full spatial sphere of radiation in 3D. CST FDTD results.

Figure 4.9 shows that, for the single mode RPIFA and SCPIFA on finite groundplanes, the purest CP is also achieved off the broadside direction. However, it is evident from the pictures, that the CP purity is more distributed across the spherical volume of radiation, which is caused by the diffraction effects of a finite groundplane.

It can also be noted from the plots that both antennas possess almost identical polarization properties, except for the different groundplanes' shape, which causes minor differences in the CPR axial ratio patterns.

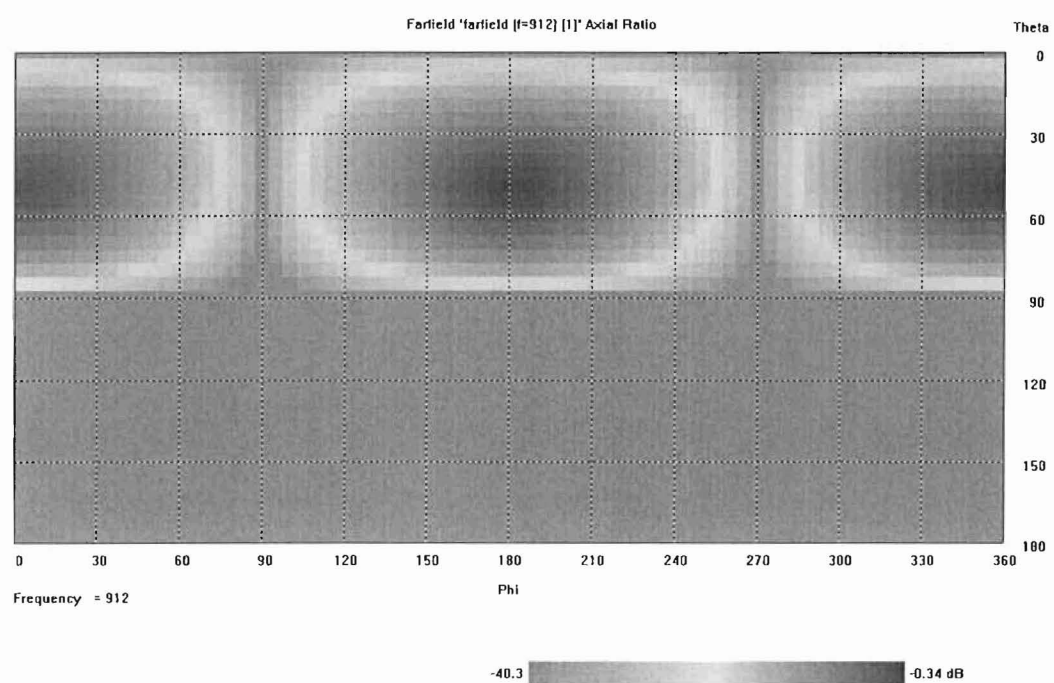
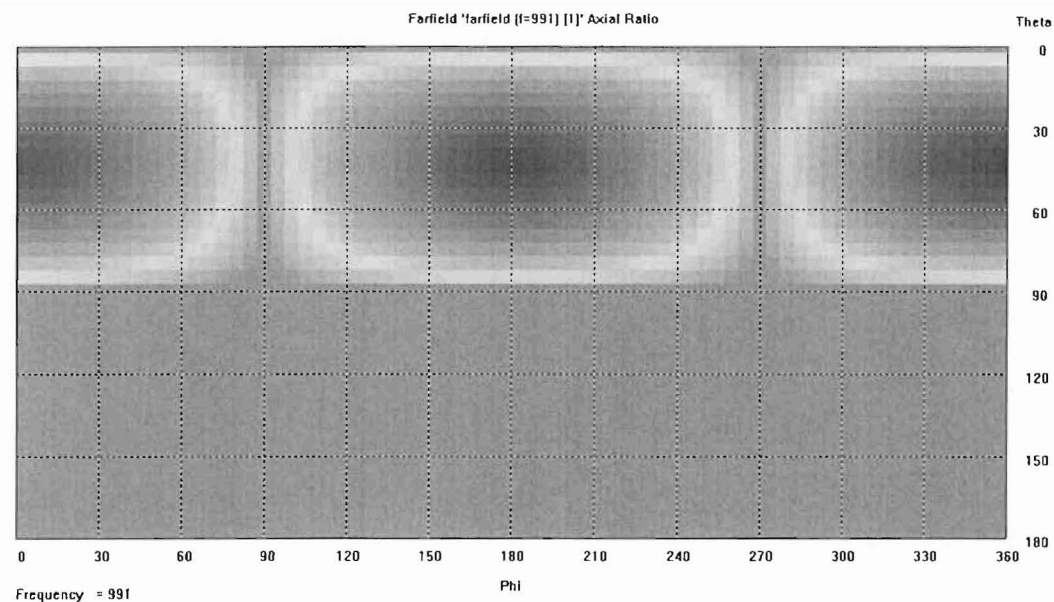


Figure 4.8 Rectangular PIFA (top) and semicircular PIFA (bottom) on infinite groundplanes axial ratios for a full spatial sphere of radiation in 2D. CST FDTD results.

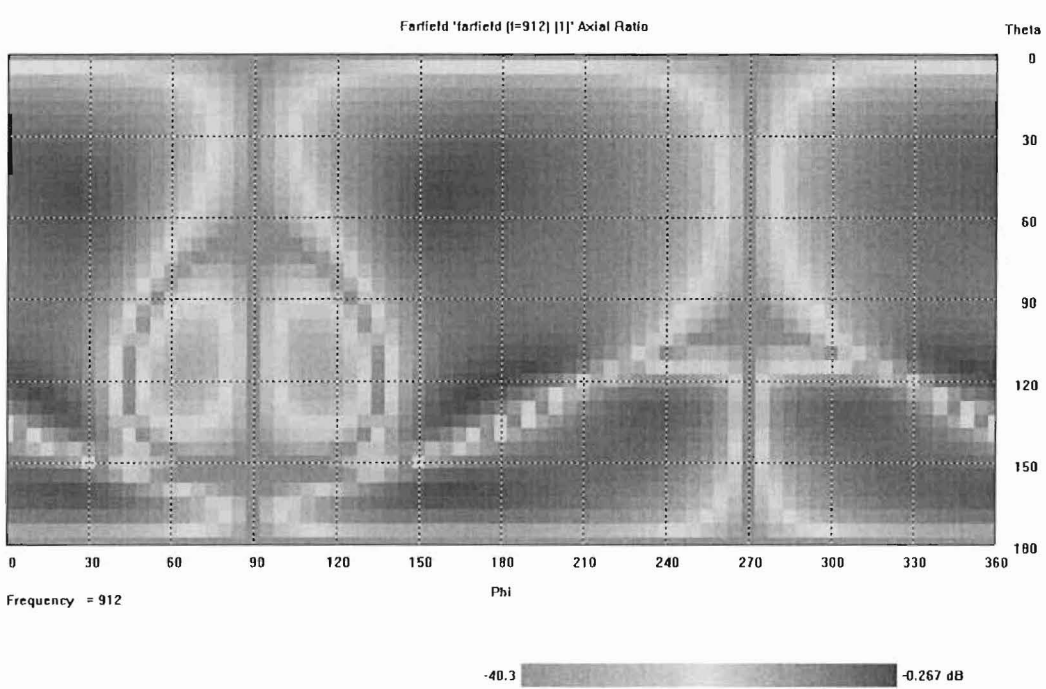
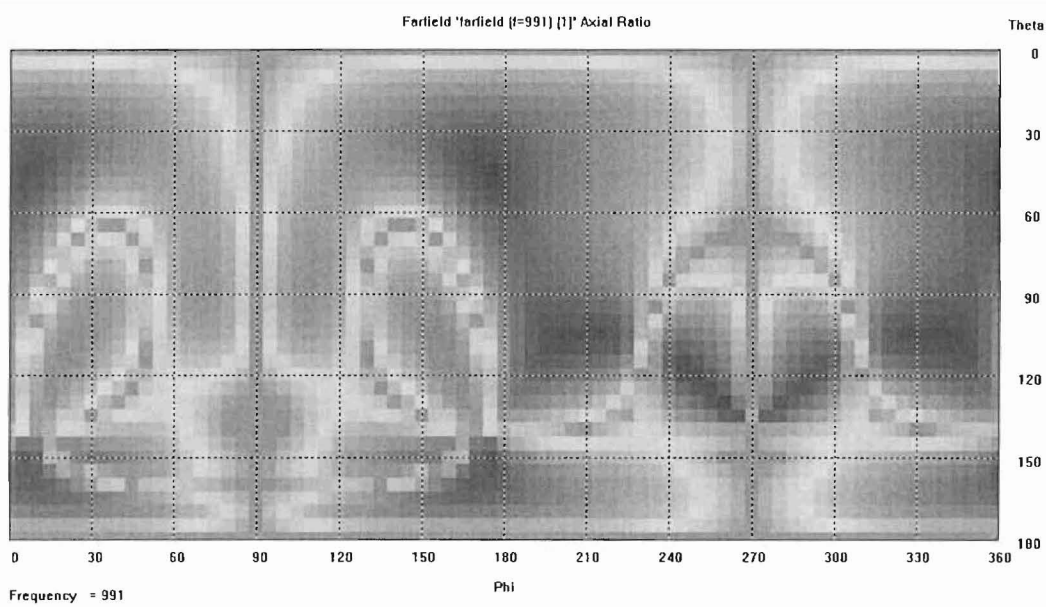


Figure 4.9 Rectangular PIFA (top) and semicircular PIFA (bottom) on finite groundplanes axial ratios for a full spatial sphere of radiation in 2D. CST FDTD results.

Nevertheless, in multi-element antenna arrays, and other practical scenarios with substantial groundplane sizes, the antenna is not required to cover all directions, including those along the groundplane. Instead, the pattern model is only required to cover a limited scan sector around broadside. This is beneficial because as it was shown in the above, a finite groundplane affects the accuracy of the PIFA model at low-elevation angles.

5 TRANSMISSION LINE MODEL

5.1 Introduction

The transmission line model [45, 46] may be thought of as a simple, but at the same time adequate tool for analyzing PIFA performance. It requires less computational power comparing to any other analytical or numerical model, yet it provides satisfactory results for most engineering applications. The model is useful in practical design of microstrip antennas, arrays, matching and feeding networks.

As its name suggests, the main role of the transmission line model is to use transmission line parameters of an equivalent circuit of PIFA resonator to estimate the PIFA impedance behavior. The antenna assumed to be comprised of a conducting patch (upper patch) with a short circuit plate (pin), a dielectric substrate and a conducting ground plane. The antenna may be fed either by a coaxial probe or by a microstrip line.

In this analysis, two approaches are described in an attempt to apply the transmission line model to PIFA analysis. The first one is a simple approach or the basic transmission line model, while the second one, is more general approach, based on the three port network model. Furthermore, the data acquired from the transmission line model is compared here to data from the cavity model as well as numerical simulations based on (Method of Moments, FDTD) and measurement results.

5.2 Basic transmission line model

In the transmission line model, the microstrip radiator is treated as a line resonator with no transverse field variations. The fields vary along the length of the radiator, which is usually a quarter wavelength and, as in the cavity model case, it is assumed that the radiation originates mainly from the fringing fields at the open circuited ends of the antenna which is supported by currents on the exterior of the patch and on the ground plane. The fields can be viewed as the fields of rectangular slots in an infinite ground plane. The PIFA equivalent slot arrangement is shown in Figure 5.1:

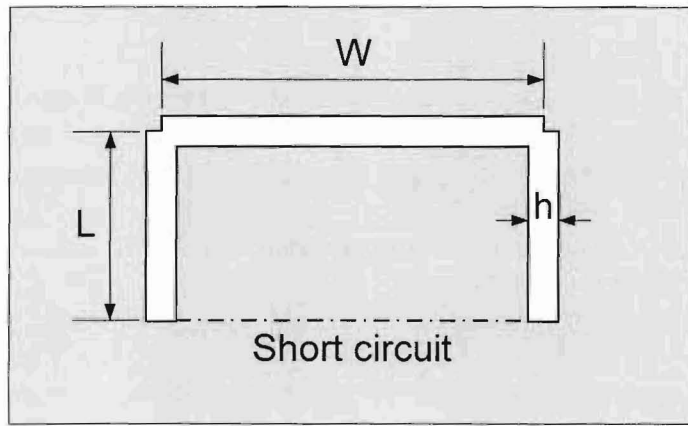


Figure 5.1 PIFA's equivalent three-slot arrangement. In practice, the slot width is constant, i.e., the indented corners are not implemented, they are drawn indented to clarify the slots dimensioning.

The metal structure of the PIFA is characterized by the resonant length L (fundamental mode), the width W , the thickness t , and the conductivity σ . The dielectric part of the antenna is characterized by its length L_d , the width W_d , the thickness h , a relative permittivity ϵ_r , and a loss tangent δ_s . The finite ground plane effects are not considered in the model, thus the ground plane assumed to be infinite.

Since PIFA is essentially a half of a rectangular microstrip antenna with one of its edges shorted, the transmission line model for PIFA can be expanded from the model of rectangular microstrip antenna in [4]. When excited with the coaxial probe at an arbitrary point on the y-axis, the equivalent simple transmission line model for PIFA can be represented as shown in Figure 5.2:

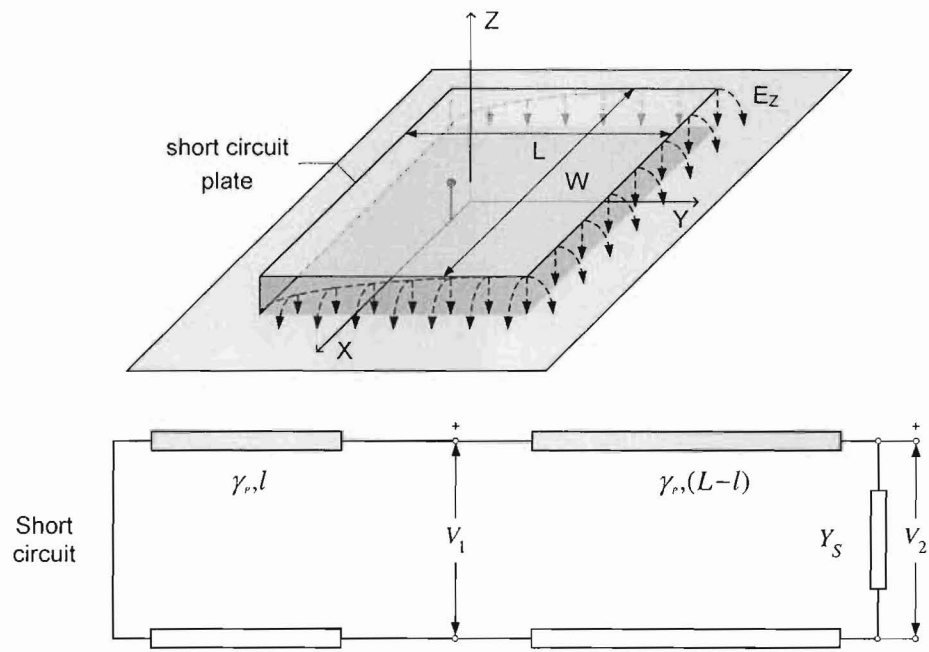


Figure 5.2 Perspective view of PIFA fed at an arbitrary point along y axis and its one-slot transmission line model.

The PIFA radiator is represented by a transmission line with characteristic admittances Y_c (mainly defined by the W/h ratio and the permittivity ϵ_r), physical width W and length L , and a propagation constant γ_p . In addition, the open-ended edge of the PIFA is modeled by parallel admittance Y_s . This is a crucial step for accurate frequency behavior modeling because the open-ended terminations of the PIFA microstrip are not perfect open circuits owing to fringing effects at the slots. Hence, the real part, G_{es} (the

conductance), of the parallel admittance Y_{es} represents the radiation of the slot, while the imaginary part, B_{es} (the susceptance), defines the reactance (energy) accounting for the lengthening effect of the transmission line due to fringing.

The input impedance of the PIFA's transmission line model at the feed point can be calculated by adding the above mentioned parallel admittances of the two transmission lines of appropriate length connected to a load impedance. The input impedance of a transmission line of length d with characteristic impedance Z_C connected to the load Z_L can be found as e.g. [34]:

$$Z_{in} = Z_C \frac{Z_L + jZ_C \tan(\gamma_p d)}{Z_C + jY_L \tan(\gamma_p d)} \quad (5.1)$$

Therefore, from the equivalent network in Figure 5.2, the input admittance of the PIFA radiator can be represented in terms of the corresponding characteristic admittances and propagation constants of the equivalent simple transmission line segments in the following way:

$$Y_{in} = jY_c \cot(\gamma_p l) + Y_c \frac{Y_{es} + jY_c \tan(\gamma_p (L - l))}{Y_c + jY_{es} \tan(\gamma_p (L - l))} \quad (5.2)$$

In this expression, it is assumed that the antenna is fed at an arbitrary point along the y-axis. If the PIFA is fed from its open edge (which is the simplest way to feed the antenna), the tangent terms vanish and the latter expression collapses to:

$$Y_{in} = jY_c \cot(\gamma_p l) + Y_{es} \quad (5.3)$$

where l is the distance from the short circuit to the feed, and $\gamma_p \approx k_0 \sqrt{\epsilon_e}$ - is the propagation constant in the direction of wave spreading.

Also [21],

$$Y_c = \frac{1}{Z_c} \approx \frac{\eta_0}{\sqrt{\epsilon_e}} \frac{h}{W} \quad (5.4)$$

where ϵ_e will be discussed later.

Since the PIFA in the transmission line analysis is represented by its open edge slot and non-radiating short-circuit, its far field may be thought of as the field radiated by magnetic source which produces the same result as for the simple cavity model (see the corresponding section).

5.3 Three slot transmission line model

The basic transmission line model has some inherent disadvantages [22]:

1. Expression for the end slot admittance Y_{es} is not accurate in broad limits for usual patch widths (see further below);
2. The radiation from the sideslots is not taken into account

To eliminate the second shortcoming, an improved three-slot transmission line model was proposed by [1]. The equivalent network representation for this model corresponds to that shown in the Figure 5.3. In this model, Y_{ss} is the admittance of each of the sideslots.

The basic assumption is that the propagation in the cavity along the x- and y-directions can indeed be separated in this way.

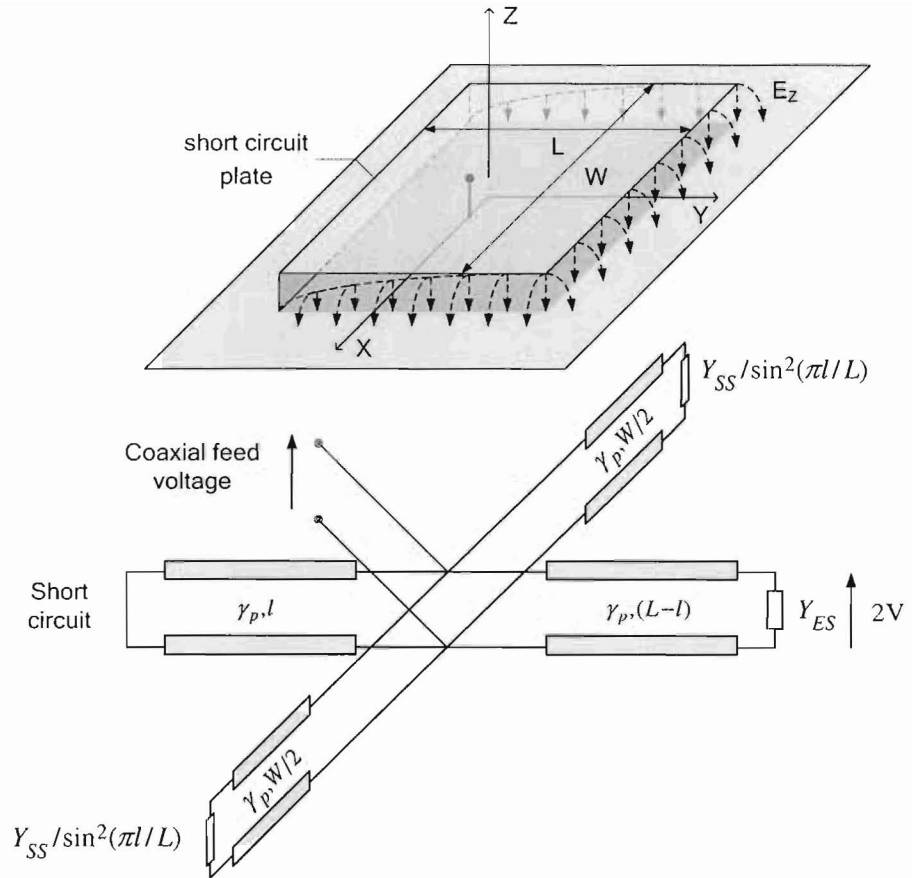


Figure 5.3 Perspective view of PIFA fed at an arbitrary point along x and y axes and its three-slot transmission line model equivalent network.

If the PIFA radiator is fed from only one point, the expression for the input admittance of the PIFA is cf. [1].

$$\begin{aligned}
 Y_{in} = & jY_c \cot(\gamma_p l) + Y_c \frac{Y_{es} + jY_c \tan(\gamma_p (L - l))}{Y_c + jY_{es} \tan(\gamma_p (L - l))} + \\
 & + Y_c \frac{Y_{ss} + jY_c \tan(\gamma_p (w))}{Y_c + jY_{ss} \tan(\gamma_p (w))} + Y_c \frac{Y_{ss} + jY_c \tan(\gamma_p (W - w))}{Y_c + jY_{ss} \tan(\gamma_p (W - w))}
 \end{aligned} \tag{5.5}$$

Again, if fed from the open edge, the latter expression collapses to:

$$Y_{in} = jY_c \cot(\gamma_p l) + Y_{es} + Y_c \frac{Y_{ss} + jY_c \tan(\gamma_p(w))}{Y_c + jY_{ss} \tan(\gamma_p(w))} + \\ + Y_c \frac{Y_{ss} + jY_c \tan(\gamma_p(W-w))}{Y_c + jY_{ss} \tan(\gamma_p(W-w))} \quad (5.6)$$

Any mutual coupling between all the slots has been ignored in this model. This would be an increasing problem for higher permittivities as the side-slots become closer, although it is possible to add simple circuit sources for modeling the mutual coupling. However, caution must be exercised here because this model (without mutual coupling) does not indicate uniform illumination of the end-slot, an assumption used in the classical cavity model. This in turn creates problems for estimating the end-slot admittance, and complicates any source modeling for the mutual coupling. There is a need for new work in this area. Also, latter expressions are asserted to be valid if the PIFA is fed anywhere across its perimeter.

The three slot transmission line model expressions presented here naturally presume the existence of the second transmission line corresponding to the two sideslots arrangement, which is orthogonal to basic one slot transmission line. Therefore, in general, the wave propagation constants corresponding to each transmission line should have different values.

Hence, the task at hand is to scrutinize the parameters of the transmission line model such as slots' admittances and transmission lines' propagation constants.

5.4 Expressions for transmission line parameters

The accuracy of the transmission line model strongly depends on the accuracy of expressions for transmission line parameters, such as Y_{es} , Y_{ss} , etc. There are several ways

to calculate the parameters that will be compared here (see also [4]). In general, the various methods differ in the initial assumptions, which subsequently lead to different analytical approaches.

5.4.1 Endslot conductance

Even with the simplification that the end-slot illumination is uniform, the problem of finding its admittance arises. There appears to be scant reliable admittance data available, and this is important for modeling accurate frequency behavior. Estimates for the admittance of the uniform slot are therefore reviewed here.

5.4.1.1 Equivalent aperture model for a uniform slot

The end-slot conductance can be derived using equivalent aperture concept [22, 35]. The uniform open-end termination is replaced by a uniformly excited rectangular TE slot of finite width and length on the infinite perfectly conducting ground plane.

When the electric field in the endslot aperture is assumed to be uniform:

$$\mathbf{E}_A = \frac{V_s}{h} \hat{\mathbf{i}}_y \text{ for } |y| \leq \frac{h}{2}, |x| \leq \frac{W}{2} \quad (5.7)$$

where V_s is the excitation voltage across the aperture, h is an equivalent aperture height, and W is its equivalent width.

The spatial Fourier transform of the aperture field is then defined as [4]:

$$\mathbf{F}_A = \int_{-\infty}^{\infty} \int_{-\infty}^{\infty} \mathbf{E}_A e^{jk_x x} e^{jk_y y} dx dy \quad (5.8)$$

where k_x, k_y are the components of the complex propagation vector \mathbf{k} , and:

$$|k| = k = \omega\sqrt{\mu\epsilon} \quad (5.9)$$

Use of derivations outlined in (ibid.) yields expressions for G_s and B_s respectively:

$$G_s = \frac{1}{\pi^2 \eta k |V_s|^2} \int_0^k \int_0^{\sqrt{k^2 - k_x^2}} (k^2 - k_x^2) |\mathbf{F}_y|^2 \frac{dk_y dk_x}{\sqrt{k^2 - k_x^2 - k_y^2}} \quad (5.10)$$

$$\begin{aligned} B_s &= \frac{1}{\pi^2 \eta k |V_s|^2} \int_0^k \int_{\sqrt{k^2 - k_x^2}}^{\infty} (k^2 - k_x^2) |\mathbf{F}_y|^2 \frac{dk_y dk_x}{\sqrt{-k^2 + k_x^2 + k_y^2}} \\ &= \frac{1}{\pi^2 \eta k |V_s|^2} \int_k^{\infty} \int_0^{\infty} (k^2 - k_x^2) |\mathbf{F}_y|^2 \frac{dk_y dk_x}{\sqrt{-k^2 + k_x^2 + k_y^2}} \end{aligned} \quad (5.11)$$

where

$$k_z = \begin{cases} \sqrt{k^2 - k_x^2 - k_y^2} & \text{for } k^2 \geq k_x^2 + k_y^2 \\ -j\sqrt{k_x^2 + k_y^2 - k^2} & \text{for } k^2 < k_x^2 + k_y^2 \end{cases} \quad (5.12)$$

Since the PIFA is a resonant structure, and the main focus here is on compact antennas, only the impedance at its resonance of the fundamental mode is of interest. The conductance, G_s , part of the slot admittance is expanded here. Substituting the expression for the aperture field Fourier spatial transform into the equation for conductance of the slot (5.10), and rewriting the double integral in terms of Bessel function of the first kind and order zero after expanding in a Maclaurin series and integrating term by term finally yields (keeping the first two terms) [ibid.]:

$$G_s \approx \frac{1}{\pi\eta} \left\{ \left(kWSi(kW) + \frac{\sin(kW)}{kW} + \cos(kW) - 2 \right) \left(1 - \frac{h^2}{24} \right) \right. \\ \left. + \frac{h^2}{12} \left(\frac{1}{3} + \frac{\cos(kW)}{k^2 W^2} - \frac{\sin(kW)}{k^2 W^2} \right) \right\} \quad (5.13)$$

where the $Si(x) = \int_0^x \frac{\sin(u)}{u} du$ function was solved using the power series expansion:

$$Si(x) = x \sum_{k=0}^{\infty} \frac{(-1)^k}{(2k+1)(3/2)^k k!} \left(\frac{x}{2} \right)^{2k} \quad (5.14)$$

and the number of terms is treated below, indicating that truncating at $k = 4$ is sufficient

5.4.1.2 Uniform voltage source model

Previously (see Section 2), it was noted that the PIFA's endslot can be modeled as an equivalent uniform voltage source. The directivity of the uniform slot is used in obtaining the end slot conductance [19]. Equating the radiated power with the power at the slot terminal:

$$P_{rad} = 1/2 G_{ES} V^2 \quad (5.15)$$

where V is a slot voltage, gives the formula for the uniform slot:

$$G_{ES} = \frac{1}{30D} \left(\frac{W}{\lambda} \right)^2 \quad (5.16)$$

where D is the maximum directivity.

For a small length directivity approximation ($W \leq 0.35\lambda$), the conductance of a uniform slot is:

$$G_{ES} = \frac{1}{90} \left(\frac{W}{\lambda} \right)^2 \quad (5.17)$$

Similarly, using the asymptotic directivity of an electrically long uniform source ($W > 2\lambda$) gives the long length conductance formula:

$$G_{ES} = \frac{1}{120} \left(\frac{W}{\lambda} \right) \quad (5.18)$$

The small length formula equals the long length expression for $W/\lambda = 1/2$.

For the electrical lengths comparable to the wavelength ($0.35\lambda \leq W \leq 2\lambda$), the conductance formula will be as follows [19]:

$$G_{ES} = \frac{1}{120} \left(\frac{W}{\lambda} \right) - \frac{1}{60\pi^2} \quad (5.19)$$

5.4.1.3 Cavity model for a uniform slot

The power radiated from each slot of PIFA can also be found using the cavity model theory (see Chapter 2). Assuming that the power radiated in the far field is substantially greater than the power dissipated in the near field, the real part of the complex Poynting vector can be found by integrating contributing far fields as follows:

$$P_r = \frac{1}{2} \operatorname{Re} \left(\int_V (\mathbf{E} \times \mathbf{H}^*) \cdot \mathbf{n} dV \right) = \frac{1}{2Z_0} \int_0^{2\pi} \int_0^{\pi/2} (|E_\theta|^2 + |E_\phi|^2) \cdot r^2 \sin \theta d\theta d\varphi \quad (5.20)$$

where E_θ, E_ϕ , are corresponding electric far field components [47], r - far field radius vector, Z_0 - free space impedance.

Again, equating the radiated power contributions from each of the PIFA slots in (5.20) with the power at the slot terminals as in (5.15) gives the expressions for the

corresponding slots conductances. The integral in (5.20) can be easily solved numerically in Matlab.

The results of the three methods are compared in Figure 5.4. The PIFA's endlslot inner height was $h = 1 \text{ mm} (\lambda/308)$.

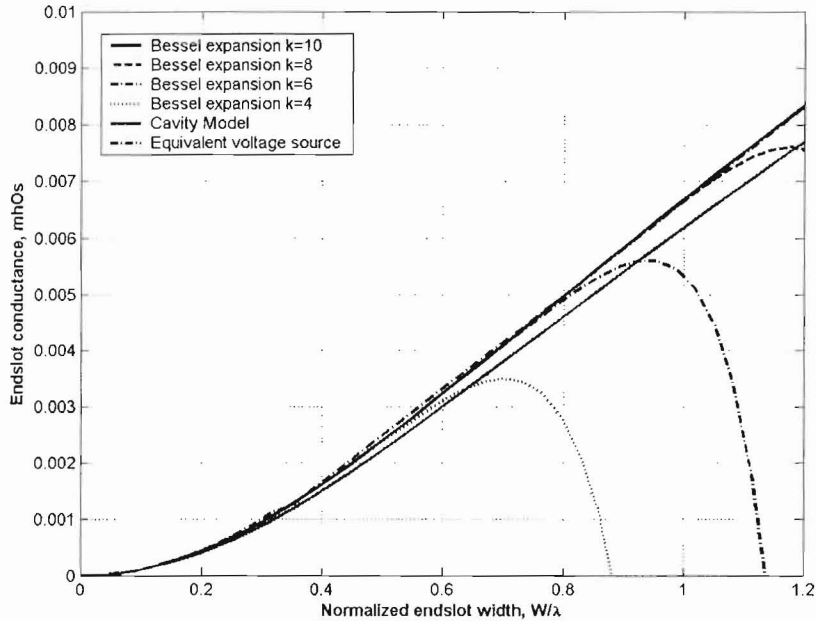


*Figure 5.4 PIFA endlslot conductance versus the normalized width according to: a) equivalent voltage source approach; b) aperture field integration method for different truncation factors; c) Cavity Model far field integration technique. *a) and c) are almost indistinguishable*

As can be seen from the Figure 5.4, the agreement between the Cavity Model results and aperture fields Bessel function expansion is very good. The influence of the truncation factor on the accuracy of the expansion expression is also obvious. In the case

of the rectangular PIFA with the endslot width less than or equal to a half of the wavelength, the truncation factor of $k = 4$ is adequate for modeling.

Also, the difference between the equivalent voltage source approach and aperture fields Bessel function expansion technique is less than 0.5% for the truncation factor $k = 10$.

5.4.2 Endslot susceptance

Despite its crucial impact on the frequency accuracy of the PIFA impedance modeling, the uniform end-slot susceptance turns out to be a considerably less researched topic than the conductance. In fact, as it was noted in [4], expression in (5.11) cannot be used to calculate the susceptance of the uniform slot as it is impossible to define a suitable aperture field. The issue here is that there is no information about the exact field shape in the slot. In order to obtain the imaginary part of the Poynting vector using the cavity model in a way similar to the real part, the PIFA near field information has to be available. That information has not been reported in the literature. In addition to that, [48] points out that the full-wave analysis does not provide accurate results for the uniform aperture susceptance.

Considering the above-mentioned shortcomings, approximate models are called on. These are based on the open-end or fringing effect concept.

5.4.2.1 Fringing effect model for a uniform slot susceptance

One of the many formulas available (see [4] for more) is based on open-end capacitance of a microstrip line [20]:

$$B_s = 0.01668 \frac{\Delta a}{h} \frac{W_e}{\lambda_0} \varepsilon_{re} = Y_0 \tan(\beta \Delta a) \quad (5.21)$$

where

$$\frac{\Delta a}{h} = 0.412 \frac{(\varepsilon_{re} + 0.3)(w/h + 0.264)}{(\varepsilon_{re} - 0.258)(w/h + 0.8)}. \quad (5.22)$$

Here, W_s is a function of W , h , and ε_r for a microstrip line, and is given in e.g. [4, 20, 48].

The fringing factor formula (5.22) has a different representation based on the Wiener-Hopf formulation (ibid.):

$$\frac{\Delta a}{h} = \frac{0.95}{(1 + 0.85k_0 h)} - \frac{0.75(\varepsilon_r - 2.45)}{(1 + 10k_0 h)} \quad (5.23)$$

It is claimed in [4, 48] that the accuracy of the last expression is 2 % for $0.1 < k_0 h < 0.6$ and for $2.45 < \varepsilon_r < 2.65$, but no measurement data is presented.

Finally, a more rigorous formula for characterization of an open-end microstrip susceptance has been claimed in [49] by curve fitting numerical data. The normalized outward extension of the radiating edge is given by:

$$\frac{\Delta a}{h} = (\xi_1 \xi_3 \xi_5 / \xi_4) \quad (5.24)$$

where the parameters $\xi_1, \xi_2, \xi_3, \xi_4, \xi_5$ are thoroughly defined (ibid.) and also in [4, 48].

Again, there is no measurement data presented – the curve fitting was performed on numerical data only. The accuracy of results given by the last formula is claimed to be better than 2.5 % for the range of normalized slot widths $0.01 \leq w/h \leq 100$ and $\varepsilon_r \leq 50$.

The three different formulations above are compared in Figure 5.5 (substrate inner height $h = 1\text{mm}$) for two substrate permittivity values.

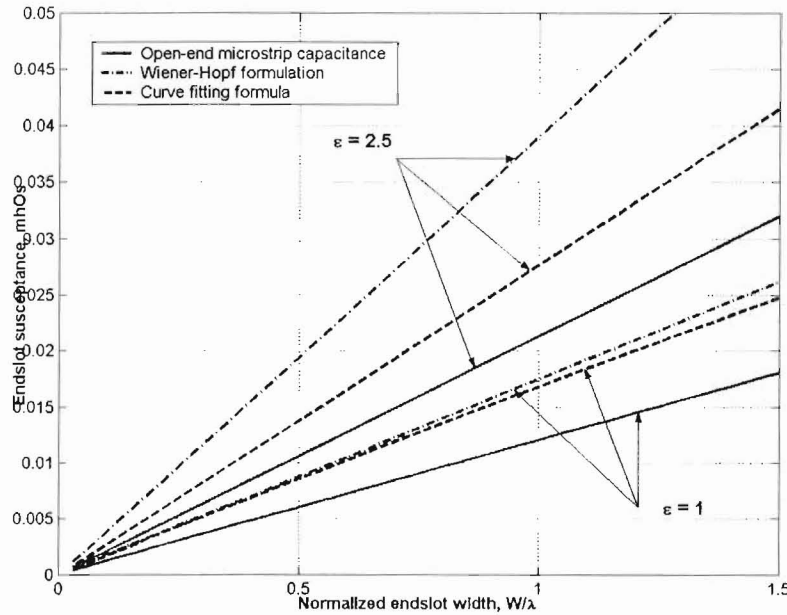


Figure 5.5 PIFA endslot susceptance versus the normalized width according to open-end capacitance formula, Wiener-Hopf approach, and curve fitting formula for two substrate permittivity values (substrate height $h=1\text{mm}$).

Comparing the plots, several observations could be made. Firstly, formulas (5.23) and (5.24) claim the accuracy of 2 % and 2.5% respectively for $\epsilon_r = 2.5$. As can be seen from the plots, the results provided by those formulas differ from each other substantially more than any of the above-mentioned percentages. Furthermore, the results provided by the open-end capacitance concept deviate from the other two formulations for both permittivity values.

It is therefore difficult to have confidence in the end-slot susceptance models. There is room for further research on this problem, including the effect of finite groundplanes with edges near the slots, which is relevant to compact antennas.

5.4.3 Sideslot conductance

The electric field in the sideslot aperture is assumed to be sinusoidal:

$$E_A = \frac{V_s}{h} \sin \frac{\pi z}{L} \hat{i}_z \quad (5.25)$$

where V_s is the excitation voltage across the aperture, h is an equivalent aperture height, and L - its equivalent width.

The problem of finding the PIFA sideslot admittance could be greatly simplified by using the equivalence (*Babinet*) principle of electromagnetism and Booker's relation e.g. [1, 31]. Booker's relation is an extension of Babinet's principle and it is usually written in terms of the admittance of the slot in question Y_s and the impedance of the corresponding complementary conducting structure Z_c at the corresponding feed point:

$$\frac{Y_s}{Z_c} = \left(\frac{2}{Z_0} \right)^2 \quad (5.26)$$

where Z_0 is a free space impedance. For instance, the resonant input resistance of the infinitesimally thin centre-fed dipole is 73Ω , so the resistance of the equivalent slot, fed at the centre point and allowed to radiate both sides of the slot, is approximately 487Ω .

Strictly speaking, the slot at hand is different from the pure sinusoidal slot, in fact it could be considered as a half-sinusoidal slot. Therefore, all the calculations for that type of slot should be adjusted accordingly.

5.4.3.1 Booker's formula approach

In order to use Booker's relation to calculate the PIFA sideslot conductance, it is necessary to obtain resistance information for the corresponding complementary conducting structure – i.e. dipole of the same width as slot. Fortunately, it is a well researched area, thus using identities and calculations of [31, 50] it is a relatively simple task to obtain the resistance data for an equivalent dipole. After that, using Booker's formula, the conductance (as well as the reactance) of the PIFA sideslot could be found.

5.4.3.2 Cavity model for a sinusoidal slot

In a similar manner, the power radiated from the PIFA sideslot can also be found using the cavity model theory (see Chapter 2).

Again, equating the radiated power contributions from the PIFA sideslots with the power at the slot terminals as in gives the expressions for the corresponding slots conductances. The integral of the real part of the Poynting vector can be easily solved numerically in Matlab.

5.4.3.3 Other models

[51, 52] describe different approaches in finding the sinusoidal slot admittance, which will be compared here as well.

The results are summarized in TABLE I . Comparison of the results from these show good agreement between different methods of calculation of sinusoidal side-slot admittance. The three above described methods' results are summarized and compared in TABLE I . PIFA's sideslot inner height was $h=1\text{mm}$ ($\lambda/308$).

TABLE I SIDE-SLOT ADMITANCE

Method	Admittance	
	Conductance, mhos* 10^{-3}	Susceptance, mhos* 10^{-3}
Booker, $L/h=20$	1.03	0.53
Booker, $L/h=153.85$	1.03	0.53
Cavity, $L/h=20$	0.92	n/a
Cavity, $L/h=153.85$	0.92	n/a
[51], $L/h=2.25$	0.9	0.15
[52], $L/h=2$	0.9	0.15
[52], $L/h=20$	1	0.45

As can be seen from the above table the agreement between the Cavity model and Booker's relation approach is good at half-wavelength slot width.

Also, comparison of the results from Figure 5.6 (Booker's approach) and those published in [51, 52] shows good agreement between different methods of calculation of sinusoidal sideslot conductance. The points at which comparisons were made are marked with stars on the plot.

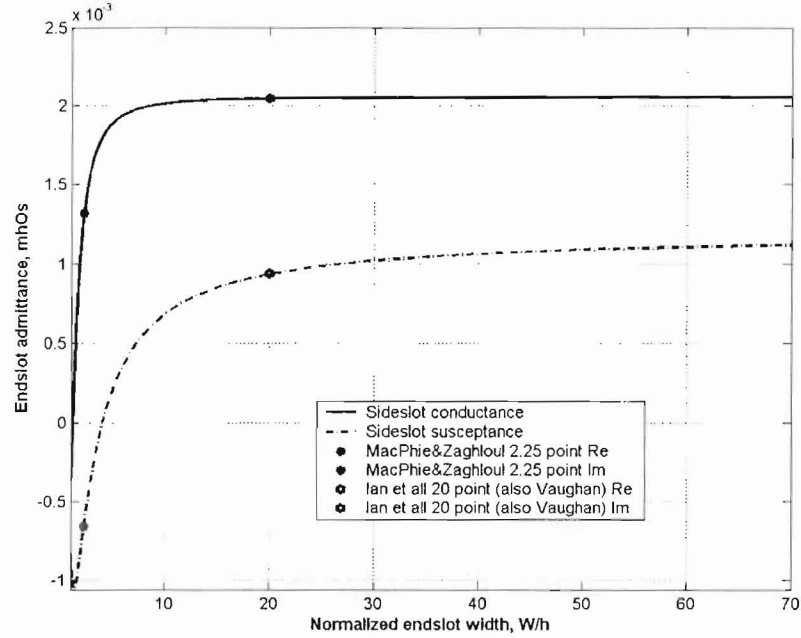


Figure 5.6 PIFA sideslot conductance and susceptance versus the normalized slot width (height is varied) according to Booker's relation approach ($L=\lambda/4$, $\epsilon_r=1$).

5.4.4 Sideslot susceptance

Using Booker's relationship for an imaginary part of the sideslot impedance yields the results presented in the Figure 5.7.

As can be seen from the last figure, the susceptance of the sideslot is very small at the slot width of half-wavelength. This data also confirms [51, 52] very well.

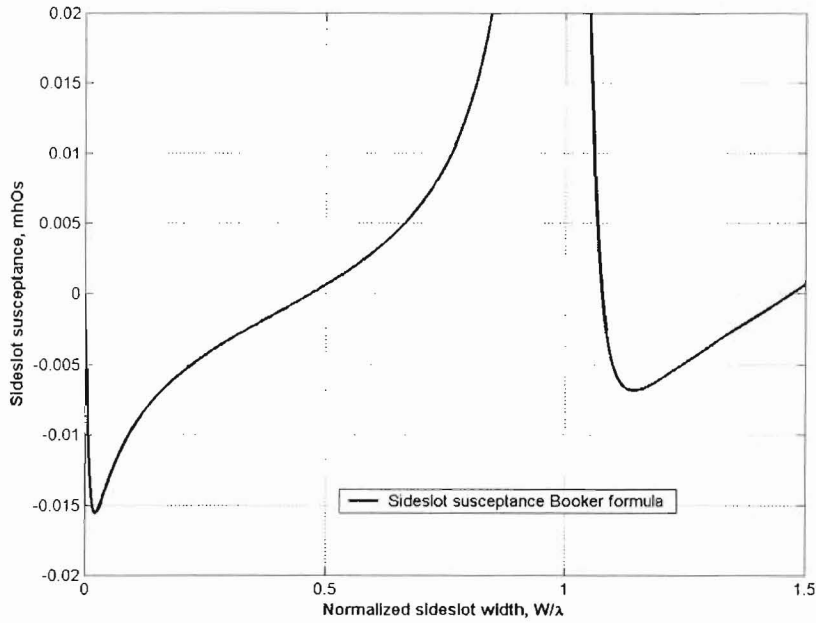


Figure 5.7 PIFA sideslot susceptance versus the normalized slot width according to Booker's relation approach (substrate height $h=1$ mm, $\epsilon_r = 1$).

5.4.5 Transmission line propagation constants and characteristic impedances

For proper transmission line analysis, transmission line propagation constants and characteristic impedances in the both PIFA length and width directions need to be found.

5.4.5.1 Length direction

The physical width of the microstrip line is W . According to [48], the characteristic impedance is:

$$Z_0 = \frac{\eta_0}{2\pi\sqrt{\epsilon_{re}}} \ln \left(F_1/u + \sqrt{1+4/u^2} \right) \quad (5.27)$$

where (ibid.):

$$F_1 = 6 + (2\pi - 6) \exp \left[-(30.666/u)^{0.7528} \right] \quad (5.28)$$

$$\eta_0 = 120\pi; \quad u = W/h \quad (5.29)$$

and this is claimed without justification to be good to 1%. No measurements are reported.

Now, the characteristic impedance for propagation in the length direction, Z_L , is calculated for a physical microstrip line width W and height h . The propagation constant for the length direction is found as follows:

$$\gamma_L = \frac{2\pi}{\lambda_L} \quad (5.30)$$

where

$$\lambda_L = \lambda_0 / \sqrt{\epsilon_{re}} \quad (5.31)$$

5.4.5.2 Width direction

Characteristic impedance and propagation constant in the PIFA width direction are Z_W , and γ_W , where the physical width of the line is L . These parameters are estimated using the wave number in width direction.

The PIFA width direction of propagation is assumed to be inside of half of a TE_{10} waveguide ($m=1, n=0$) (Figure 5.8). The cut-off wavelength in the TE_{10} mode is:

$$\lambda_c = \frac{2}{\sqrt{(n/h)^2 + (m/W)^2}} \quad (5.32)$$

Now, to calculate the effective width of the TE_{10} waveguide the fringing formula similar to the above mentioned (5.24), with the width extension of ΔL :

$$L_{eff TE_{10}} = L + 2\Delta L \quad (5.33)$$

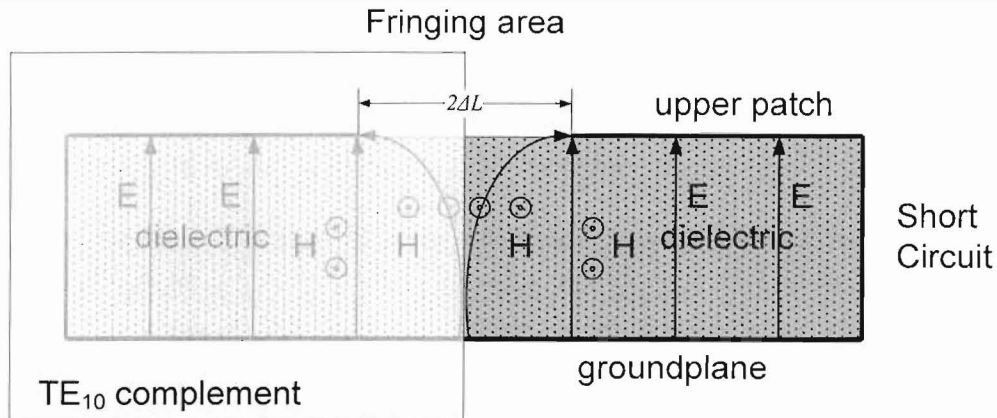


Figure 5.8 PIFA TE_{10} complement waveguide.

The propagation constant is then:

$$\gamma_w = \gamma_0 \sqrt{1 - \left(\frac{L}{L_{eff\ TE_{10}}} \right)^2} \quad (5.34)$$

The characteristic impedance in the width direction is:

$$Z_w = \frac{Z_0}{\sqrt{1 - \left(\frac{L}{L_{eff\ TE_{10}}} \right)}} \quad (5.35)$$

Finally, having found all the transmission line parameters, it is now possible to calculate the spatial PIFA impedance information according to that model.

5.5 Results and comparisons

The above described transmission line model was implemented in Matlab. The PIFA physical dimensions were taken as follows: length variable changes from $l=0$ (short

circuit) to $l=L=\lambda/4$, while width variable changes from $w=-W/2$ to $w=W/4$, where $W=\lambda/2$.

The w is indexed positive and negative from $w=0$ at the centre.

The edge slot is considered to be uniformly illuminated, and the reactive part of the slot impedance is estimated using a uniform half-wavelength dipole reactance and then applying the Booker's relationship.

The side slot admittance, as it was described earlier, is taken as an impedance of a quarter wavelength monopole in a half space, after Booker's formula is used to get the equivalent slot's impedance.

There is no probe correction factors added to the formulas and there are no finite ground plane effects considerations. There is also no loss in the transmission lines.

Calculated results from the three-slot transmission line model are plotted in Figure 5.9 along with the measurements data [1] and single-slot transmission line model results. Input impedance measurements were performed by [1] at the frequency, where the best 50 Ohm match of the antenna was found.

The agreement between the three-slot transmission line model and physical experiment results is good. However, for feed positions off the axis of symmetry, more measurement data is needed.

In order to obtain reliable measurements data off the center axis, a single mode PIFA brass prototype was built with the air substrate 1 mm thick. The feed points were pre-manufactured on the design stage to provide coverage of all upper patch area (see more in Chapter 6).

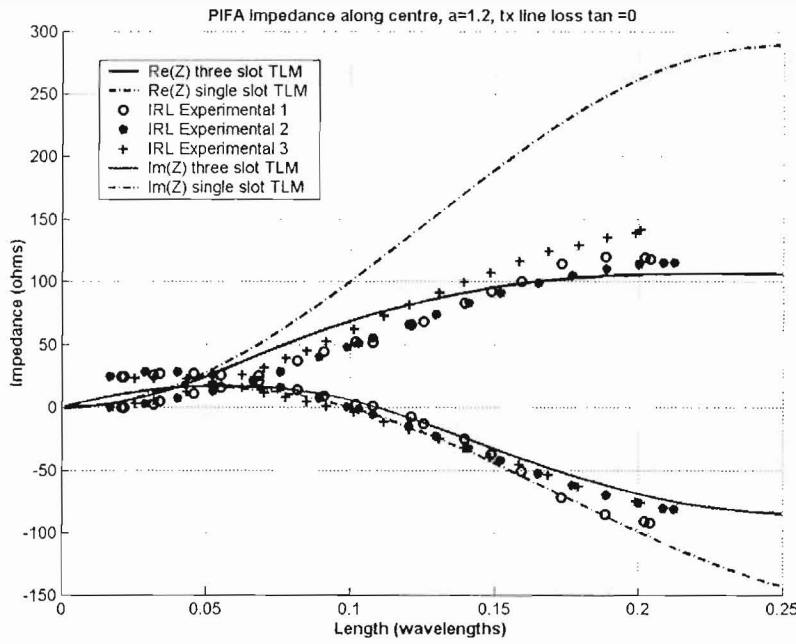


*Figure 5.9 PIFA input impedance as a function of feed position along the centre length of the antenna.
Experimental data is from [1] for three different PIFA heights.*

Also, the prototype replica was designed in commercial EM solving software CST Microwave Studio® and its impedance was calculated there using FDTD method.

The results of the measurements and numerical simulations across the endslot of the PIFA are plotted in Figure 5.10. The agreement gets worse towards the side edges of the patch. It must be noted that the agreement is very good around center of the PIFA up until approximately 0.15 of the wavelength of the antenna off the center. Nevertheless, from that point the theoretical, numerical and experimental curves start to depart producing differences up to 35 %.

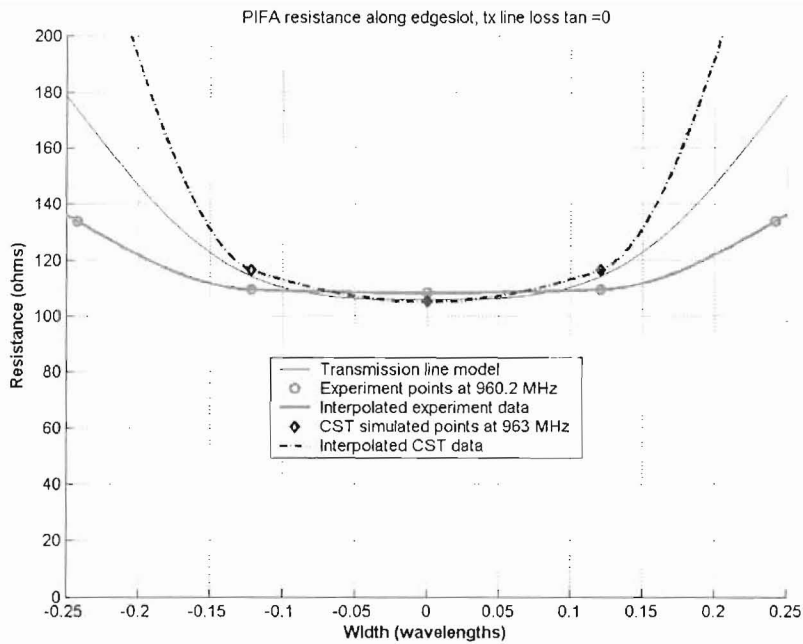


Figure 5.10 The PIFA input impedance as a function of feed position along the edge-slot of the antenna. The parameters of the PIFA: substrate thickness – 1mm, metal plate thickness t = 1.7 mm. W = 146 mm, L = 78 mm. The ground plane size: 400x300 mm (WxL).

Therefore, the transmission line model (as well as numerical EM software), in its current state of development still is not accurate over the whole PIFA patch space. A key limitation for the TLM, as noted above, lies with accurate expressions for the transmission line parameters, i.e., the propagation constants, and in particular, the terminating admittances.

As future work suggestions, the following steps can be proposed:

- 1) The loss inclusion has to be refined.
- 2) The propagation constants and the characteristic impedances for the transverse and lengthwise transmission lines have to be scrutinized.

- 3) Edge slot impedance reliable measurements or electromagnetic simulations data have to be obtained.
- 4) The model has to feature frequency dependent admittances and susceptances, in order to fringing formulas, edge impedance, as well as other transmission lines' parameters (metallic losses in particular), all to be functions of frequency.

6 MEASUREMENTS AND SIMULATIONS

6.1 Introduction

The main purpose of this section is to present and describe numerical and physical experiments techniques which were used to validate the quality of the theoretical predictions about the PIFA behavior and characteristics made in the preceding chapters. Much attention is also given to the PIFA prototypes' design considerations as well as numerical and measurements results discussion and conclusions.

6.2 PIFA impedance measurements considerations

In this section, only input impedance and bandwidth measurements aspects will be treated. The input impedance of the antenna as well as its impedance bandwidth will be obtained by measuring the reflection coefficient of a single port test system.

6.2.1 The reflection coefficient, VSWR

The reflection coefficient is the ratio of the input power to the output power of the test system. For a transmission line of length d , the reflection coefficient Γ is defined as:

$$\Gamma_0 = \frac{Z_L - Z_0}{Z_L + Z_0} \quad (6.1)$$

$$\Gamma(d) = \Gamma_0 e^{-2j\beta d} \quad (6.2)$$

Another parameter of interest is the *Voltage Standing Wave Ratio* (VSWR), which is defined as the ratio of the maximum voltage to the minimum voltage of the traveling

wave in a microwave system. The VSWR can be related to the *reflection coefficient* of the system by:

$$VSWR = \frac{|V_{MAX}|}{|V_{MIN}|} = \frac{1+\Gamma}{1-\Gamma} \quad (6.3)$$

From these definitions, the scattering parameters and the Smith Chart of the antenna system can be derived. Both are the important tools in analysis of antennas and microwave circuits.

6.2.2 Scattering parameters

The scattering parameters are the equations that determine the relationships between incident waves and reflected waves in an n -port network. Consider the two-port network shown in Figure 6.1.

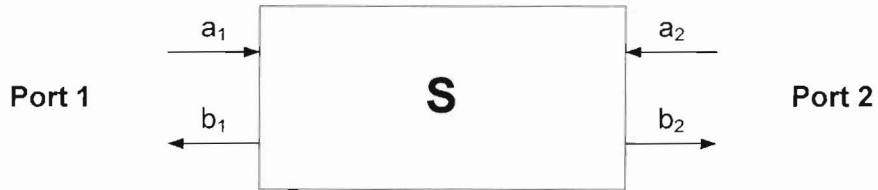


Figure 6.1 The 2 port network.

In this network, a_n defined as the normalized incident wave voltage, and b_n , as the normalized reflected wave voltage. They are defined as:

$$a_n = \frac{1}{2\sqrt{Z_0}}(V_0 + Z_0 I_n) \quad (6.4)$$

$$b_n = \frac{1}{2\sqrt{Z_0}}(V_0 - Z_0 I_n) \quad (6.5)$$

The above equations can be used for a general n port network.

The scattering parameters matrix of the above system relates the incident waves to the reflected waves in the following way:

$$\begin{bmatrix} b_1 \\ b_2 \end{bmatrix} = \begin{bmatrix} S_{11} & S_{12} \\ S_{21} & S_{22} \end{bmatrix} \begin{bmatrix} a_1 \\ a_2 \end{bmatrix} \quad (6.6)$$

Solving for each of S -parameters yields:

$$S_{11} = \frac{b_1}{a_1} \Bigg|_{a_2=0} \quad (6.7)$$

$$S_{21} = \frac{b_2}{a_1} \Bigg|_{a_2=0} \quad (6.8)$$

$$S_{22} = \frac{b_2}{a_2} \Bigg|_{a_1=0} \quad (6.9)$$

$$S_{12} = \frac{b_1}{a_2} \Bigg|_{a_1=0} \quad (6.10)$$

The voltage and the current at a port can be expressed in terms of a_n and b_n :

$$V_n = \sqrt{Z_0} (a_n + b_n) \quad (6.11)$$

$$I_n = \frac{1}{\sqrt{Z_0}} (a_n - b_n) \quad (6.12)$$

The power flow of the network is equal to:

$$P_n = \frac{1}{2} \operatorname{Re} \{ V_n I_n \} = \frac{1}{2} \left(|a_n|^2 - |b_n|^2 \right) = \frac{|a_n|^2}{2} \left(1 - \frac{|b_n|^2}{|a_n|^2} \right) \quad (6.13)$$

On the other hand, the power at the port is defined in terms of its reflection coefficient:

$$P_n = \frac{|V_n^+|^2}{2Z_0} \left(1 - |\Gamma_n|^2\right) \quad (6.14)$$

Comparing equations (6.13) and (6.14) it can be seen that the parameters S_{11} and S_{22} are equal to the input and output reflection coefficients, respectively, of the two-port network. It can also be shown that the parameters S_{21} and S_{12} are equivalent to the forward and reverse voltage gains of the two-port network.

6.2.3 Bandwidth

The notion of impedance bandwidth of an antenna was introduced in earlier sections. The bandwidth can be defined in terms of the antenna Q-factor and VSWR e.g. [46]:

$$BW = \frac{VSWR - 1}{Q\sqrt{VSWR}} \quad (6.15)$$

for a VSWR of 2:1, the BW simplifies to:

$$BW = \frac{1}{Q\sqrt{2}} \quad (6.16)$$

The impedance bandwidth of an antenna system is inversely proportional to the system's quality factor. Since the Q-factor is inversely related to the antenna's electrical size (see Section 4), the impedance bandwidth is expected to be linearly proportional to the antenna's electrical size. Measured bandwidth values are reported in corresponding sections along with theoretically predicted figures.

6.3 PIFA prototype design considerations

As it was mentioned earlier, the main purpose of performing a set of PIFA measurements for this work was to validate theoretical predictions about the PIFA impedance, bandwidth, and resonant frequency made by the Cavity Model and the Transmission Line Model in previous sections. In order to achieve the goal, several requirements must be considered when designing the PIFA prototype:

1. The feed position of PIFA must be variable to obtain impedance readings at several points of interest across the PIFA area;
2. The height of the prototype must be small to retain TM_{01} mode purity inside the PIFA cavity to conform to the theoretical models;
3. The groundplane of the PIFA prototype must be of manageable size while providing enough area to emulate an infinite extent provision.

While the latter requirement was relatively easy to satisfy, the former two conditions proved to be more challenging to meet.

6.3.1 Prototype I

The first prototype (and all subsequent) was manufactured using 1.8 mm thick brass plates with coaxial feed via an SMA connector fixed to the ground plane sheet of size 300x400 mm. The upper patch of the antenna was made together with the shorting wall from one metal sheet by bending. In order to obtain variable feed positions across the PIFA, the upper piece was connected to the ground plane using conducting copper tape. The inner height of the prototype was $h = 7.2$ mm.

However, it was found in the course of experiment that the electrical contact provided by copper tape between the upper piece and the ground plane could not provide for repeatability of the experiments' results.

In addition to that, the chosen height of the PIFA, while improving bandwidth of the prototype, resulted in generation of higher modes of the antenna system.

6.3.2 Prototype II

To eliminate generation of higher modes, it was decided to manufacture very thin PIFA, thus neglecting the bandwidth performance, but retaining the modal purity. The chosen height of the antenna was $h = 1\text{mm}$.

To obtain variable feed points and retain repeatability of experiments, approach that is more straightforward was chosen. It was decided to manufacture several prototypes with fixed feeds at different places across the patch. The upper piece of the PIFA was soldered to the ground plane sheet.

The achieved modal purity of this PIFA prototype was very good, which satisfied the second requirement.

Unfortunately, while providing good modal purity this approach suffered from even minor manufacturing errors in the PIFA cavity construction. It proved to be very challenging to build several electromagnetically identical 1 mm thick PIFA cavities using conventional mechanical shop tools.

6.3.3 Prototype III

Finally, a simple way of varying the PIFA feed points while retaining the modal purity was found. One thin ($h = 1$ mm) brass prototype was manufactured conventionally by soldering the upper piece to the ground plane. However, both upper plate and the ground plane had via holes for SMA connectors at the corresponding points of interest. The picture of the prototype from the top and bottom are shown in Figure 6.2.

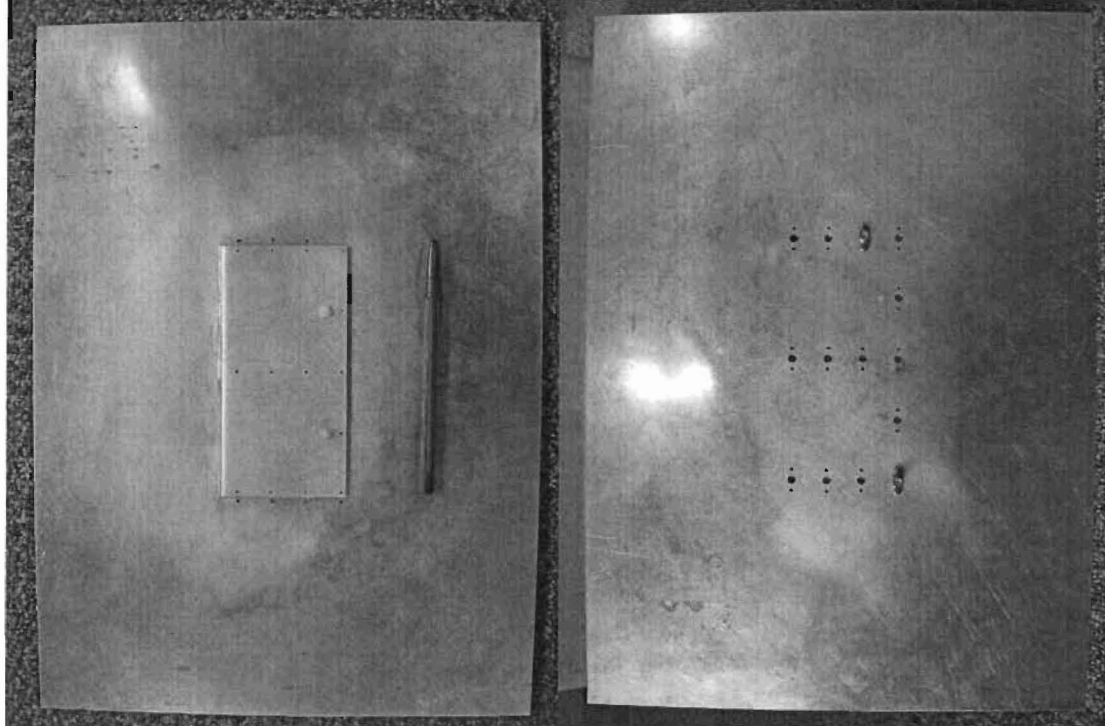


Figure 6.2 Rectangular PIFA prototype III. Via holes and SMA connectors are seen. Pen provided for scale. Patch: $W = 148\text{mm}$, $L = 74\text{mm}$, substrate height (air): 1mm ($\lambda/308$), plate thickness (brass): 1.7 mm ($\lambda/181$), groundplane: $W = 400\text{mm}$, $L = 300\text{mm}$

Also, the two nylon pins visible in the picture, were used to improve stability and accurateness of the PIFA cavity shape.

To obtain experimental readings in different points across the PIFA, the SMA connectors with the 50 Ohm coaxial feed were placed at these points and held by a pair of screws. Copper tape was used to cover the remaining unused holes in the plates. However, as it was predicted and confirmed experimentally, the effect of the open holes on the PIFA electromagnetic characteristics was negligible even without the tape.

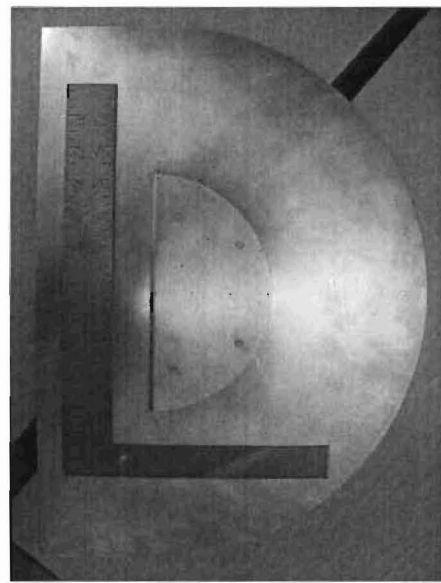


Figure 6.3 Semicircular PIFA prototype III. Via holes and nylon washers are seen. Ruler provided for scale. Patch radius: $a = 90\text{mm}$, substrate height (air): 1mm ($\lambda/328$), plate thickness (brass): 1.7 mm ($\lambda/199$).

6.4 PIFA test-set layout

The test setup consisted of a HP8510B network analyzer, HP8514A S-Parameter Test set, HP8341B function generator, and a personal computer. The function generator was only used to supply the network analyzer with a 10MHz reference clock. Each device was connected using GPIB connections. Figure 6.4 shows the overall test setup.

Later, with acquisition of a new Agilent E5071B ENA network analyzer, the functions of vector network analyzer, function generator, PC and GPIB interface were conveniently delegated to the E5071B.

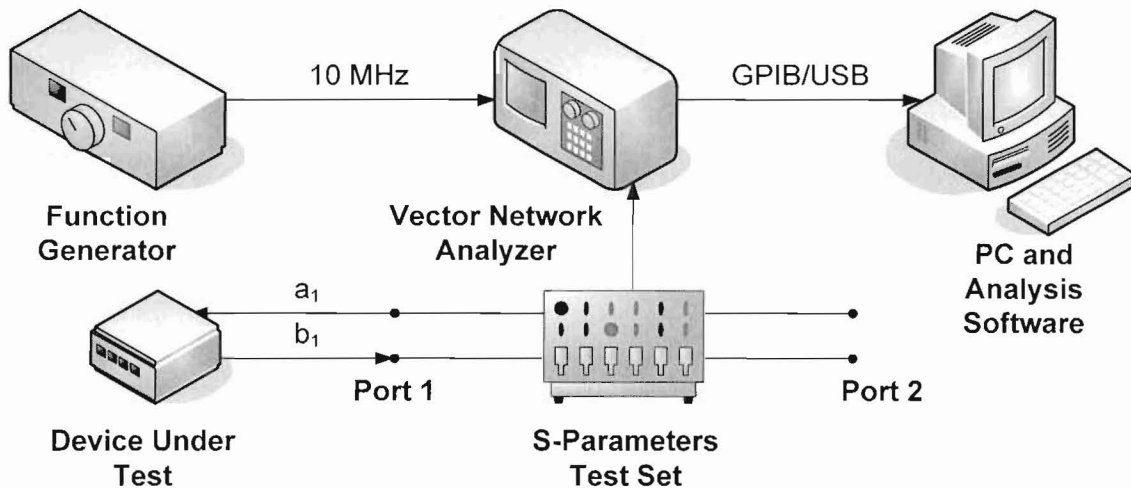


Figure 6.4 PIFA test setup.

The computer was able to control the network analyzer and acquire data using HP ADS software. The software measured the magnitude and phase of the S11 parameter over a given frequency range and saved the data in either ASCII text or *.csv file that could be easily accessed in Matlab or HP ADS.

The network analyzer was calibrated at the end of the connecting coaxial cable, to negate losses in the cable. The HP 85052A calibration kit was used to calibrate the system to a shorted, open, and terminated load. 3.5mm connectors were used. There was also an added electrical loss in the connector mounted to the ground plane of the antenna, which was compensated manually in the network analyzer. The Agilent 85092-60008 electronic calibration module was used to calibrate the E5071B ENA.

6.5 PIFA far field measurements considerations

For precise far field measurements of the PIFA prototypes, the Satimo anechoic chamber was used at Sierra Wireless Richmond, BC facility. This is a newly constructed anechoic chamber for fast measurements of radiating performance in the radiation near field. An array of 64 dual polarized antennas encircles the *device under test* (DUT), which is placed on a rotating table as shown in the Figure 6.5. All the antennas probe the transmitted signal at one sweep so that by rotating the DUT table in horizontal plane the full far field 3D measurement can be obtained. The far field is then calculated by fast Fourier transform (FFT) in the supplied software.

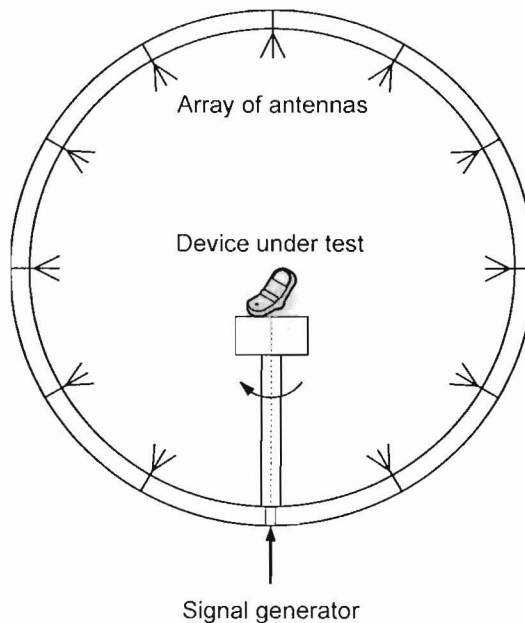


Figure 6.5 Satimo Anechoic chamber setup.

The chamber was also used in to do passive measurements on radiated power. By measuring an external signal coming directly to the probe antennas (one at a time) on one

side, while measuring total radiated power of the antenna at the other end, the antenna efficiency could be calculated.

6.6 PIFA numerical simulation with commercial software packages

In recent years, the area of antenna research and development has become increasingly dominated by commercial electromagnetic solving software packages. While this incentive greatly simplifies an antenna development cycle, the question of accurateness and universalism of the electromagnetic solvers is still open.

In particular, it is of a great interest to find out how accurate those solvers can predict major electromagnetic characteristics of PIFA, such as impedance behavior, resonant frequency and bandwidth, as well as far field patterns.

The two electromagnetic simulation packages were used at different stages of this work are WIPL-D by WIPL-D d.o.o., and CST Microwave STUDIO by Computer Simulation Technology.

The above mentioned solvers differ greatly not only in functionality and features they provide, but also in the fundamental methods of electromagnetic computing.

6.7 Results and comparisons

6.7.1 Rectangular PIFA impedance and resonant frequency

Extensive study of the PIFA's input impedance as a function of the feed position across the PIFA's patch area is presented in Sections 4 and 5 along with experimental and numerical results.

However, there are several things which might provide more insightful view on the PIFA's impedance behavior.

Strictly speaking, when studying resonant antennas (in this particular case - the PIFA), the definition or type of impedance resonance used must be pronounced. In fact, there are two types of resonances, which can be defined in the PIFA resonant cavity.

The first type of resonance occurs when the reactive part of the complex input impedance is equal to zero – the so called *circuit resonance*. In an ideal circuit, this resonance coincides with the maximum of the real part of the input impedance. However, due to different factors, such as antenna losses, parasitic reactances, and coupling, the zero of the antenna reactance does not necessarily align with its resistance maximum.

In the latter case, the resonant behavior of the antenna is judged by its resistance' maximum only. Throughout this investigation, except where stated to the contrary, the PIFA's resonance is taken at the frequency where its input resistance is at its maximum.

The plots of the measured and simulated rectangular PIFA input impedance versus the frequency are furnished in the Appendix 9.6. As can be seen from these plots, the frequencies at which maximum resistance occurs do not align with those where the reactance of the PIFA is equal to zero for above mentioned reasons.

Figure 6.6 and Figure 6.7 show these measured and simulated PIFA's resonant frequencies for each probe feed position across the PIFA as discussed earlier. The values of the resonant frequencies did not remain constant over the entire range of the feed positions, varying less than 2.3% for the measurements results.

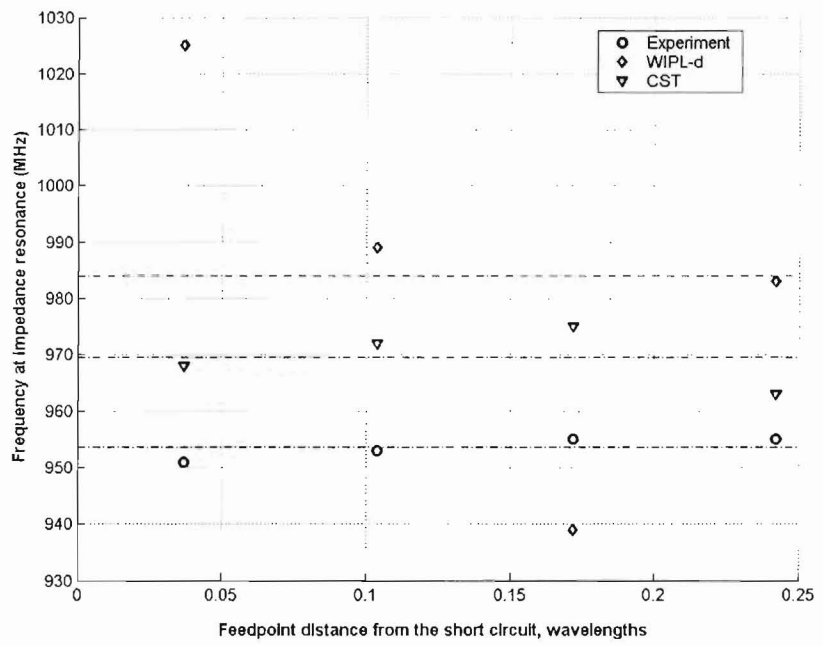
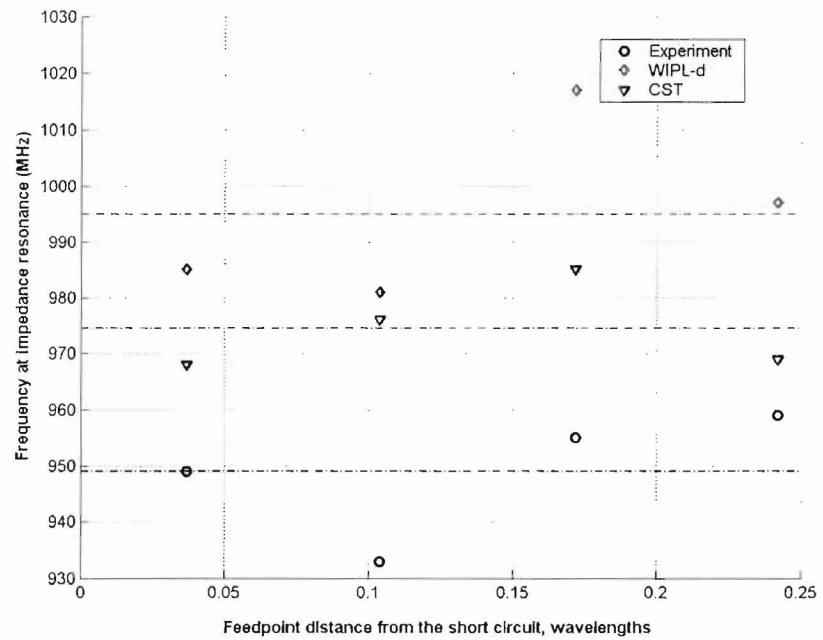


Figure 6.6 Measured and simulated resonant frequency of the probe-fed rectangular PIFA along center (top) and one of its sideslots (bottom) versus the feed position.

Several observations can be made from the plots. Firstly, the PIFA's resonant frequency does not remain constant for the entire range of the feed positions across the PIFA patch. Particularly, this is true when feeding the antenna along its length at the center width. This effect is somewhat mitigated when feeding at either of the PIFA sideslots. Finally, it is interesting to note that the PIFA's resonant frequency remains constant when feeding along its endslot for up to 0.15 wavelengths from its middle.

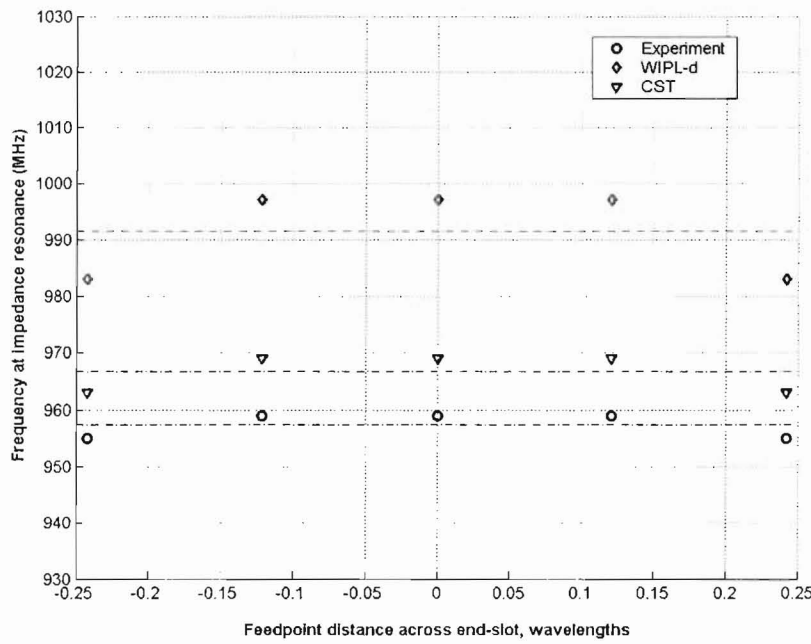


Figure 6.7 Measured and simulated resonant frequency of the probe-fed rectangular PIFA along its endslot versus the feed position.

In addition, as can be seen from the plots, the numerical EM solvers, such as WIPL-d and CST Microwave do not provide very accurate results in terms of the PIFA input impedance (especially when feeding from the sideslots). The PIFA's resonant frequency prediction of the EM solvers is also somewhat inaccurate even though the CST

Microwave provides the resonant frequency behavior across the PIFA patch resembling that of the measured results. The dotted lines in the plots provide information on the averaged resonant frequency obtained for each cut.

6.7.2 Semicircular PIFA impedance and resonant frequency

The plots of the measured semicircular PIFA input impedance versus the frequency are also furnished in the Appendix 9.6. As it was the case for the rectangular PIFA, the frequencies at which maximum input resistance occurs also do not align with those where the input reactance of the semicircular PIFA is equal to zero for the similar mentioned reasons.

Measured semicircular PIFA's resonant frequencies for each probe feed position across the PIFA are provided in Figure 6.8. The values of the resonant frequencies did not remain constant over the entire range of the feed positions. However, the resonant frequency variation was much less than that of the rectangular PIFA, - the order of 0.5% for the measurements results.

As it was for the rectangular PIFA, the resonant frequency did not remain constant when feeding along the center. Also, this effect becomes less pronounced when feeding off the center, 45° away from the center radius.

Also, it is interesting to note, that the average measured resonant frequency of the semicircular PIFA remained remarkably constant for the entire range of feed positions used (the thin lines on the plots).

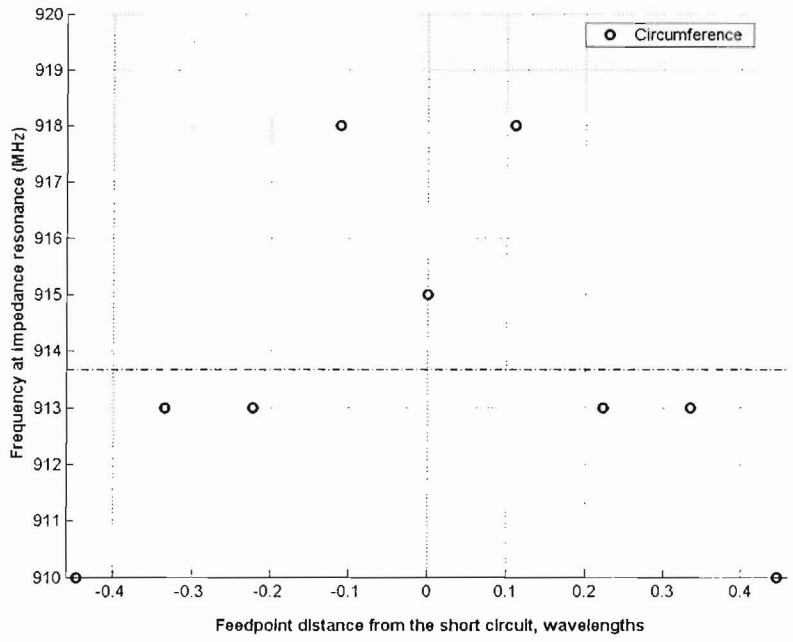
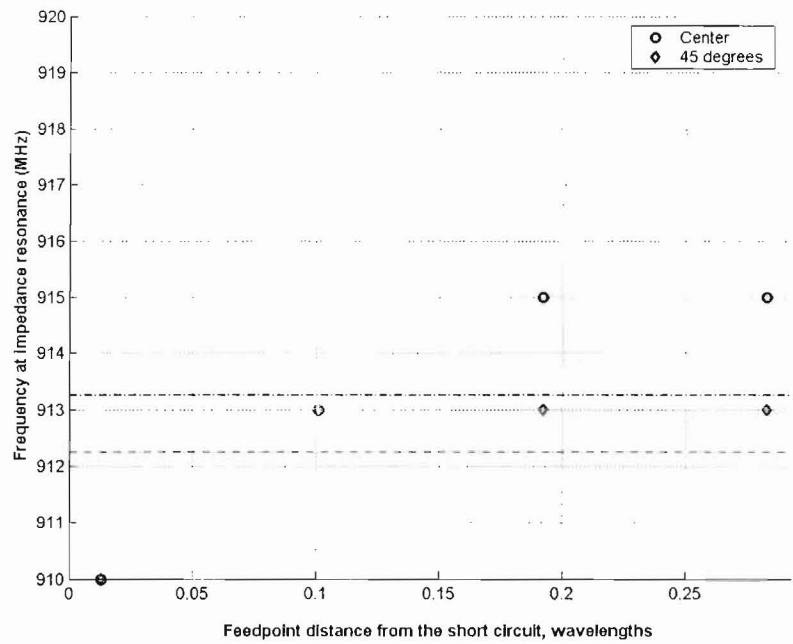


Figure 6.8 Measured and simulated resonant frequency of the probe-fed semicircular PIFA along its center, 45 degrees off the center (top) and PIFA along its circumferential endslot (bottom) versus the feed position.

6.7.3 Rectangular PIFA far fields

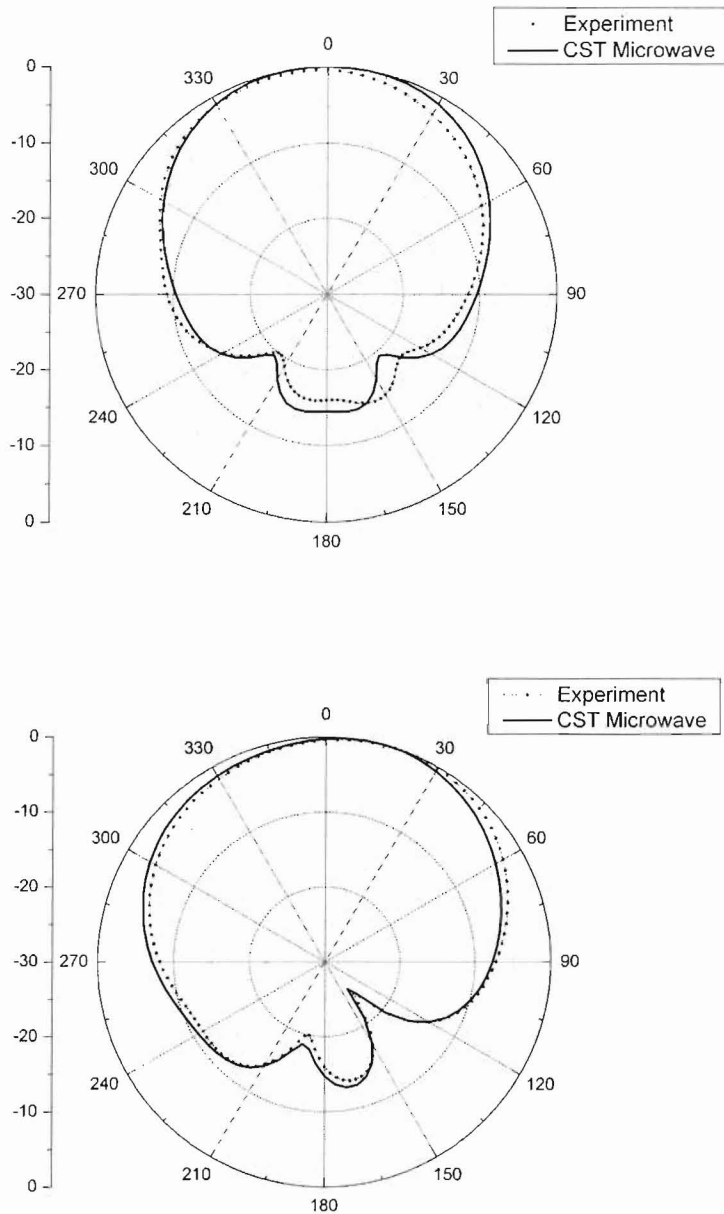


Figure 6.9 The rectangular PIFA far field in the: H-plane ($\phi = 0$) – top and E-plane ($\phi = 90^\circ$) – bottom. Parameters of the PIFA: $W = 148\text{mm}$, $L = 74\text{mm}$, Ground plane size: $W \times L = 400 \times 300 \text{ mm}$. Resonant frequency $f_r = 975 \text{ MHz}$.

Measured and simulated far fields of the thin rectangular PIFA prototype with the finite ground-plane are presented in Figure 6.9- Figure 6.10:

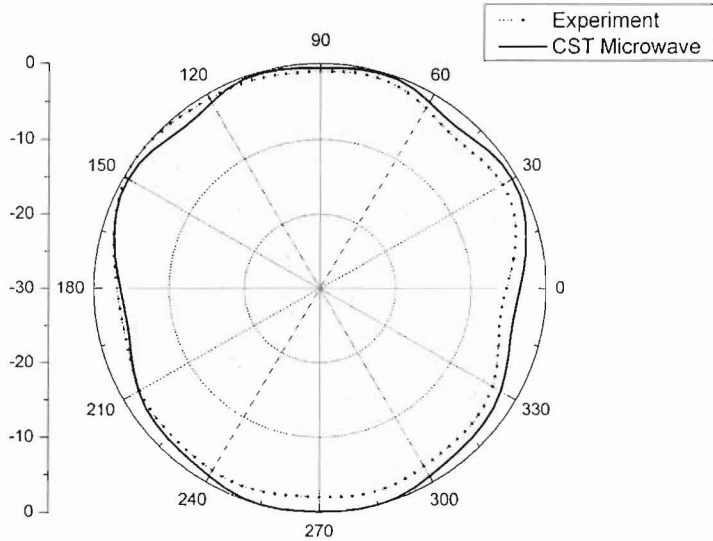


Figure 6.10 The rectangular PIFA far field in the XY-plane ($\theta = 90^\circ$). Parameters of the PIFA: $W=148\text{mm}$, $L=74\text{mm}$, Ground plane size: $W \times L = 400 \times 300 \text{ mm}$. Resonant frequency $f_r = 975 \text{ MHz}$.

As can be seen from the plots, the agreement between the measured and simulated results is very good in all principal planes of radiation for various angles. Minor misalignment discrepancies of the plots are caused by non-ideal placement of the PIFA prototype relative to the anechoic chamber's phase center.

The gain of the PIFA prototype from CST was 5.9 dBi, while the measured gain was 4.3 dBi, with measured efficiency (using the Satimo chamber) of about 65% (ie., about -1.9dB).

6.7.4 Semicircular PIFA far fields

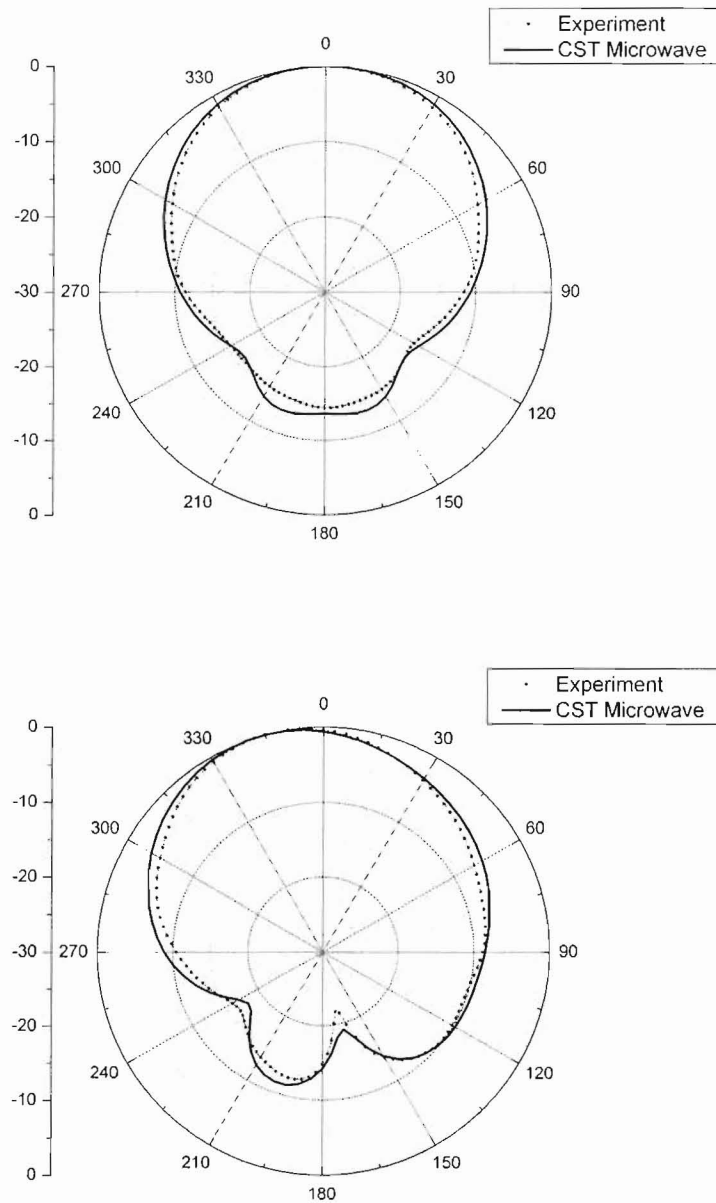


Figure 6.11 The semicircular PIFA far field in H-plane ($\phi = 0$) – top and E-plane ($\phi = 90^\circ$) – bottom. Parameters of the PIFA: $a = 90\text{mm}$, resonant frequency $f_r = 915\text{ MHz}$.

Measured and simulated far fields of the thin semicircular PIFA prototype with the finite ground-plane are presented in Figure 6.11 - Figure 6.12.

As it was for the rectangular PIFA, the agreement between the measured and simulated results is very good in all principal planes of radiation for various angles.

The directive gain predicted by CST was 6.9 Dbi/m while the measured gain was 3.8 Dbi/m. Measured efficiency of the antenna was 45 %.

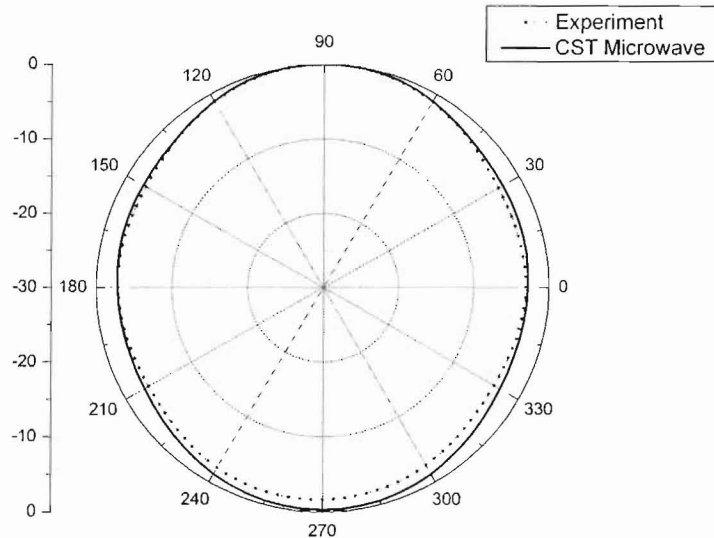


Figure 6.12 The semicircular PIFA far field in the XY-plane ($\theta = 90$). Parameters of the PIFA: $a = 90\text{mm}$, resonant frequency $f_r = 915\text{ MHz}$.

It can be concluded from the data presented here that the numerical FDTD solver of CST Microwave provides very accurate results for the PIFA far fields prediction.

7 CONCLUSIONS

This chapter summarizes the material presented in this thesis. In addition, it emphasizes the contributions of the conducted research work and outlines the conclusions that can be drawn from them.

7.1 Summary and contributions

This dissertation has dealt with theoretical investigation, modeling and design of planar inverted F-antennas. Two most popular geometries of PIFA were considered: rectangular and semicircular PIFA's. Theoretical investigation and modeling included cavity model analysis and transmission line model analysis of the PIFA's. Experimental investigation of the PIFA's included numerical simulations using full wave analysis methods, namely, method of moments and finite difference time domain technique, as well as extensive prototyping and physical measurements of the PIFA's.

The research work presented in this thesis resulted in many contributions to the area of PIFA modeling and design. The contributions in the PIFA modeling include:

- Simple cavity-based three-slot rectangular PIFA model to determine the antenna far field patterns, polarization, input impedance, Q-factor and bandwidth;
- Simple cavity-based semicircular PIFA model to determine the antenna far field patterns, polarization, input impedance, Q-factor and bandwidth;

- An investigation of the impact of the PIFA's substrate permittivity and height on the PIFA Q-factor and bandwidth characteristics;
- An investigation of the PIFA's circular polarization radiation capabilities and the impact of the PIFA's finite groundplane on the CP purity;
- Simple three-slot transmission line model for rectangular PIFA to obtain the antenna input impedance at any feed point across its upper patch area;
- An investigation of the PIFA's slots admittance data and propagation constants for the abovementioned transmission line model;
- An extensive comparative study of the theoretically predicted results versus the results obtained by the Method of Moments and FDTD solvers as well as physical measurements for the PIFA's far fields, polarization, input impedance, and bandwidth.

7.2 Conclusions

Most designs for PIFA's use numerical experimentation to get a basic conception. However, the cavity model and the transmission line method are still advantageous in terms of analysis computation time and they also offer different insights to the operating mechanism of the PIFA.

The rectangular PIFA's was therefore investigated using its respective three-slot cavity and transmission line model. The significant influence of including the side-slots of the PIFA is evident from the pattern shape, polarization, and input impedance. The PIFA produces both circular polarizations and this is extremely pure in both hands in their respective, specific directions. The rectangular PIFA has a lower Q compared to the

analogous square patch. The transmission line model revealed that the PIFA's input impedance can be accurately predicted across its patch area to within about 0.15 wavelengths from the center line of the width. The biting constraint for frequency accuracy is the accuracy of the edge susceptance, a long-standing problem, and so the current models for these have been reviewed.

The semicircular PIFA's was investigated using its cavity model only. The significance of this analysis' results is in the fact that derived far field pattern is almost identical to that provided by the three-slot cavity model for the rectangular PIFA. This means in turn that those types of PIFA are interchangeable in the sense of their radiating characteristics. Also, the equivalent three-slot filament magnetic source arrangement of the rectangular PIFA can be seen in a far field as a semicircular sinusoidal filament current of the semicircular PIFA.

The experiment test setup, PIFA prototypes design, and measurement technique described in this thesis, can also be successfully employed in the PIFA prototyping and design in conjunction with above described models. The numerical electromagnetic solvers employed in this work can be successfully used in the PIFA design, but some degree of caution must be exercised when interpreting and using those solvers' results.

7.3 Future work

The future work in this area must include the finite groundplane effects analysis for the cavity model far fields calculation and for the transmission line model slots admittances.

Also, the electric vector potential for the semicircular PIFA far fields can be attempted to be solved analytically, not numerically. The semicircular PIFA input impedance information can be investigated using the cavity model as well.

For progress in accurately predicting the frequency behavior using the transmission line model, new results are needed for the edge admittances. This is complicated by the non-uniform illumination of the end-slot.

Also, the PIFA arrays for wireless applications can be proposed with both fixed CP directions and/or broad scan angles.

The PIFA MIMO and diversity applications must also be addressed in detail, owing to PIFA's compactness and suitability for multi-antenna configurations. Mutual coupling effects of PIFA elements in different array structures is also of great interest.

8 BIBLIOGRAPHY

- [1] R. Vaughan and J. Bach Andersen, *Channels, Propagation and Antennas for Mobile Communications.*, vol. 50, London: Institution of Electrical Engineers, 2003, pp. 753.
- [2] G. Deschamps, "Theoretical Aspects of Microstrip Waveguides," *Communications Systems, Transactions of the IRE Professional Group on*, vol. 2, pp. 100-102, 1954.
- [3] J. Howell, "Microstrip antennas," in 1972, pp. 177-180.
- [4] J. R. James and P. S. Hall, *Handbook of Microstrip Antennas*. London, Eng.: Peregrinus, 1989,
- [5] B. M. Green, M. A. Jensen and Y. Rahmat Samii, "Dual-mode antenna for satellite/terrestrial communications," in 1996, pp. 66-69 vol.1.
- [6] C. R. Rowell and R. D. Murch, "A capacitively loaded PIFA for compact PCS handsets," in 1996, pp. 742-745 vol.1.
- [7] R. Kronberger, H. Lindenmeier, L. Reiter and J. Hopf, "Multiband planar inverted-F car antenna for mobile phone and GPS," in 1999, pp. 2714-2717 vol.4.
- [8] W. J. Krzysztofik, "Two-band planar arrays for GPS and/or GSM terminals," in 2002, pp. 756-759 vol.4.
- [9] M. Z. Azad and M. Ali, "A miniaturized implantable antenna for GPS application," in 2006, pp. 1103-1106.
- [10] J. Kim and Y. Rahmat-Samii, "Implanted antennas inside a human body: simulations, designs, and characterizations," *Microwave Theory and Techniques, IEEE Transactions on*, vol. 52, pp. 1934-1943, 2004a.
- [11] J. Kim and Y. Rahmat-Samii, "Low-profile antennas for implantable medical devices: Optimized designs for antennas/human interactions," in 2004b, pp. 1331-1334 Vol.2.
- [12] Y. J. Cho, Y. S. Shin and S. O. Park, "Internal PIFA for 2.4/5 GHz WLAN applications," *Electronics Letters*, vol. 42, pp. 8-10, 2006.
- [13] Kin-Lu Wong, An-Chia Chen and Yen-Liang Kuo, "Diversity metal-plate planar inverted-F antenna for WLAN operation," *Electronics Letters*, vol. 39, pp. 590-591, 2003.

- [14] M. Ali and G. J. Hayes, "Analysis of integrated inverted-F antennas for bluetooth applications," in 2000, pp. 21-24.
- [15] T. Tiehong and Z. Zheng, "Applications of planar inverted-F antenna for bluetooth," in 2003, pp. 1230-1233 vol.2.
- [16] Se-Keun Oh, Hyung-Sik Yoon and Seong-Ook Park, "A PIFA-Type Varactor-Tunable Slim Antenna With a PIL Patch Feed for Multiband Applications," *Antennas and Wireless Propagation Letters*, vol. 6, pp. 103-105, 2007.
- [17] Y. Gao, X. Chen, C. Parini and Z. Ying, "Study of a dual-element PIFA array for MIMO terminals," in 2006, pp. 309-312.
- [18] Ki-Jin Kim, Won-Gyu Lim and Jong-Won Yu, "High isolation internal dual-band planar inverted-F antenna diversity system with band-notched slots for MIMO terminals," in 2006, pp. 1414-1417.
- [19] J. R. James, P. S. Hall and C. Wood, *Microstrip Antenna : Theory and Design.* , vol. 12, London ; New York: Peregrinus on behalf of the Institution of Electrical Engineers, 1981, pp. 290.
- [20] I. J. Bahl and P. Bhartia, *Microstrip Antennas*. Dedham, Mass.: Artech House, 1980, pp. 348.
- [21] K. Hirasawa and M. Haneishi, *Analysis, Design, and Measurement of Small and Low-Profile Antennas*. Boston: Artech House, 1992, pp. 270.
- [22] H. Pues and A. van de Capelle, "Accurate transmission-line model for the rectangular microstrip antenna," *IEE Proceedings H: Microwaves Optics and Antennas*, vol. 131, pp. 334-340, dec. 1984.
- [23] Y. Lo, D. Solomon and W. Richards, "Theory and experiment on microstrip antennas," *Antennas and Propagation, IEEE Transactions on [Legacy, Pre - 1988]*, vol. 27, pp. 137-145, 1979.
- [24] A. Derneryd, "Analysis of the microstrip disk antenna element," *Antennas and Propagation, IEEE Transactions on [Legacy, Pre - 1988]*, vol. 27, pp. 660-664, 1979.
- [25] P. Pinho and J. F. Rocha Pereira, "Design of a PIFA antenna using FDTD and genetic algorithms," in 2001, pp. 700-703 vol.4.
- [26] M. N. O. Sadiku and A. F. Peterson, "A comparison of numerical methods for computing electromagnetic fields," in 1990, pp. 42-47 vol.1.
- [27] M. N. O. Sadiku and C. N. Obiozor, "A comparison of finite difference time-domain (FDTD) and transmission-line modeling (TLM) methods," in 2000, pp. 19-22.

- [28] W. L. Stutzman and G. A. Thiele, *Antenna Theory and Design*. ,2nd ed.New York: J. Wiley, 1998, pp. 648.
- [29] C. A. Balanis, *Antenna Theory :Analysis and Design*. ,3rd ed.Hoboken, NJ: John Wiley, 2005, pp. 1117.
- [30] R. F. Harrington, *Time-Harmonic Electromagnetic Fields*. McGraw-Hill, 1961, pp. 480.
- [31] R. S. Elliott, *Antenna Theory and Design*. ,Revis ed.Hoboken, N.J.: John Wiley & Sons, 2003, pp. 594.
- [32] J. Harris and H. Stücker, *Handbook of Mathematics and Computational Science*. New York: Springer, 1998, pp. 1028.
- [33] C. G. Montgomery, R. H. Dicke and E. M. Purcell, *Principles of Microwave Circuits*. , vol. 8, New York: Dover Publications, 1965, pp. 486.
- [34] D. M. Pozar, *Microwave Engineering*. ,3rd ed.Hoboken, NJ: John Wiley, 2005, pp. 700.
- [35] D. M. Pozar and D. Schaubert. (1995, *Microstrip Antennas :The Analysis and Design of Microstrip Antennas and Arrays*. Available: <http://www.loc.gov.proxy.lib.sfu.ca/catdir/toc/onix07/>
- [36] L. J. Chu, "Physical limitations of omnidirectional antennas," Massachusetts Institute of Technology, Research Laboratory of Electronics, Massachusetts Institute of Technology, Research Laboratory of Electronics, Tech. Rep. 64, 1948, 1948.
- [37] H. A. Wheeler, "Fundamental Limitations of Small Antennas," *Proceedings of the IRE*, vol. 35, pp. 1479-1484, 1947.
- [38] J. S. McLean, "A re-examination of the fundamental limits on the radiation Q of electrically small antennas," *Antennas and Propagation, IEEE Transactions on*, vol. 44, pp. 672, 1996.
- [39] W. Richards, Y. Lo and D. Harrison, "An improved theory for microstrip antennas and applications," *Antennas and Propagation, IEEE Transactions on [Legacy, Pre - 1988]*, vol. 29, pp. 38-46, 1981.
- [40] K. Carver and J. Mink, "Microstrip antenna technology," *Antennas and Propagation, IEEE Transactions on [Legacy, Pre - 1988]*, vol. 29, pp. 2-24, 1981.
- [41] "IEEE standard test procedures for antennas," *ANSI/IEEE Std 149-1979*, 1979.
- [42] W. L. Stutzman, *Polarization in Electromagnetic Systems*. Artech House, 1993, pp. 256.

- [43] J. S. Hollis , T. J. Lyon and L. Clayton , *Microwave Antenna Measurements*. Atlanta: Scientific-Atlanta, 1970,
- [44] I. Khalifa and R. Vaughan, ""Polarization purity of higher mode circularly polarized circular patch antennas," in *Proceedings of the URSI Triennial International Symposium on Electromagnetic Theory*, 2007,
- [45] R. Munson, "Conformal microstrip antennas and microstrip phased arrays," *Antennas and Propagation, IEEE Transactions on [Legacy, Pre - 1988]*, vol. 22, pp. 74-78, 1974.
- [46] A. Derneryd, "A network model of the rectangular microstrip antenna," in 1977, pp. 93-95.
- [47] V. Antonchik and R. Vaughan, "Far field pattern for rectangular PIFA antenna from the cavity model," in 2005, pp. 226-229 vol. 2B.
- [48] R. Garg, *Microstrip Antenna Design Handbook*. Boston, MA: Artech House, 2001, pp. 845.
- [49] M. Kirschning and et al., "Accurate model for open end effect of microstrip lines," *Electron. Lett.*, vol. 17, pp. 123-125, 1981.
- [50] S. J. Orfanidis. *Electromagnetic Waves and Antennas*. [web-book]. Available: <http://www.ece.rutgers.edu/orfanidi/ewa/>, 2003
- [51] R. MacPhie and A. Zaghloul, "Radiation from a rectangular waveguide with infinite flange--Exact solution by the correlation matrix method," *Antennas and Propagation, IEEE Transactions on [Legacy, Pre - 1988]*, vol. 28, pp. 497-503, 1980.
- [52] I. -. Jan, R. F. Harrington and J. R. Mautz, "Aperture admittance of a rectangular aperture and its use," *Antennas and Propagation, IEEE Transactions on*, vol. 39, pp. 423-425, 1991.

9 APPENDICES

9.1 Maxwell equations

Maxwell equations in general form:

$$\begin{aligned}\nabla \times \bar{E} &= -j\omega \bar{B} - \bar{M} \\ \nabla \times \bar{H} &= j\omega \bar{D} + \bar{J} \\ \nabla \cdot \bar{D} &= \rho \\ \nabla \cdot \bar{B} &= 0\end{aligned}$$

where the nabla operator is defined as follows:

$$\nabla = \frac{\partial}{\partial x} \hat{x} + \frac{\partial}{\partial y} \hat{y} + \frac{\partial}{\partial z} \hat{z}$$

The definition of the curl of a vector in rectangular coordinates:

$$\nabla \times \bar{A} = \left(\frac{\partial A_z}{\partial y} - \frac{\partial A_y}{\partial z} \right) \hat{x} + \left(\frac{\partial A_x}{\partial z} - \frac{\partial A_z}{\partial x} \right) \hat{y} + \left(\frac{\partial A_y}{\partial x} - \frac{\partial A_x}{\partial y} \right) \hat{z}$$

For source free, isotropic and homogeneous medium, the Maxwell equations are:

$$\begin{aligned}\nabla \times \bar{E} &= -j\omega \bar{H} \\ \nabla \times \bar{H} &= j\omega \bar{E} \\ \nabla \cdot \bar{D} &= \nabla \cdot \epsilon \bar{E} = 0 \\ \nabla \cdot \bar{B} &= 0\end{aligned}$$

9.2 Wave (Helmholtz) equation

Taking the curl of the first Maxwell equation and solving for \bar{E} yields:

$$\nabla \times \nabla \times \bar{E} = -j\omega\mu\nabla \times \bar{H} = \omega^2\mu\varepsilon\bar{E}$$

Using the vector identity:

$$\nabla \times \nabla \times \bar{E} = \nabla(\nabla \cdot \bar{E}) - \nabla^2 \bar{E}$$

and the third Maxwell equation in the above equation yields:

$$\nabla^2 \bar{E} + \omega^2\mu\varepsilon\bar{E} = 0$$

where:

$$\nabla^2 = \frac{\partial^2}{\partial x^2} + \frac{\partial^2}{\partial y^2} + \frac{\partial^2}{\partial z^2}$$

The above equation is known as wave (Helmholtz) equation for a source free homogeneous medium.

The wave number is defined as:

$$k^2 = \omega^2\mu\varepsilon$$

or alternatively, using the wavelength representation:

$$k = \frac{2\pi}{\lambda}$$

The wave equation can be rewritten in the expanded form:

$$\frac{\partial^2 \bar{E}}{\partial x^2} + \frac{\partial^2 \bar{E}}{\partial y^2} + \frac{\partial^2 \bar{E}}{\partial z^2} + k^2 \bar{E} = 0$$

In the assumption that the electric field has only x component and propagates in y direction, the above equation reduces to:

$$\frac{\partial^2 \bar{E}_x}{\partial x^2} + k^2 \bar{E}_x = 0$$

The above equation is called a second order homogeneous wave equation and it has a general solution:

$$E(y) = Ae^{-jky} + Be^{jky}$$

where A and B are constants.

9.3 Boundary conditions

9.3.1 Arbitrary

The general expressions for boundary conditions at an arbitrary interface of media (currents) are given in [35]:

$$\begin{aligned}\hat{n} \cdot (\bar{D}_2 - \bar{D}_1) &= \rho_s \\ \hat{n} \cdot \bar{B}_2 &= \hat{n} \cdot \bar{B}_1 \\ (\bar{E}_2 - \bar{E}_1) \times \hat{n} &= \bar{M}_s \\ \hat{n} \times (\bar{H}_2 - \bar{H}_1) &= \bar{J}_s\end{aligned}$$

where:

\hat{n}	-	<i>normal unit vector</i>
\bar{D}	-	<i>electric displacement</i>
ρ_s	-	<i>surface charge density of the interface</i>
\bar{B}	-	<i>magnetic induction</i>
\bar{E}	-	<i>electric field</i>
\bar{M}_s	-	<i>surface magnetic current density</i>
\bar{H}	-	<i>magnetic field</i>
\bar{J}_s	-	<i>surface electric current density</i>

9.3.2 Electric wall

The boundary conditions for a perfect electric conductor can be also found in [35]:

$$\begin{aligned}\hat{n} \cdot \bar{D} &= \rho_s \\ \hat{n} \cdot \bar{B} &= 0 \\ \bar{E} \times \hat{n} &= 0 \\ \hat{n} \times \bar{H} &= \bar{J}_s\end{aligned}$$

9.3.3 Magnetic wall

The boundary conditions for a perfect magnetic conductor can be found in [35] as well:

$$\begin{aligned}\hat{n} \cdot \bar{D} &= 0 \\ \hat{n} \cdot \bar{B} &= 0 \\ \hat{n} \times \bar{E} &= -\bar{M}_s \\ \hat{n} \times \bar{H} &= 0\end{aligned}$$

9.4 Coordinate transformations

9.4.1 Rectangular to spherical coordinate transformation [1]

$$\begin{aligned}\hat{r} &= \sin \theta \cos \varphi \hat{x} + \sin \theta \sin \varphi \hat{y} + \cos \theta \hat{z} \\ \hat{\theta} &= \cos \theta \cos \varphi \hat{x} + \cos \theta \sin \varphi \hat{y} - \sin \theta \hat{z} \\ \hat{\varphi} &= -\sin \varphi \hat{x} + \cos \varphi \hat{y}\end{aligned}$$

9.4.2 Cylindrical to spherical coordinate transformation [1]

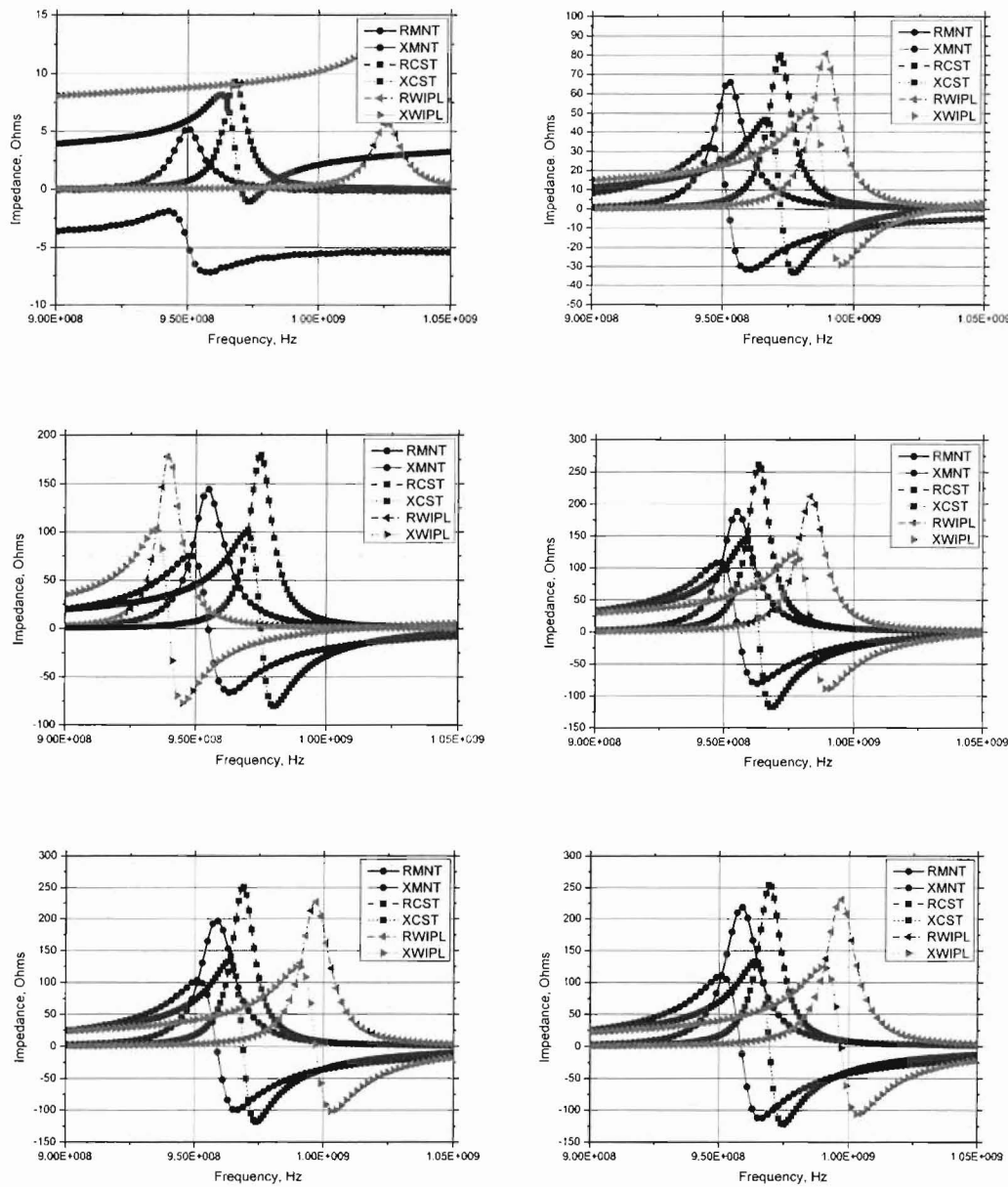
$$\begin{aligned}\hat{r} &= \sin \theta \hat{\rho} + \cos \theta \hat{z} \\ \hat{\theta} &= \cos \theta \hat{\rho} - \sin \theta \hat{z} \\ \hat{\varphi} &= \hat{\varphi}\end{aligned}$$

9.5 Far fields components for a magnetic current source

$$\begin{aligned} H_r &\approx 0 & E_r &\approx 0 \\ H_\theta &\approx -j\omega F_\theta & E_\theta &\approx -j\omega \eta F_\varphi \\ H_\varphi &\approx -j\omega F_\varphi & E_\varphi &\approx j\omega \eta F_\theta \end{aligned}$$

9.6 PIFA impedance measurements

9.6.1 Rectangular PIFA



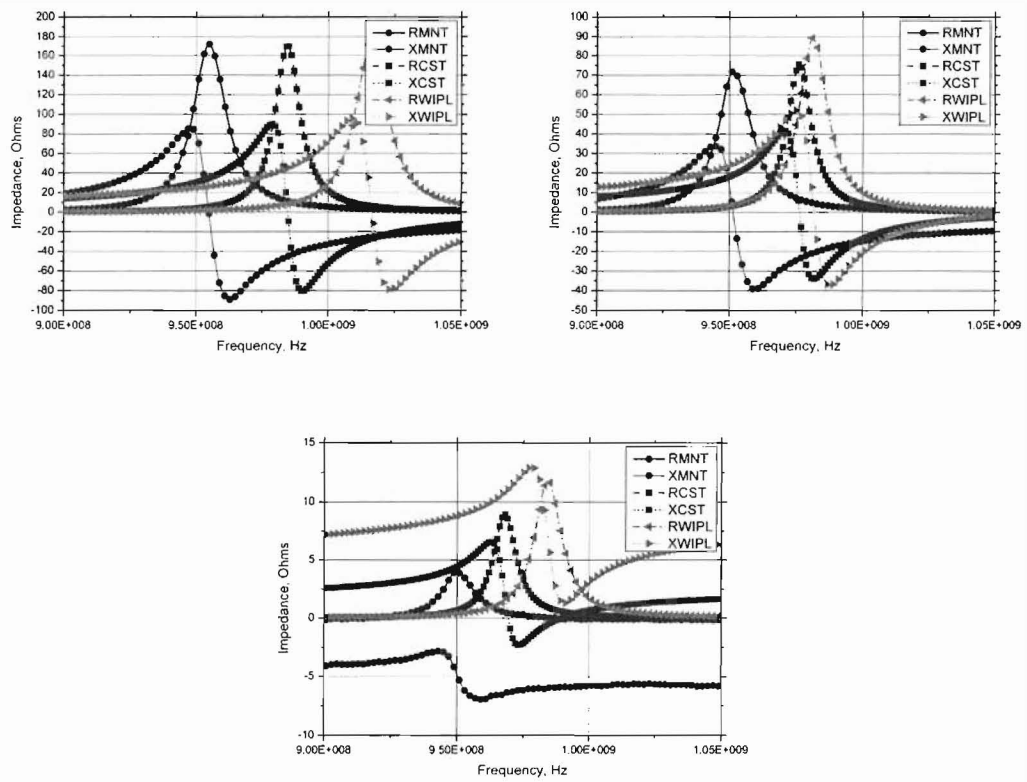
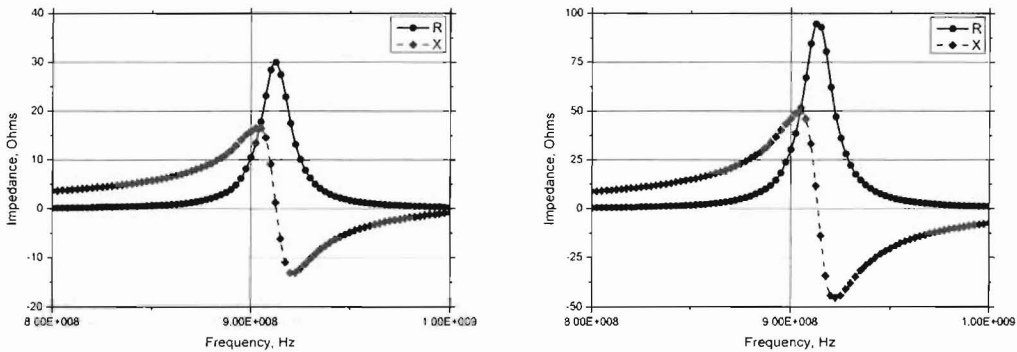


Figure 9.1 Measured and simulated input impedance of the probe-fed rectangular PIFA along sideslot (1-4), endslot (4-6) and center (6-9) versus frequency.

9.6.2 Semicircular PIFA



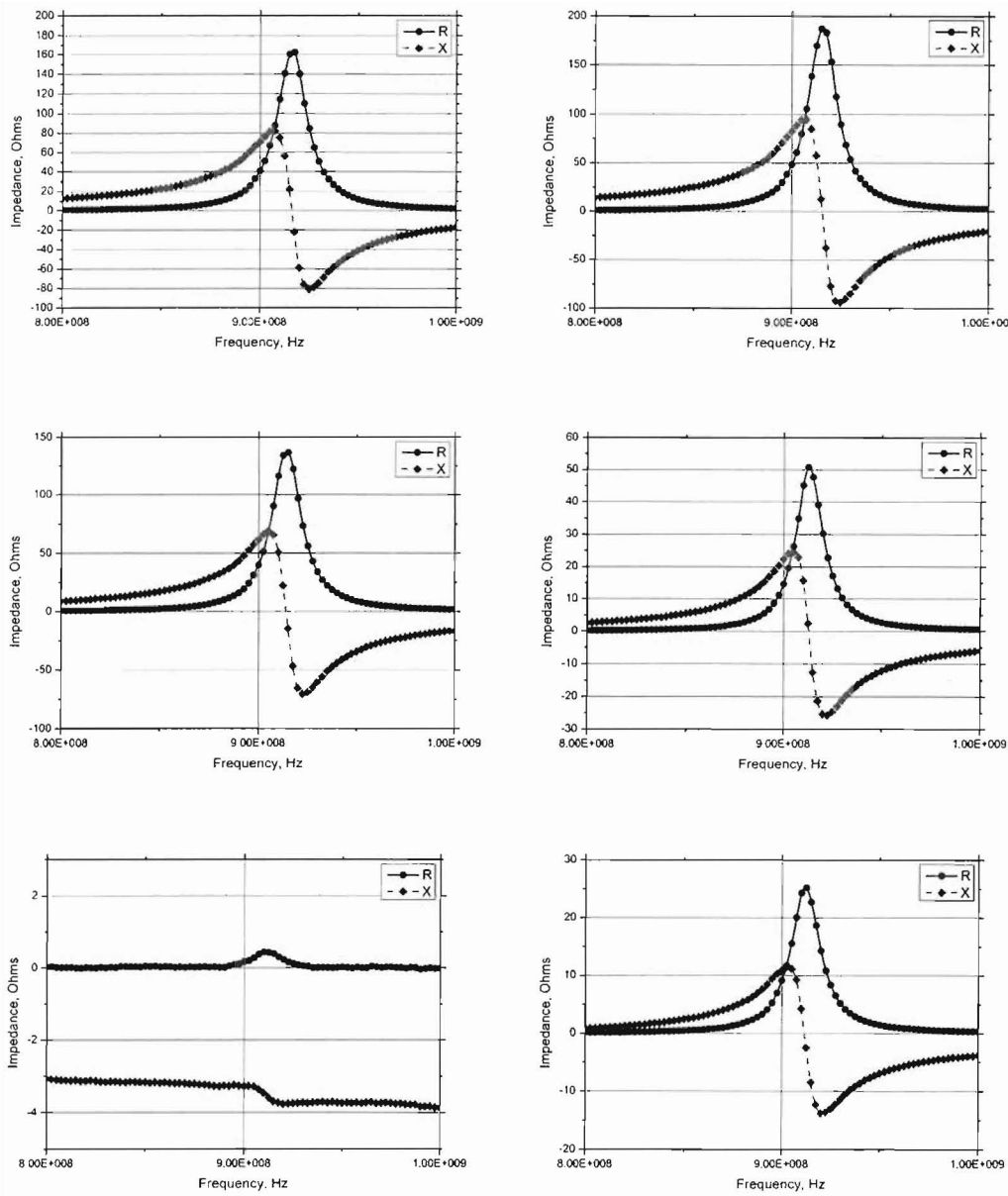


Figure 9.2 Measured input impedance of the probe-fed semicircular PIFA along circumference (1-4), center (4-7) and 45° radius (7,8,2) versus frequency.